sciendo

DOI: 10.2478/ata-2020-0025



Acta Technologica Agriculturae 4
Nitra, Slovaca Universitas Agriculturae Nitriae, 2020, pp. 155–160

# EFFECT OF BASIL OIL ON THE PERFORMANCE OF BIODIESEL FUELLED AGRICULTURAL ENGINE

Natesan KAPILAN[1]*, Rana Pratap REDDY[2]

[1]Nagarjuna College of Engineering and Technology, Bengaluru, India
[2]Global Academy of Technology, Bengaluru, India

The rapidly depleting fossil fuel resources and stringent emission norms have given importance to research of alternative fuels, especially in relation to reduction of greenhouse gases and global warming. In the work presented, biodiesel was derived from honge oil, which is non-edible. The oxidation stability of honge oil biodiesel is low due to the content of unsaturated fatty acids. Therefore, basil oil was used as a natural antioxidant to this biodiesel and the effect of this additive on the engine performance was studied. The addition of basil oil to the honge oil biodiesel increases its oxidation stability thanks to free radical scavenging activities of the basil oil. A set of engine tests was carried out on the agricultural diesel engine with honge oil biodiesel with different concentrations of basil oil. The engine tests showed that the addition of basil oil with the concentration of 1,000 ppm reduces the engine exhaust emissions in contrast to diesel. Basil oil does not have any significant impact on the engine brake thermal efficiency. Based on this work, it is possible to conclude that basil oil can be used as a natural additive to honge oil biodiesel for the purposes of oxidation stability improvement and significant reduction of oxides of nitrogen ($NO_x$) emission.

**Keywords:** alternative fuel; natural additive; properties; emissions

The industrial growth and globalisation increase the energy demand of the world and the use of fossil fuels for energy production increases carbon dioxide ($CO_2$) emissions. Biomass-based energy sources are considered an alternative to fossil fuels and $CO_2$ neutral (Joshi et al., 2017). The majority of recent research works is thus focused on biofuel development and adoption. Biodiesel is a sustainable alternative fuel (Lykova and Gustafsson, 2010). For example, rapeseed oil has significant potential in terms of biodiesel production in Latvia – biofuel production in Latvia was doubled due to demand (Pubule et al., 2011). Hydrocarbon (HC), carbon monoxide (CO) and particulate matter (PM) emissions of the diesel engine can be reduced significantly using biodiesel (Hasan and Rahman, 2017). Viscosity of olive oil is higher than sunflower oil viscosity due to its composition (Hlaváč et al., 2017), which can be reduced by optimising the process variables (Gulum and Bilgin, 2018). Innovative methods developed for the purposes of reduction of water requirements in biodiesel washing (Luna et al., 2014) and energy stimulant methods can be used to reduce energy consumption (Kapilan and Baykov, 2014).

Ginger extract with dosage of 250 ppm can be used as a natural antioxidant for honge oil biodiesel (Devi et al., 2017). Di-tertiary-butyl peroxide and 2-ethylhexyl nitrate additives added to the diesel-biodiesel-pentanol blends with dosage of 1,000 and 2,000 ppm reduce the NO emissions (Imdadul et al., 2017). Synthetic antioxidant propyl gallate (PG) improves the oxidation stability of honge oil biodiesel (Kapilan, 2017). The synthetic antioxidants pose greater risks of side effects (Aburigal et al., 2017), as they may be toxic to the biological systems (Eriotou et al., 2015). Biodiesel fuelled compression ignition engine emits higher amounts of $NO_x$ and various methods are used to reduce the $NO_x$ emission (Khalife et al., 2017). Engine tests conducted with methyl acetate as an additive show that this additive reduces CO and increases the $NO_x$ levels (Cakmak et al., 2018). Bio-butanol can be used in diesel engine using cetane number improver (Čedík et al., 2018).

Surface transport of India is dependent on fossil fuel import and hence India's bio-fuel policy stipulates the blending of bio-ethanol and biodiesel with fossil fuel. The non-edible oils are preferred for biodiesel production in India (Biswas and Pohit, 2013). India's fuel demand in the transportation sector may double by 2030 and hence the government of India gives priority to alternative fuels (Leduc et al., 2009). The non-edible oils, such as honge oil, have significant potential for biodiesel production (Patel and Sankhavara, 2017). Honge oil has a considerable potential for biodiesel production in India, however, it has lower oxidation stability and it is necessary to add antioxidants. Basil oil has better antioxidant and antimicrobial activities. Therefore, this work observes utilization of basil oil as a natural antioxidant for honge oil biodiesel and studies the impact of this additive on engine emissions and engine performance. Figs. 1 and 2 show honge tree and honge seeds. Basil (Fig. 3) is an aromatic plant and most widely

**Contact address:** Natesan Kapilan, Nagarjuna College of Engineering and Technology, Bengaluru, India;
e-mail: kapil_krecmech@yahoo.com

used to enhance the aroma and flavour in food. Furthermore, it is also used for medical purposes, because it contains chemical compounds (e.g. linalool, estragole and methyl-cinnamate), which can cure a variety of diseases.

## Material and methods

In this work, non-edible honge oil was used as a feedstock for biodiesel production. The biodiesel was produced by two step transesterification due to higher acid value of the honge oil. Basil oil was used as antioxidant for the honge oil biodiesel (HOB), as the oxidation stability of HOB was low. The basil oil was added with dosages of 1,000 and 2,000 ppm to the HOB. The basil oil completely mixes with the HOB and the fuel properties of the biodiesel and biodiesel with added basil oil were determined as per the ASTM standards.

Engine tests were performed on a single cylinder agricultural diesel engine and its technical specifications are given in Table 1. The engine speed was measured and indicated by an inductive pickup sensor in conjunction with a digital speed indicator. The engine load was varied using an eddy current dynamometer and the engine experimental setup is shown in Fig. 4. Engine emissions were measured using the AVL emission analyser. Necessary instrumentations were provided to measure the flow rates of fuel and air, and K-type thermocouple was used to measure the exhaust gas temperature (EGT).

**Table 1** Engine experimental setup specification

| Engine | Naturally aspirated compression ignition engine |
|---|---|
| Displacement | 661 CC |
| Maximum brake power | 5.2 kW at 1,500 rpm |
| Compression ratio | 17.5 : 1 |
| Bore and stroke dimension | 87.5 mm and 110 mm |
| Fuel injection | direct injection |

### Experimental methods

The engine tests were carried out using diesel as fuel to obtain baseline data. The engine tests were carried out at constant speed. The engine was

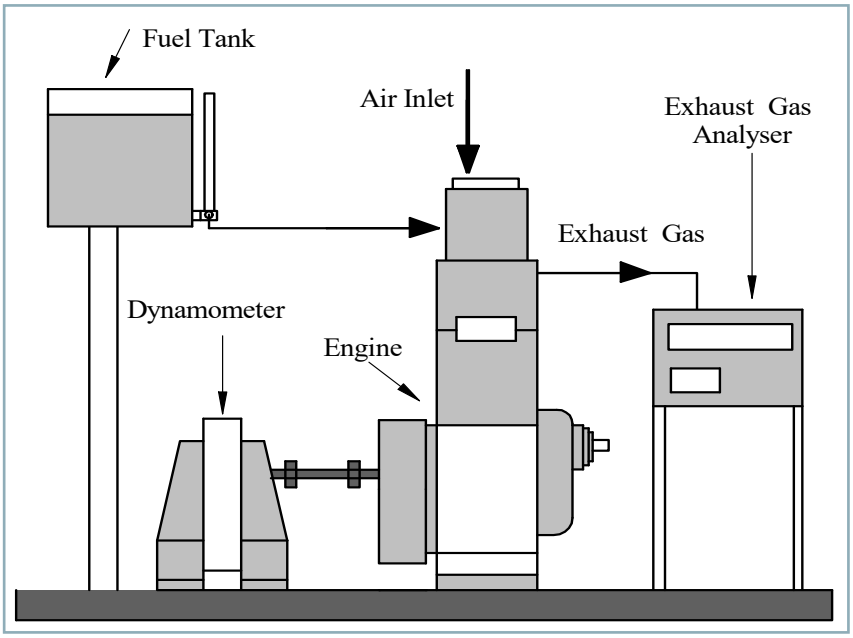


**Fig. 4** Engine experimental setup

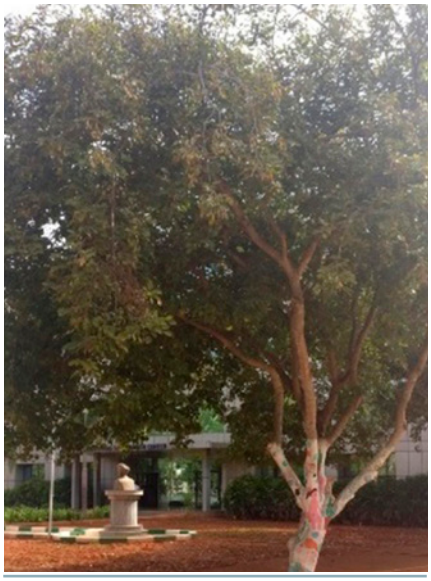

**Fig. 1** Honge tree

**Fig. 2** Honge seeds

**Fig. 3** Basil

**Table 2** Details of the engine exhaust gas analyser

| Exhaust gas analyser AVL Digas 444 N | | | | |
|---|---|---|---|---|
| **Exhaust gas** | **Principle** | **Range** | **Resolution** | **Uncertainty (%)** |
| **CO** | NDIR | 0 to 2.0 % vol | ±0.01 % vol | ±3 |
| **HC** | NDIR | 0 to 10,000 ppm | ±20 ppm | ±2 |
| **$NO_x$** | electrochemical | 0 to 5,000 ppm | ±10 ppm | ±2 |
| **Smoke meter AVL 437C** | | | | |
| **Smoke opacity** | | 0 to 100 | ±0.1 | ±1 |

started by hand cranking with diesel as fuel and allowed to warm up, the engine load was then increased to 4 kg. After the engine reached steady state condition, engine speed, air flow rate, fuel flow rate and EGT were measured. Gas analyser probe was placed in the engine's exhaust tube to measure and record emission levels. Subsequently, engine load was increased to next load (8 kg) and observations and emissions were recorded, and similar procedure was followed for other loads. After the engine test, the diesel was drained from the fuel tank and fuel filter. The tank was filled with new fuel, HOB (B100), and it was allowed to flow in the fuel supply line. The 100 ml of this fuel was collected from the fuel injector to remove the trace of previously used fuel in the fuel line. After this process, the fuel injector was fitted to its original position and engine was started. The engine was allowed to run for 15 min to remove any traces of previously used fuel in the combustion chamber. The important engine observations and emissions were recorded at steady state condition with the new fuel. Previously described procedure was followed for other fuels, such as B1,000 and B2,000.

## Results and discussion

The important properties of the fuels were determined and are shown in Table 3. The properties of HOB with added basil oil are better than those of pure HOB. Fire and flash points of biodiesel with added basil oil are better than those of pure HOB. However, the variation in viscosity and calorific value is small. The addition of basil oil increases the oxidation stability of HOB. Basil oil contains higher amount of linalool and methyl eugenol, which provide better antioxidant activity comparable to synthetic antioxidant BHT (Chenni et al., 2016). Basil oil does not affect copper corrosion value of HOB.

Engine tests were performed with different types of fuels and the impact of basil oil on engine performance and on emissions are discussed below. Engine performance is generally represented by the term brake thermal efficiency (BTE). BTE indicates the effectiveness of conversion of the fuel heat energy into engine shaft power. Fig. 5 shows the impact of basil oil on the engine BTE at various engine loads. BTE was low at part loads due to higher frictional losses; however, it gradually increased as the engine load increased. BTE was high at full engine load. Fig. 5 reveals that the addition of basil oil slightly improved the BTE at higher loads. Basil oil has better volatility in contrast to the biodiesel and thus improved spray formation, which resulted in better premixed combustion phase. BTE of HOB is lower than BTE of diesel, which is due to its higher viscosity and poor volatility. However, HOB with added basil oil of 1,000 ppm resulted in a slightly higher BTE in comparison to HOB and HOB with added basil oil of 2,000 ppm at full load.

Engine combustion temperature affected the EGT. Variation in EGT at different loads is depicted in Fig. 6. The engine consumed higher amount of fuel as the engine load increased. This caused higher combustion temperature and hence the EGT value increased with increase in load. HOB results in higher EGT in contrast to diesel. This is due to higher viscosity and lower volatility of HOB, leading to un-burnt fuels in the premixed combustion phase. This un-burnt fuel burns after the diffusion combustion phase and causes higher EGT. The addition of basil oil to the HOB reduces the EGT, as the basil oil improves the premixed combustion phase. Basil oil dosage of 1,000 ppm results in higher EGT than dosage of 2,000 ppm thanks to better combustion.

The variation of engine's CO emission at different loads and with various fuels is shown in the Fig. 7. Biodiesel contains oxygen, which enhances the combustion process and results in higher in-cylinder combustion temperature

**Table 3** Comparison of fuel properties

| **Property** | Diesel | Biodiesel | B1,000 ppm | B2,000 ppm |
|---|---|---|---|---|
| **Calorific value ($MJ \cdot kg^{-1}$)** | 42.71 | 39.41 | 39.40 | 39.38 |
| **Viscosity at 40 °C ($mm^2 \cdot s^{-1}$)** | 2.64 | 3.94 | 3.91 | 3.89 |
| **Fire point (°C)** | 71 | 161 | 157 | 151 |
| **Flash point (°C)** | 65 | 130 | 125 | 121 |
| **Oxidation stability (h)** | – | 3.5 | 6.3 | 7.6 |
| **Copper corrosion at 50 °C for 3 h** | 1a | 1a | 1a | 1a |

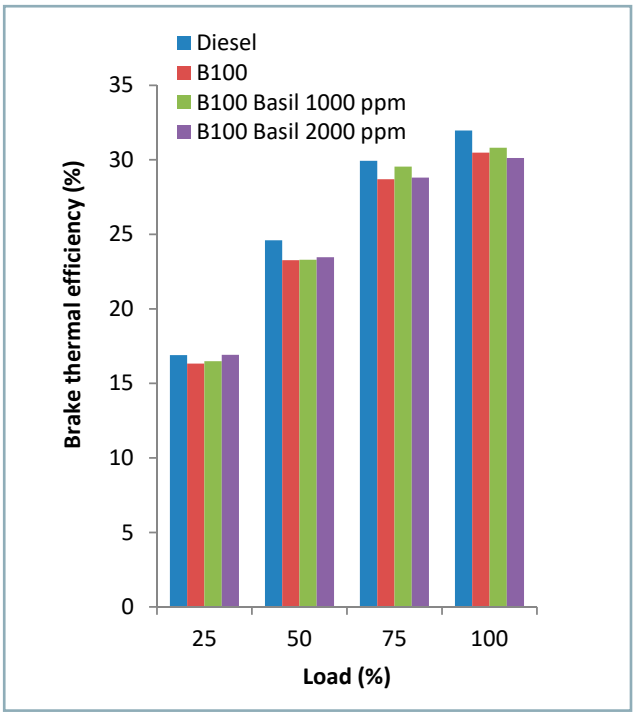


**Fig. 5** Variation in BTE at different loads

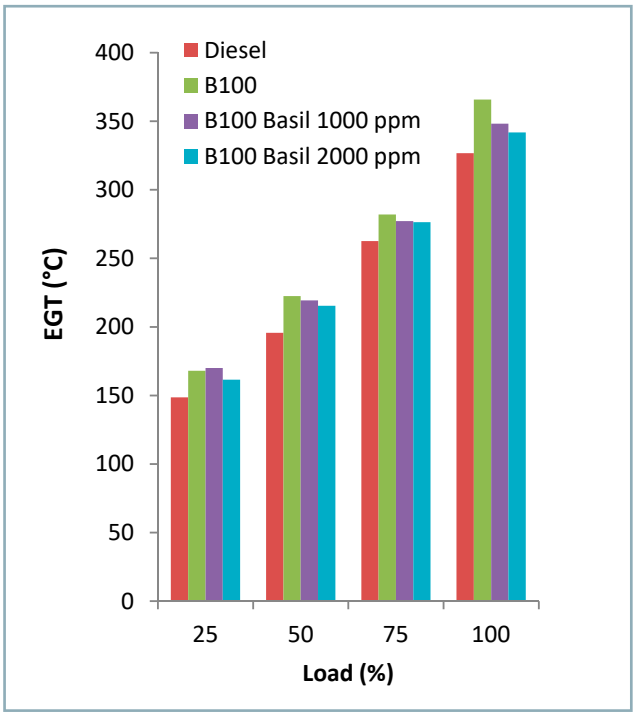


**Fig. 6** Variation in EGT at different loads

(Kivevele et al., 2011). HOB thus resulted in lower CO emission in comparison to diesel. However, addition of basil oil to biodiesel increased the CO level. Basil oil shows both antimicrobial and free radical scavenging activities (Eriotou et al., 2015) and the presence of eugenol in its chemical composition provides antioxidant properties (Politeo et al., 2007). Hydrogen peroxide ($H_2O_2$) and peroxyl radicals formed during combustion are converted into hydroxyl radicals due to absorption of heat from the combustion chamber. These radicals inhibit CO conversion, leading to an increase in the CO (Palash et al., 2014). However, the CO emission of HOB with added basil oil is low in contrast to diesel. The CO emission of HOB with 1,000 ppm of basil oil was lower than of HOB with 2,000 ppm of basil oil. At full load, the HOB CO emission was lower than the diesel CO emission; the CO emission of the HOB with 1,000 ppm basil oil was lower than the diesel CO emission at full load.

The un-burnt hydrocarbon (HC) emission of the engine depends on the fuel properties; fuel atomization; spray formation; and combustion efficiency. The changes in HC emission of the engine fuelled with various fuels at different loads is shown in Fig. 8. HOB produced lower HC emission compared to diesel, as biodiesel contains higher concentration of oxygen, which improves flame speed and

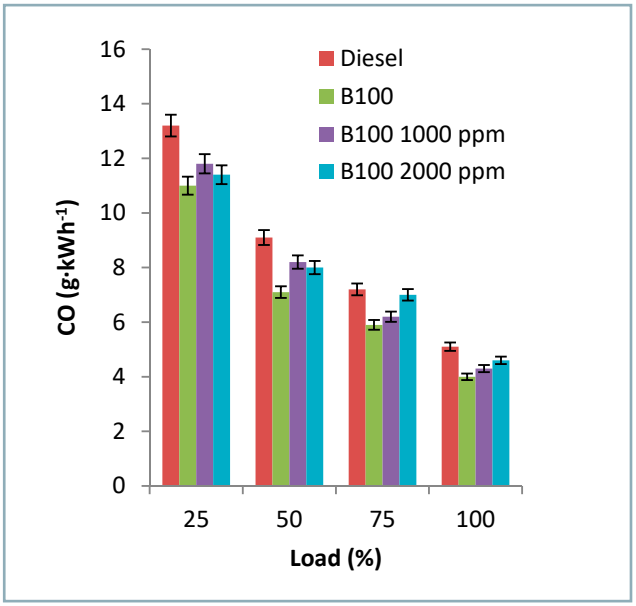


**Fig. 7** Variation in CO at different loads

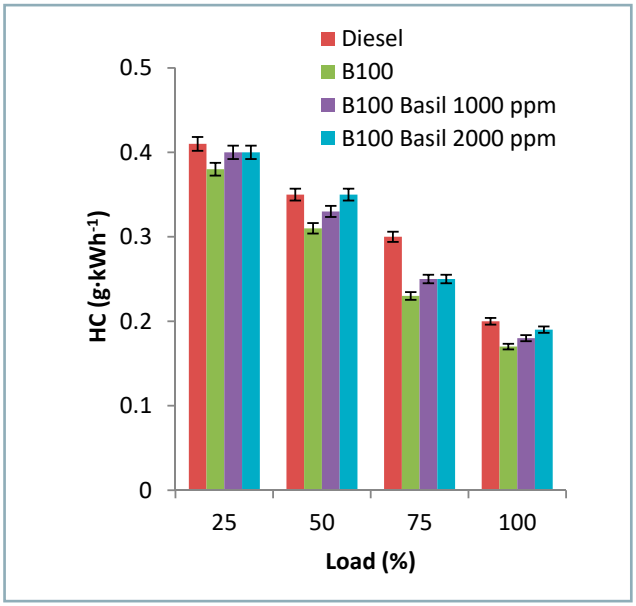


**Fig. 8** Variation in HC at different loads

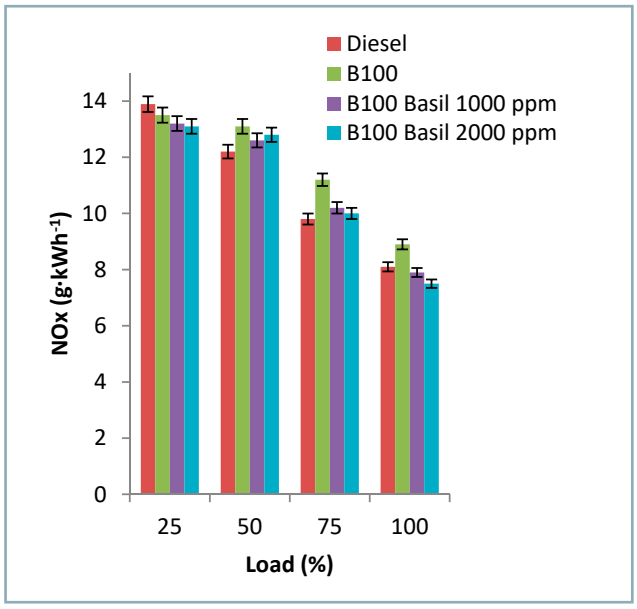


**Fig. 9** Variation in $NO_x$ at different loads

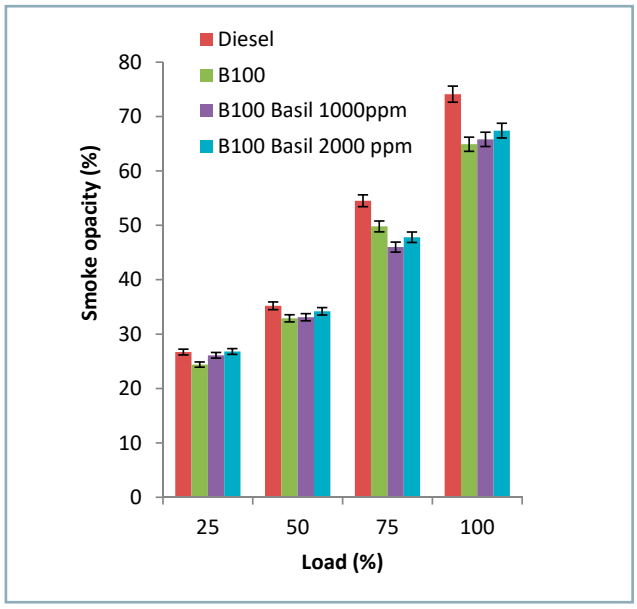


**Fig. 10** Variation in smoke level at different loads

enhances the post flame oxidation during air and fuel mixing specifically at fuel rich zones. This causes enhancement of the oxidation of unburnt HC, which reduces HC emission (Ozsezen et al., 2009). Basil oil increases the engine HC emission due to its free radical scavenging activities. Basil oil with concentration of 1,000 ppm resulted in lower HC emission compared to concentration of 2,000 ppm due to the lower basil oil quantity, which caused the lower free radical scavenging activity. However, the HC emission of HOB with 1,000 ppm of basil oil was lower than that of diesel. Similar type of behaviour of the antioxidant was also reported by Varatharajan et al. (2011). Biodiesel with 1,000 ppm resulted in 10% lower HC emission than the diesel at full load. The HC emission of HOB was 15% lower than that of diesel.

The variation in oxides of nitrogen ($NO_x$) at various engine loads with different fuels is shown in Fig. 9. The $NO_x$ emission is produced due to higher percentage of nitrogen in the air; combustion temperature; and longer presence of fuel inside the combustion chamber. HOB showed higher $NO_x$ emission than diesel due to presence of oxygen and higher bulk modulus of the HOB, which slightly advanced fuel injection timing and increased the time during which the fuel is present inside the combustion chamber. The addition of 1,000 ppm of basil oil to the biodiesel reduced the $NO_x$ emission by 7.8% in contrast to pure HOB. The basil oil contains free-radical scavenging compounds, such as phenolic compounds (Aburigal et al., 2017), that are excellent hydrogen donors and react with the species of reactive nitrogen and reactive oxygen. This termination reaction breaks new radical formation (Pereira et al., 2009).

Fig. 10 depicts the impacts of different fuels on the engine smoke opacity at various loads. Smoke emission indicates the visible part of poor combustion of the fuel burnt in combustion chamber. HOB produced smoke emission lower by 14% than diesel, since the biodiesel is oxygenated. HOB with 2,000 ppm of basil oil showed higher smoke emission in contrast to HOB with 1,000 ppm of basil oil. The addition of basil oil to the HOB increases the smoke emission because basil oil additive promotes reductive reactions inhibiting oxidative reactions (Wang et al., 2014). It is suggested that basil oil contains a phenolic compound with ability to scavenge the alkylperoxyl radical. The smoke emission of HOB with 1,000 ppm of basil oil was lower compared to diesel. However, a slight variation was observed between HOB with 2,000 ppm of basil oil and diesel and this behaviour is similar to observations reported by Khatib et al. (2018).

## Conclusion

Honge oil biodiesel contains unsaturated components, which result in lower oxidation stability. This issue can be improved by addition of basil oil to the biodiesel, thus enhancing its oxidation stability. The major emission of the agricultural diesel engine fuelled by biodiesel is $NO_x$ emission. The addition of basil oil to the HOB significantly affects the engine $NO_x$ emission. However, basil oil increases exhaust emissions, such as CO, HC and smoke, due to its free radical scavenging activities that reduce oxidation and inhibit fuel combustion. Nevertheless, these emission values are lower than those showed by fossil diesel. The addition of basil oil to the HOB does not have a significant impact on engine thermal efficiency. Basil oil dosage of 1,000 ppm resulted in lower CO, HC and smoke emissions and slightly higher BTE compared to basil oil dosage of 2,000 ppm. $NO_x$ emission reduction with basil oil dosage of 1,000 ppm at full load was 11.2% in contrast to the B100. Based on this work, it is possible to conclude that basil oil can be used as an antioxidant for the HOB, significantly reducing $NO_x$ emission.

## Acknowledgments

Authors express their gratitude to VTU for funding this project (Aca. /2013-14 / A-9/63).

## References


ABURIGAL, Y. A. A. – MIRGHANI, M. E. S. – ELMOGTABA, E. Y. – SIRIBLE, A. A. M. – HAMZA, N. B. – HUSSEIN, I. H. 2017. Total phenolic content and antioxidant capacity of basil (*Ocimum basilicum* L.) leaves from different locations. In International Food Research Journal, vol. 24, pp. 378–381.

BISWAS, P. K. – POHIT, S. 2013. What ails India's biodiesel programme? In Energy Policy, vol. 52, pp. 789–796.

CAKMAK, A. – KAPUSUZ, M. – GANIYEV, O. – OZCAN, H. 2018. Effects of methyl acetate as oxygenated fuel blending on performance and emissions of SI engine. In Environmental and Climate Technologies, vol. 22, no. 1, pp. 55–68.

ČEDÍK, J. – PEXA, M. – PETERKA, B. – HOLŮBEK, M. – MADER, D. – PRAŽAN, R. 2018. Effect of biobutanol-sunflower oil-diesel fuel blends on combustion characteristics of compression ignition engine. In Acta Technologica Agriculturae, vol. 21, no. 4, pp. 130–135.

DEVI, A. – DAS, V. K. – DEKA, D. 2017. Ginger extract as a nature based robust additive and its influence on the oxidation stability of biodiesel synthesized from non-edible oil. In Fuel, vol. 187, pp. 306–314.

ERIOTOU, E. – ANASTASIADOU, K. – NIKOLOPOULOS, D. – KOULOUGLIOTIS, D. 2015. Antimicrobial and free radical scavenging activities of basil (*Ocimum basilicum*) essential oil isolated from five plant varieties growing in Greece. In Journal of Nutrition & Food Sciences, vol. 5, no. 3, pp. 1–9.

GULUM, M. – BILGIN, A. 2018. An experimental optimization research of methyl and ethyl esters production from safflower oil. In Environmental and Climate Technologies, vol. 22, no. 1, pp. 132–148.

HASAN, M. – RAHMAN, M. 2017. Performance and emission characteristics of biodiesel-diesel blend and environmental and economic impacts of biodiesel production: A review. In Renewable and Sustainable Energy Reviews, vol. 74, pp. 938–948.

HLAVÁČ, P. – BOŽIKOVÁ, M. – PETROVIĆ, A. 2017. Selected physical properties assessment of sunflower and olive oils. In Acta Technologica Agriculturae, vol. 22, no. 3, pp. 86–91.

CHENNI, M. – EL ABED, D. – RAKOTOMANOMANA, N. – FERNANDEZ, X. – CHEMAT, F. 2016. Comparative study of essential oils extracted from Egyptian basil leaves (*Ocimum basilicum* L.) using hydro-distillation and solvent-free microwave extraction. In Molecules, vol. 21, no. 1, pp. 113–118.

IMDADUL, H. – RASHED, M. – SHAHIN, M. – MASJUKI, H. – KALAM, M. – KAMRUZZAMAN, M. – RASHEDUL, H. 2017. Quality improvement of biodiesel blends using different promising fuel additives to reduce fuel consumption and NO emission from CI engine. In Energy Conversion and Management, vol. 138, pp. 327–337.

JOSHI, G. – PANDEY, J. K. – RANA, S. – RAWAT, D. S. 2017. Challenges and opportunities for the application of biofuel. In Renewable and Sustainable Energy Reviews, vol. 79, pp. 850–866.

KAPILAN, N. – BAYKOV, B. D. 2014. A review on new methods used for the production of biodiesel. In Petroleum & Coal, vol. 56, no. 1, pp. 62–73.

KAPILAN, N. 2017. Studies on effect of antioxidant on the performance of biodiesel operated diesel engine. In Journal of Sustainable Energy Engineering, vol. 5, no. 1, pp. 3–12.

KHALIFE, E. – TABATABAEI, M. – DEMIRBAS, A. – AGHBASHLO, M. 2017. Impacts of additives on performance and emission characteristics of diesel engines during steady state operation. In Progress in Energy and Combustion Science, vol. 59, pp. 32–78.

KHATIB, S. – HARNAFI, M. – TOUISS, I. – BEKKOUCH, O. – AMRANI, S. – HARNAFI, H. 2018. Phenolic extract of basil prevents lipid oxidation in sunflower oil, beef and turkey meat: A comparison with synthetic antioxidant BHA. In American Journal of Food Science and Nutrition, vol. 5, no. 3, pp. 66–75.

KIVEVELE, T. T. – KRISTÓF, L. – BERECZKY, Á – MBARAWA, M. M. 2011. Engine performance, exhaust emissions and combustion characteristics of a CI engine fuelled with croton megalocarpus methyl ester with antioxidant. In Fuel, vol. 90, no. 8, pp. 2782–2789.

LEDUC, S. – NATARAJAN, K. – DOTZAUER, E. – MCCALLUM, I. – OBERSTEINER, M. 2009. Optimizing biodiesel production in India. In Applied Energy, vol. 86, pp. 145–153.

LUNA, D. – CALERO, J. – SANCHO, E. – LUNA, C. – POSADILLO, A. – BAUTISTA – VERDUGO, C. 2014. Technological challenges for the production of biodiesel in arid lands. In Journal of Arid Environments, vol. 102, pp. 127–138.

LYKOVA, N. – GUSTAFSSON, J. E. 2010. A survey of biofuel production potentials in Russia. In Scientific Journal of Riga Technical University: Environmental and Climate Technologies, vol. 4, no. 1, pp. 64–75.

OZSEZEN, A. N. – CANAKCI, M. – TURKCAN, A. – SAYIN, C. 2009. Performance and combustion characteristics of a DI diesel engine fuelled with waste palm oil and canola oil methyl esters. In Fuel, vol. 88, no. 4, pp. 629–636.

PALASH, S. – KALAM, M. – MASJUKI, H. – ARBAB, M. – MASUM, B. – SANJID, A. 2014. Impacts of $NO_x$ reducing antioxidant additive on performance and emissions of a multi-cylinder diesel engine fuelled with Jatropha biodiesel blends. In Energy Conversion and Management, vol. 77, pp. 577–585.

PATEL, R. L. – SANKHAVARA, C. 2017. Biodiesel production from Karanja oil and its use in diesel engine: A review. In Renewable and Sustainable Energy Reviews, vol. 71, pp. 464–474.

PEREIRA, D. – VALENTÃO, P. – PEREIRA, J. – ANDRADE, P. 2009. Phenolics: From chemistry to biology. In Molecules, vol. 14, pp. 2202–2211.

POLITEO, O. – JUKIC, M. – MILOS, M. 2007. Chemical composition and antioxidant capacity of free volatile aglycones from basil (*Ocimum basilicum* L.) compared with its essential oil. In Food Chemistry, vol. 101, no. 1, pp. 379–385.

PUBULE, J. – ROMAGNOLI, F. – BLUMBERGA, D. 2011. Why biodiesel is environmentally better than traditional, fossil-based diesel: An LCA approach. In Environmental and Climate Technologies, vol. 7, no. 1, pp. 93–99.

VARATHARAJAN, K. – CHERALATHAN, M. – VELRAJ, R. 2011. Mitigation of $NO_x$ emissions from a Jatropha biodiesel fuelled DI diesel engine using antioxidant additives. In Fuel, vol. 90, no. 8, pp. 2721–2725.

WANG, Z. – WU, J. – MAO, G. – QU, L. – WANG, F. – HU, H. 2014. Effect of antioxidants on emission of biodiesel. In the Transactions of the Chinese Society of Agricultural Engineering, vol. 30, pp. 266–271.

sciendo

DOI: 10.2478/ata-2020-0026



Acta Technologica Agriculturae 4
Nitra, Slovaca Universitas Agriculturae Nitriae, 2020, pp. 161–167

# SENSORY EVALUATION OF PLIEK-U QUALITY USING FUZZY-TOPSIS METHOD

Raida AGUSTINA*, MUSTAQIMAH, Rahmat FADHIL, DEVIANTI

Universitas Syiah Kuala, Indonesia

The purpose of this study is to apply one of the decision-making methods, namely the fuzzy-TOPSIS method, to determine the best alternative of coconut fermentation in process of making Pliek-U, which is a typical powder made of coconut and is used for traditional cooking recipes by people in Aceh Province, Indonesia. The weight of fuzzy criteria and judgments about alternative methods of coconut fermentation was used to calculate the sensory evaluation scores and Pliek-U quality ratings. It can help to determine the quality of the Pliek-U. Sensory evaluation results for the quality of Pliek-U using the fuzzy-TOPSIS method showed that the most ideal alternative of the coconut fermentation method in the process of making Pliek-U is the 10-day coconut fermentation method, because it had the highest closeness coefficient (0.7484) in contrast to the 7-day coconut fermentation method (0.5425), and 4-day coconut fermentation method (0.3291). The fuzzy-TOPSIS method utilization was beneficial for generating the sensory multi-criteria assessment calculations through weighting, so that the process of determining consumer acceptance of the product assessed became easier and faster.

**Keywords:** coconut; fermentation; quality rating; respondent; hedonic scale

There are three derivative products made of processed coconut, i.e. Pliek-U, Simplah oil, or fermented virgin coconut oil (FVCO) (Khathir et al., 2020), and Pliek oil. Processing of Pliek-U requires several essential stages, namely the fermentation stage, and then the oil is separated after several days of fermentation. The next stage includes drying and pressing with hydraulic pressure (Agustina and Munawar, 2019). Pliek-U produced by conventional fermentation processes has a slightly acidic taste, smells rancid, is moldy, and of dark color (Rohaya et al., 2019). The improvement of Pliek-U fermentation method by several alternative fermentation techniques is expected to increase the quality and quantity of Pliek-U (Mustaqimah et al., 2019).

Sirangelo (2019) explained that sensory evaluation can be done objectively or subjectively. In many cases, the available data is sometimes inadequate for issues in real life, because human judgments, including preferences, are often vague or unclear and preferences cannot be estimated with an appropriate numerical value. Therefore, a fast method of evaluating consumer acceptance of food products is needed. One method of evaluating the respondents' opinions is the fuzzy-TOPSIS (Technique for Order Performance by Similarity to Ideal Solution) method, in which the respondents evaluate each product and provide an assessment of the product acceptance level based on multi-sensory criteria including aroma, colour, taste, and texture (Fadhil et al., 2019).

## Fuzzy-TOPSIS method

Many methods are used in ranking and choosing the alternative solutions to solve problems in decision making that are influenced by multi-criteria (Tulkhah and Saifuddin, 2019). One method commonly used for multi-criteria decision-making techniques (Multiple Attribute Decision Making MADM) is the fuzzy-TOPSIS method, which was first introduced by Yoon (1980), Hwang and Yoon (1981), Yoon and Kim (2017). Furthermore, this method has been used by Rouhani et al. (2012), Fadhil et al. (2017a), Fadhil et al. (2017b), Shindu et al. (2019), Fadhil et al. (2019), Yazdi et al. (2020), and Rouyendegh et al. (2020). Fuzzy-TOPSIS method can help in evaluating of various alternatives of various criteria that are considered, including in determining the right method to produce high-quality food products based on sensory evaluation. In the fuzzy-TOPSIS approach, the alternative selection is based on the value of closeness to the value of a positive ideal solution (FPIS), and on the furthest value from the value of a negative ideal solution (FNIS) (Papilo et al., 2018). According to Fadhil et al. (2019), TOPSIS can only be implemented for criteria, weights of which are known or calculated beforehand, because there is a stage in TOPSIS involving the multiplication process of criteria weights and alternative values on a criterion.

The purpose of this study is to apply the fuzzy-TOPSIS decision-making technique in determining the best alternative for the selection of coconut fermentation methods in the process of making Pliek-U. Results of the fuzzy-TOPSIS method analysis are expected to be used as information or recommendations to help farmers or business producers in determining the best alternative for coconut fermentation in making Pliek-U.

**Contact address:** Raida Agustina, Universitas Syiah Kuala (UNSYIAH), Department of Agricultural Engineering, Jalan Teungku Hasan Krueng Kalee No. 3 Kopelma Darussalam, Banda Aceh 23111 Indonesia; e-mail: raidaagustina@unsyiah.ac.id

## Material and methods

This research was conducted at the Post Harvest Technology Laboratory of Agricultural Engineering Study Program, Agriculture Faculty, Universitas Syiah Kuala, in June 2019. The material used in this study was coconut meat that was rasped. The tools used included digital scale meters, thermometers, dryers, and hydraulic type press tools.

### Research stages

This research was divided into two main stages. The first stage was the Pliek-U fermentation process with a combination of thick pile treatment and fermentation time. The second stage was conducting a multi-criteria sensory assessment of Pliek-U through the collection of respondents/ panellists' opinions.

### Framework

The determination of weighting of respondents' assessment criteria for multi-criteria in the Pliek-U sensory evaluation was done by a hedonic scale, which can also be changed to a numerical scale with number quality according to the preference level. The respondent's hedonic scale included aroma, colour, and taste of Simplah oil, Pliek oil, and Pliek-U. Chauhan and Sharma (2003) mentioned that sensory assessments utilizing human senses, such as aroma, colour, and taste, are the most influential judgments on the acceptance of a product based on the decisions of respondents/panellists. The detailed explanation of each of these criteria is shown in Table 1, while the Pliek-U sensory preference values based on the hedonic scale are presented in Table 2. An assessment of each alternative by respondents using the fuzzy-TOPSIS method with preference values is given in Table 3.

**Table 1** Pliek-U sensory multi-criteria assessment criteria

| Criteria | Assessment considerations |
|---|---|
| **Colour of simplah Oil (C1)** | limpid, clear |
| **Aroma of simplah Oil (C2)** | the aroma is rather pungent |
| **Colour of pliek oil (C3)** | yellowish limpid, clear |
| **Aroma of pliek oil (C4)** | typical aroma of coconut oil |
| **Colour of pliek-U (C5)** | brownish |
| **Aroma of pliek-U (C6)** | typical aroma of coconut, not rancid and rather acidic |
| **Taste of pliek-U (C7)** | acidic |

**Table 2** Pliek-U sensory assessment preferences based on hedonic scale

| Value | Preference |
|---|---|
| **5** | really like |
| **4** | like |
| **3** | neutral |
| **2** | dislike |
| **1** | wery dislike |

**Table 3** Comparison of alternative determination scale of fuzzy-TOPSIS method

| Scale | TFN linguistic |
|---|---|
| **Very dislike (VD)** | 1, 1, 2 |
| **Dislike (D)** | 1, 2, 3 |
| **Neutral (N)** | 2, 3, 4 |
| **Like (L)** | 3, 4, 5, |
| **Really like (RL)** | 4, 5, 5 |

The framework of this research was construed in four steps, namely:

1. the aim was set as sensory evaluation of Pliek-U;
2. the analysis was done through determining the weight of assessment criteria and determining alternative decisions;
3. alternative determination methods using fuzzy-TOPSIS were carried out;
4. alternative ranking decisions were obtained as results.

### Respondent selection

Ten respondents were selected to conduct a sensory multi-literacy assessment of Pliek-U with various types of treatment. The selection of respondents was determined by using a number of criteria – whether they are fond of Pliek-U, whether they prefere to consume it either raw or in the form of processed products, whether they are experienced in sensory testing, whether they show any sign of illness (such as colds, cough, canker sores, etc.) – which may interfere the sensory testing process, whether they are not colour-blind, etc.

These criteria were used because sensory evaluation is very dependent on humans who will accurately express their sensory experiences of a product (Hamilton and Jacob, 2020). Lawless and Heymann (2010) also mentioned that sensory evaluation consists of a series of ways to measure human responses to food, which minimize the effects that have the potential to cause bias on the characteristics and identity of a product, as well as the influence of other information on consumer perception.

### Fuzzy-TOPSIS procedure

The fuzzy-TOPSIS method used in this study was carried out by weighing the criteria with a Triangular Fuzzy Number (TFN) value; in such manner, the criteria are more objective (Pochampally et al., 2004). This was because the data from the respondents' preferences that were available were inadequate to solve the problem of the Pliek-U fermentation method, because the human judgment of preferences is often influenced by subjectivity, so the results are vague or unclear and cannot determine the preference values with appropriate numerical values.

### Steps of the fuzzy-TOPSIS method

Halicka (2020) mentioned steps in the application of the fuzzy-TOPSIS method, i.e.:

1. Choosing the right linguistic variable with the importance criteria ($\tilde{w}_j = l_{ij}, m_{ij}, u_{ij}$) and alternative linguistic ranking of the criteria ($\tilde{x}_{ij}$) in TFN.
2. Aggregating the weights from each criterion to get fuzzy weight aggregates ($\tilde{w}_j$) on the criteria $C_j$ and determining the fuzzy aggregate weight of the alternative $A_i$ on each criterion $C_j$:

$$\tilde{x}_{ij} = \frac{1}{k}\left[\tilde{x}_{ij}^1 + \tilde{x}_{ij}^2 + ... + \tilde{x}_{ij}^k\right] \quad (1)$$

$i = 1, 2..., m; j = 1, 2..., n$

$$w_j = \frac{1}{k}\left[\tilde{w}_j^1 + \tilde{w}_j^2 + ... + w_j^k\right] \quad (2)$$

$j = 1, 2..., n$

3. Building a normalized decision matrix. Pochampally et al. (2004) mentioned this step to change the size of various dimensions of performance into non-dimensional attributes. The $r_{ij}$ element resulted from the normalization of the decision matrix $R$ with the Euclidean length of a vector method as follows:

$$r_{ij} = \frac{x_{ij}}{\sqrt{\sum_{i=1}^{m} x_{ij}^2}} \quad (3)$$

with $i = 1, 2, 3..., m; j = 1, 2, 3..., n$

4. Building the weighted normalized decision matrix.

   Positive ideal solution $A^+$ and negative ideal solution $A^-$ can be determined based on the normalized weight rating ($y_{ij}$) as:

$$y_{ij} = w_i r_{ij} \quad (4)$$

with $i = 1, 2, 3..., m; j = 1, 2, 3..., n$

5. Determining a positive ideal solution matrix and a negative ideal solution matrix. Positive ideal solution ($A^+$) is calculated based on:

$$S^+ = \left(y_1^+, y_2^+, y_3^+ ... \ ... \ ... y_n^+\right) \quad (5)$$

Negative ideal solution $A^-$ is calculated based on:

$$S^- = \left(y_1^-, y_2^-, y_3^- ... \ ... \ ... y_n^-\right) \quad (6)$$

6. Calculating the distance between each alternative value with the value of FPIS (Fuzzy Positive Ideal Solution) and FNIS (Fuzzy Negative Ideal Solution):

$$D_1^+ = \sqrt{\sum_{i=1}^{n}\left(y_{ij} - y_i^+\right)^2} \quad (7)$$

$i = 1, 2, 3..., m$

$$D_1^- = \sqrt{\sum_{i=1}^{n}\left(y_{ij} - y_i^-\right)^2} \quad (8)$$

$i = 1, 2, 3..., m$

7. Determining the preference value for each alternative. The closeness of each alternative to the ideal solution is calculated based on the formula:

$$CC_i = \frac{D_i^-}{D_i^+ + D_i^-} \quad (9)$$

$i = 1, 2, 3..., m$

8. Ranking the alternative.

   After the preference value for each alternative was determined, alternatives were ranked according to the $CC_i$ value (Boran et al., 2009). The alternative with the largest $CC_i$ value represented the best solution.

## Results and discussion

The alternative determination was conducted by following the fuzzy-TOPSIS method through the decomposition of the analysis results into 6 stages. The best alternative was selected based on the highest closeness coefficient to each alternative compared.

### Stage 1

Input data were collected via sensory questionnaires with a hedonic scale that were arranged into a comparison matrix (Table 4).

**Table 4** Respondents' assessment matrix on various alternative methods of coconut fermentation

| Criteria | | Fermentation alternatives | | |
|---|---|---|---|---|
| | | 4 days | 7 days | 10 days |
| Simplah Oil | colour (C1) | 5 | 5 | 5 |
| | aroma (C2) | 4 | 3 | 4 |
| Pliek Oil | colour (C3) | 3 | 4 | 4 |
| | aroma (C4) | 4 | 3 | 3 |
| Pliek-U | colour (C5) | 5 | 5 | 4 |
| | aroma (C6) | 3 | 3 | 4 |
| | taste (C7) | 3 | 4 | 4 |

Sensory evaluation can be used as an instrument to control the quality of a product, because the people's acceptance or preference represented by respondents is one of the keys to the success of marketing the product (Popov-Raljic and Lalicic-Petronijevic, 2009; Ana et al., 2017). Consumers often judge the initial quality of a product by its colour and appearance, because this is the main indicator

when assessing the product quality, especially food. Colour also correlates with changes in aroma and taste (Lawless and Heymann, 2010). For Simplah oil colour, all respondents gave a value of 5 (really like). For Pliek-U oil and Pliek-U colour, respondents gave a value of 4 (like) for 10-day fermentation.

For the aroma of Simplah oil, respondents gave a rating of 4 (like) for 10-day fermentation. For the aroma of Pliek oil, respondents gave a value of 4 (like) for 4-day fermentation, because it was typical of coconut oil and not rancid. The longer the fermentation time, the higher the free fatty acids content in Pliek oil. According to Umudee et al. (2013), the percentage of free fatty acids is the most important parameter for assessing the quality of vegetable oils, such as copra oil, the content of free fatty acids of which can increase by 1,410% during fermentation to a range of 0.660–2.502%. One way to reduce the free fatty acids in oil is by using microwave heating (Vieira and Regitano-D'Arce, 1998; Khathir et al., 2020). Application of metal-organic frameworks enhances the physicochemical properties of unrefined vegetable oils (more pleasant taste and odour), because free fatty acids and peroxide compounds are bound in such manner (Hlaváč et al., 2019). For the aroma of Pliek-U, respondents gave a value of 4 (like) for10-day fermentation, because Pliek-U showed typical aroma of coconut, which was neither rancid, nor acidic.

For the taste of Pliek-U, respondents gave a value of 4 (like) for 10-day fermentation, because its taste was more acidic than in case of 4-day fermentation. Based on research of Mustaqimah et al. (2019), the pH value of the 10-day fermented Pliek-U was 5.0, while that of 4-day and 7-day fermentation were 5.8 and 5.1, respectively. Therefore, it can be concluded that the longer the fermentation period,

**Table 5** Respondent's assessment matrix of alternative fermentation methods on the TFN scale

| Criteria | | 4-day fermentation | | | 7-day fermentation | | | 10-day fermentation | | |
|---|---|---|---|---|---|---|---|---|---|---|
| | | lower | middle | upper | lower | middle | upper | lower | middle | upper |
| **Simplah oil** | colour (C1) | 4 | 5 | 5 | 4 | 5 | 5 | 4 | 5 | 6 |
| | aroma (C2) | 3 | 4 | 5 | 2 | 3 | 4 | 3 | 4 | 5 |
| **Pliek oil** | colour (C3) | 2 | 3 | 4 | 3 | 4 | 5 | 3 | 4 | 5 |
| | aroma (C4) | 3 | 4 | 5 | 2 | 3 | 4 | 2 | 3 | 4 |
| **Pliek-U** | colour (C5) | 4 | 5 | 5 | 4 | 5 | 5 | 3 | 4 | 5 |
| | aroma (C6) | 2 | 3 | 4 | 2 | 3 | 4 | 3 | 4 | 5 |
| | taste (C7) | 2 | 3 | 4 | 3 | 4 | 5 | 3 | 4 | 5 |

**Table 6** Matrix multiplication of weighting criteria and alternative normalization values

| Criteria | | 4-day fermentation | | | 7-day fermentation | | | 10-day fermentation | | |
|---|---|---|---|---|---|---|---|---|---|---|
| | | l | m | u | l | m | U | l | m | u |
| **Simplah oil** | colour (C1) | 1.33 | 2.50 | 3.33 | 1.33 | 2.50 | 3.33 | 1.33 | 2.50 | 4.00 |
| | aroma (C2) | 1.80 | 2.40 | 3.00 | 1.20 | 2.40 | 4.00 | 1.80 | 3.20 | 5.00 |
| **Pliek oil** | colour (C3) | 0.80 | 1.80 | 3.20 | 1.20 | 2.40 | 4.00 | 1.20 | 2.40 | 4.00 |
| | aroma (C4) | 1.80 | 3.20 | 5.00 | 1.20 | 2.40 | 4.00 | 1.20 | 2.40 | 4.00 |
| **Pliek-U** | colour (C5) | 1.60 | 3.00 | 4.00 | 1.60 | 3.00 | 4.00 | 1.20 | 2.40 | 4.00 |
| | aroma (C6) | 1.20 | 2.40 | 4.00 | 1.20 | 2.40 | 4.00 | 1.80 | 3.20 | 5.00 |
| | taste (C7) | 1.60 | 3.00 | 4.00 | 2.40 | 4.00 | 5.00 | 2.40 | 4.00 | 5.00 |

**Table 7** Value of positive and negative ideal solutions

| Criteria | | $S^+$ | $S^-$ |
|---|---|---|---|
| **Simplah oil** | colour (C1) | (1.33, 2.50, 4.00) | (1.33, 2.50, 4.00) |
| | aroma (C2) | (1.80, 3.20, 5.00) | (1.20, 2.40, 3.00) |
| **Pliek oil** | colour (C3) | (1.20, 2.40, 4.00) | (0.80, 1.80, 3.20) |
| | aroma (C4) | (1.80, 3.20, 5.00) | (1.20, 2.40, 4.00) |
| **Pliek-U** | colour (C5) | (1.60, 3.00, 4.00) | (1.20, 2.40, 4.00) |
| | aroma (C6) | (1.80, 3.20, 5.00) | (1.20, 2.40, 4.00) |
| | taste (C7) | (2.40, 4.00, 5.00) | (1.60, 3.00, 4.00) |

the lower the pH value. This is in line with the statement of Khathir et al. (2018), who stated that the fermentation process tends to increase the acidic taste, which is characterized by a decrease in pH value.

### Stage 2

The next step to determine the alternative priorities for the coconut fermentation method was to collect the preferences of respondents' choices, which were translated into lower, middle, and upper boundary values. After compiling a matrix of respondents' evaluation of various alternative methods of coconut fermentation (Table 4), the respondents' evaluation data were then converted into TFN linguistic data (Table 5).

### Stage 3

The next step was to aggregate the TFN value into weighting interests and normalizing of weighting interests. Furthermore, a multiplication matrix between the criteria weight and normalization value of each alternative fermentation method was arranged (Table 6).

### Stage 4

The next step was to determine the value of the positive ideal solution (FPIS) $S^+$ and the value of the negative ideal solution (FNIS) $S^-$ (Table 7).

### Stage 5

The next stage was to calculate the value of distance between each alternative value with the value of a positive ideal solution and the value of a negative ideal solution. The results of these calculations are given in Table 8.

Based on the comparison of $d^+$ and $d^-$ conducted to evaluate the value of the criteria distance with Fuzzy Positive Ideal Solution (FPIS) and Fuzzy Negative Ideal Solution (FNIS), a radar diagram (Fig. 1) was plotted – it shows the

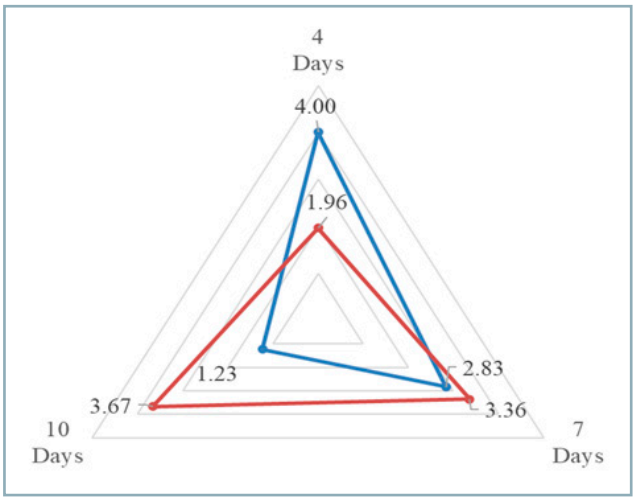


**Fig. 1** Evaluation of $d^+$ and $d^-$

product acceptance preferences. It is obvious that the 7-day fermentation treatment showed the $d^+$ and $d^-$ values with the smallest distance from the positive and negative ideals, while the 10-day fermentation treatment showed the $d^+$ and $d^-$ values with the greatest distance from the positive and negative ideals.

Dashti et al. (2010) explained that the principle used in the TOPSIS method is that the chosen alternative must have the shortest distance from the positive ideal solution and the farthest from the negative ideal solution to determine the relative closeness of an alternative to the optimal solution.

### Stage 6

The last step was to calculate the value of relative closeness preference to the ideal solution (closeness coefficient – $CC_i$) of each alternative (Table 9).

**Table 8** Value of the distance between the criteria value with FPIS and FNIS

| Criteria | | FPIS ($d^+$) | | | FNIS ($d^-$) | | |
|---|---|---|---|---|---|---|---|
| | | 4 days | 7 days | 10 days | 4 days | 7 days | 10 days |
| Simplah oil | colour (C1) | 0.38 | 0.38 | 0.00 | 0.38 | 0.38 | 0.00 |
| | aroma (C2) | 1.24 | 0.82 | 0.00 | 0.35 | 1.00 | 1.29 |
| Pliek oil | colour (C3) | 0.62 | 0.00 | 0.00 | 0.00 | 0.62 | 0.62 |
| | aroma (C4) | 0.00 | 0.82 | 0.82 | 0.82 | 0.00 | 0.00 |
| Pliek-U | colour (C5) | 0.00 | 0.00 | 0.42 | 0.42 | 0.42 | 0.00 |
| | aroma (C6) | 0.82 | 0.82 | 0.00 | 0.00 | 0.00 | 0.82 |
| | taste (C7) | 0.94 | 0.00 | 0.00 | 0.00 | 0.94 | 0.94 |
| $d^+$ and $d^-$ | | 4.00 | 2.83 | 1.23 | 1.96 | 3.36 | 3.67 |

**Table 9** Closeness and alternative ranking coefficients

| | Fermentation alternatives | | |
|---|---|---|---|
| | 4 days | 7 days | 10 days |
| $CC_i$ | 0.3291 | 0.5425 | 0.7484 |
| Ranking | 3 | 2 | 1 |

Based on the calculation results of relative closeness preference value of each alternative in Table 9, it appears that the10-day fermentation method had the greatest value of 0.7484. The alternative fermentation method, which has the largest coefficient value, is the main alternative that is recommended to be selected or prioritized compared to other alternatives based on the preferences of the respondents' choices (product acceptance). Based on the value of the closeness coefficient ($CC_i$), an alternative ranking method of fermentation can be formed, arranging the fermentation methods from the largest to the smallest $CC_i$ value:

1. 10-day coconut fermentation,
2. 7-day coconut fermentation,
3. 4-day coconut fermentation.

The 10-day alternative fermentation method had the shortest or closest distance to the positive ideal solution – 1.23, and the distance to the farthest negative ideal solution was 3.67. Fuzzy-TOPSIS method is based on the concept of using multi-criteria decision-making methods or alternative choices, which are alternatives that have the shortest distance from the positive ideal solution and the longest distance from the negative ideal solution. According to Pochampally et al. (2004), the best alternative is determined based on ranking preference on the value of closeness coefficient ($CC_i$).

Based on the analysis of results using the fuzzy-TOPSIS approach in the aforementioned steps, 10-day coconut fermentation method is the main and ideal according to the preferences of respondents from among the observed alternative methods of coconut fermentation.

## Conclusion

Sensory evaluation analysis of Pliek-U quality using the fuzzy-TOPSIS method was able to find the most ideal or prime alternative of coconut fermentation treatment from the 3 alternatives considered. Based on the fuzzy-TOPSIS method approach, the highest closeness coefficient value 0.7484 was obtained by the 10-day coconut fermentation alternative. Furthermore, the quality of Pliek-U produced using 10-day fermentation treatment showed a higher level of product acceptance than the quality of Pliek-U produced using 4-day and 7-day coconut fermentation treatments. Ultimately, respondents also preferred Simplah oil, Pliek oil, and Pliek-U produced utilizing the 10-day fermentation treatment.

## Acknowledgement

This work was supported by Universitas Syiah Kuala, the Ministry of Education and Culture, Republic of Indonesia, Penelitian Lektor No. 270/UN11/SPK/PNBP/2020.

## References

AGUSTINA, R. – MUNAWAR, A. A. 2019. Electro-optic properties of dried Pliek-U powder: local ingredients from Aceh. In IOP Conference Series: Earth and Environmental Sciences, vol. 365.

BORAN, E. – GENÇ, S. – KURT, M. – AKAY, D. 2009. A multi-criteria intuitionistic fuzzy group decision making for supplier selection with topsis method. In Expert Systems with Applications, vol. 36, no. 8, pp. 11363–11368.

DASHTI, Z. – PEDRAM, M. M. – SHANBEHZADEH, J. 2010. A multi-criteria decision making based method for ranking sequential patterns. In Proceedings of International Multi-Conference of Engineers and Computer Scientist, Hongkong, vol. 1.

FADHIL, R. – MAARIF, M. S. – BANTACUT, T. – HERMAWAN, A. 2017a. Multi criteria decision support system for the development of Gayo coffee agroindustry using fuzzy-eckenrode and fuzzy-topsis approaches. In Jurnal Teknologi Industri Pertanian, vol. 27, no. 1, pp. 103–113. (In Indonesian: Sistem penunjang keputusan multi kriteria untuk pengembangan agroindustri kopi gayo menggunakan pendekatan fuzzy-eckenrode dan fuzzy-topsis).

FADHIL, R. – MAARIF, M. S. – BANTACUT, T. – HERMAWAN, A. 2017b. Comparison of multi-criteria decision making techniques between the eckenrode method and the fuzzy eckenrode method on agro-industry performance. In Jurnal Manajemen & Agribisnis, vol. 14, no. 2, pp. 109–117. (In Indonesian: Perbandingan teknik pengambilan keputusan multi-kriteria antara metode eckenrode dengan metode fuzzy eckenrode pada kinerja agroindustri).

FADHIL, R. – AGUSTINA, R. – MUSTAQIMAH. 2019. A multi-criteria sensory assessment of curcumis melo L. using fuzzy-eckenrode and fuzzy-topsis methods. In Journal Foods and Raw Materials, vol. 7, no. 2, pp. 339–347.

HALICKA, K. 2020. Technology selection using the topsis method. In Foresight and STI Governance, vol. 14, no. 1, pp. 85–96.

HAMILTON, M. L. – JACOB, L. 2020. Fast and automated sensory analysis: using natural language processing for descriptive lexicon development. In Food Quality and Preference, vol. 83.

HLAVÁČ, P. – BOŽIKOVÁ, M. – PETROVIC, A. 2019. Selected physical properties assessment of sunflower and olive oils. In Acta Technologica Agriculturae, vol. 22, no. 3, pp. 86–91.

HWANG, C. L. – YOON, K. 1981. Multiple Attributes Decision Making Methods and Applications. Springer, Berlin, Heidelberg. ISBN 978-3-642-48318-9.

CHAUHAN, V. S. – SHARMA, A. 2003. Studies on organoleptic properties of food products from fresh egg and egg powder through principal component analysis. In Molecular Nutrition Food Research, vol. 47, no. 2, pp. 102–105.

KHATHIR, R. – AGUSTINA, R. – BASYIR, F. 2018. Study of the fermentation process in the processing of Pliek U. In Prosiding Seminar Nasional. Pembangunan Berbasis Kearifan Lokal (Local Wisdom). Banda Aceh, pp. 277–284. (In Indonesian: Kajian proses fermentasi pada proses pengolahan Pliek U).

KHATHIR, R. – AGUSTINA, R. – HARTUTI, S. – FAHMI, Z. 2020. Improving fermented virgin coconut oil quality by using microwave heating. In IOP Conference Series: Earth and Environmental Science, vol. 425.

LAWLESS, H. T. – HEYMANN, H. 2010. Sensory Evaluation of Food. In Springer New York Dordrecht Heidelberg London. ISBN 978-1-4419-6487-8.

MUSTAQIMAH – AGUSTINA, R. – FADHIL, R. – ZUHDI, I. – DEVIANTI. 2019. Study on physical characteristics of Pliek-U: comparisons among fermentation stages. In IOP Conference Series: Earth and Environmental Sciences, vol. 365.

PAPILO, P. – DJATNA, T. – ARKEMAN, Y. – MARIMIN. 2018. The application of fuzzy topsis in determining the location of the development area of the palm oil bioenergy supply chain. In Jurnal Agritech, vol. 38, no. 1, pp. 79–87. (In Indonesian: Penerapan fuzzy topsis dalam penentuan lokasi kawasan pengembangan rantai pasok bioenergy kelapa sawit).

POCHAMPALLY, K. K. – GUPTA, S. M. – KAMARTHI, S. V. 2004. Evaluation of production facilities in a closed-loop supply chain: a fuzzy topsis approach. In S. M. Gupta (Ed.). In Environmentally Conscious Manufacturing III, vol. 5262, pp. 125–138.

POPOV-RALJIC, J. V. – LALICIC-PETRONIJEVIC, J. G. 2009. Sensory properties and color measurements of dietary chocolates with different compositions during storage for up to 360 days. In Sensors, vol. 9, no. 3, pp. 1996–2016.

ROHAYA, S. – ERFIZA, N. M. – AMANDA, V. – SULAIMAN, I. 2019. Optimization of instant Pliek-U (fermented coconut meat) production using kinetic dryer. In IOP Conference Series: Materials Science and Engineering, vol. 536.

ROUHANI, S. – GHAZANFARI, M. – JAFARI, M. 2012. Evaluation model of business intelligence for enterprise system using fuzzy TOPSIS. In Journal Expert System with Applications, vol. 39, pp. 3764–3771.

ROUYENDEGH, B. D. – YILDIZBASI, A. – YILMAZ, I. 2020. Evaluation of retail industry performance ability through integrated intuitionistic fuzzy TOPSIS and data envelopment analysis approach. In Soft Computing, vol. 24, pp. 12255–12266.

SHINDU, M. S. – RASHID, T. – KHASIF, A. 2019. Modeling of linear programming and extended TOPSIS in decision making problem under the framework of picture fuzzy sets. In Plos One, vol. 14, no. 8, pp. 1–13.

SIRANGELO, T. M. 2019. Sensory descriptive evaluation of food products: a review. In Journal of Food Science and Nutrition Research, vol. 2, no. 4, pp. 354–363.

TULKHAH, A. – SAIFUDDIN, A. 2019. Fuzzy topsis to improve the accuracy and objectivity of the weight in the vendor selection of PT.Telkomsel TTC BSD. In Jurnal Informatika Universitas Pamulang, vol. 4, no. 1, pp. 28–34. (In Indonesian: Fuzzy topsis untuk meningkatkan akurasi dan objektivitas bobot pada seleksi vendor PT. Telkomsel TTC BSD).

UMUDEE, I. – CHONGCHEAWCHAMNAN, M. – KIATWEERASAKUL, M. –TONGURAI, C. 2013. Sterilization of oil palm fresh fruit using microwave technique. In International Journal of Chemical Engineering and Applications, vol. 4, no. 3, pp. 111–113.

VIEIRA, T. M. F. S. – REGITANO-D'ARCE, M. A. B. 1998. Stability of oils heated by microwave: UV-spectrophotometric evaluation. In Journal of Food Science and Technology, vol. 18, no. 4, pp. 433.

YOON, K. 1980. System selection by multiple attribute decision making. Ph.D. Dissertation. Kansas State University, Manhattan, Kansas.

YOON, K. P. – KIM, W. K. 2017. The behavioral TOPSIS. In Expert Systems with Applications, vol. 89, pp. 266–272

YAZDI, M. – KORHAN, O. – DANESHVAR, S. 2020. Application of fuzzy fault tree analysis based on modified fuzzy AHP and fuzzy TOPSIS for fire and explosion in the process industry. In International Journal of Occupational Safety and Ergonomics, vol. 26, no. 2, pp. 319–335.

sciendo

DOI: 10.2478/ata-2020-0027



Acta Technologica Agriculturae 4
Nitra, Slovaca Universitas Agriculturae Nitriae, 2020, pp. 168–175

# OPTIMIZATION OF THE MIXING RATIO FOR PARTICLEBOARD PRODUCTION FROM GROUNDNUT SHELL AND RICE HUSK

Olamide OLAWALE[1]*, Banjo A. AKINYEMI[2], Favourite ATTABO[2]

[1]Chemical Engineering Department, Landmark University, Omu-Aran; Kwara State, Nigeria
[2]Agriculture and Biosystems Engineering, Landmark University, Omu-Aran; Kwara State, Nigeria

The aim of this work is to optimize the mixing ratio for production of particleboard (PB) from groundnut shell and rice husk. This research is focused on optimization approach for turning the agricultural waste into quality value-added composite PB for sustainable development. Box-Behnken design was used to optimize the effect of three process variables: groundnut husk (0–100 g); rice husk (0–100 g) and resin (1.5–2.5 g). The best process levels for PB production predicted by the software were validated. The PB samples produced were analysed using scanning electron microscope. The best results were obtained at levels: groundnut husk – 50 g; rice husk –100 g; resin – 3.50 g with rupture modulus of 3.50 N·mm$^{-2}$ and elasticity modulus of 932.4 N·mm$^{-2}$, the predicted optimal levels of 65.99 g; 86.34 g and 1.69 g were validated. The validation results gave rupture modulus of 3.49 N·mm$^{-2}$, and elasticity modulus of 932.10 N·mm$^{-2}$. It can be concluded that PB produced at the optimized conditions satisfied the American National Standard ANSI/A208.1-999 specification for general purpose particleboards for sustainable development.

**Keywords:** Box-Behnken design; ANOVA; regression; elasticity modulus; rupture modulus

The reserves of indigenous plant species have declined due to the rise in wood consumption, leading to a search for new lignocellulosic products that can successfully meet the demand. The 95% of lignocellulosic components used in PB manufacturing is wood. Abdulkareem and Adeniyi (2017) noted that the wood alternatives, such as agricultural residues and non-wood crops, have started to play an essential role in this field (Idris et al., 2011; Ezenwa et al., 2019). Prominent agricultural residues include cereal straw; bagasse sugar cane; cornstalks and cobs; stalks of cotton; seeds of sunflower (Fiorelli et al., 2016); rice husk (Madu et al., 2018; Akinyemi et al., 2020); rice straw (Matías et al., 2019); cassava peels (Villamizar et al., 2012); coir pith (Ahmed et al., 2016); red iron wood (Akinyemi et al., 2019a); sawdust (Akinyemi et al., 2019b; Atuanya et al., 2016); and palm kernel shells (Akinyemi et al., 2016). PB is widely used for flooring, wall bracing, ceiling, furniture, partitioning and cladding purposes (Olorunmaiye and Ohijeagbon, 2015; Chibudike et al., 2011). However, the panel/board industry has encountered continuous growth in developing countries, such as Nigeria, over the previous few years and the demand for panels/boards rapidly increased, what placed a lot of pressure on forest resources, resulting in deforestation and its corresponding negative effects on the environment, as well as increased timber prices (Sotannde et al., 2012). For this very reason, major focus has been put on the development of composite materials from agricultural waste as an alternative particleboard to timber-based products. The composite materials are held together by synthetic resins and other additives, which may be added to enhance the final composite material properties. Several resin types are widely used, the cheapest is urea formaldehyde and phenol formaldehyde resins (Akindapo et al., 2015).

One of the major causes of environmental pollution is the rapid depletion of forest raw resources. Furthermore, to reduce forest exploitation, it is vital to explore alternative sources of raw materials. It is thus crucial to explore the suitability of agricultural residues for PB production, since it would be more eco-friendly and promote the waste to prosperity concept in construction sector. This would protect the environment and promote eco-friendly techniques (Bektas et al., 2015). Numerous authors have dealt with the issue of PB production from agricultural wastes: Mendes et al. (2009) investigated coffee husks and hull fibres; Sarkar et al. (2012) and Madu et al. (2018) observed rice husk and saw-dust; Suleiman et al. (2013) researched the rice husk PBs reinforced with Gum Arabic and formaldehyde; Amenaghawon et al. (2016) studied corn cobs and cassava leaves. However, there is a scarcity of information on the impacts of control variables, such as the amounts of agro-residue composites and urea formaldehyde resin, on the mechanical PB properties (Amenaghawon et al., 2016). The research presented hence investigates the use of groundnut shell and rice husk as a composite material for PB production using optimization approach.

**Contact address:** Olamide Olawale, Chemical Engineering Department, Landmark University, Omu-Aran; Kwara State, Nigeria; e-mail: olawale.olamide@lmu.edu.ng

## Material and methods

The materials used included groundnut shell; rice husk (collected from Landmark University, Commercial farm); and binder (urea formaldehyde).

### Experimental design

The experimental design was conducted by means of Box-Behnken design in the 6.0.8 Design Expert software in order to determine the interaction effect of three variables (groundnut shell content, rice husk content and urea formaldehyde content). The range and levels of independent variables are shown in Table 1. The matrix for the three variables was varied at 3 levels (-1, 0 and +1) as shown in Table 2. The Box-Behnken design has been established to be suitable for the quadratic response surfaces and this design generated a second-degree polynomial model (Amenaghawon et al., 2014), in which $Y_i$ is a dependent variable or predicted response; $X_i$ and $X_j$ are independent variables; $b_0$ is an offset term; $b_i$ and $b_{ij}$ are the single and interaction effect coefficients; and $e_i$ is the error term. The Design Expert software was used for the regression and graphical analysis of experimental data. The responses analysed were elasticity modulus (*MOE*) and rupture modulus (*MOR*). Design Matrix for the PB production from groundnut shell and rice husk is shown in Table 2.

### Production of particleboards

Waste materials were cleaned, washed, air dried to reduce its moisture content and milled to reduce the particle size. The groundnut shell and rice husk were separated using standard sieve sizes into two different group sizes (0.85 mm and 1.7 mm). PB after moulding is shown in Figs. 1 and 2.

Digital weighing balance was used for weighing of variables via the interactions generated by the experimental design. Subsequently, materials were thoroughly mixed with binder in a mixing bowl. Polythene nylon was used to cover the resulting homogeneous mixture. Cold and hot compression was performed on the boards using a hydraulic press and pressing was retained for 24 h prior to release of the compacting pressure. The boards were dried at temperature of approx. 80 °C. PBs were then subjected to mechanical and physical tests.

**Table 1** Coded and actual levels of the variables

| Independent variables | | Coded and actual levels | | |
|---|---|---|---|---|
| | symbols | -1 | 0 | +1 |
| Amount of groundnut shell (g) | $X_1$ | 0 | 50 | 100 |
| Amount of rice husk (g) | $X_2$ | 0 | 50 | 100 |
| Resin loading (g) | $X_3$ | 1.5 | 2.0 | 2.5 |

**Table 2** Design matrix for the PB production from groundnut shell and rice husk

| Std | Run | Coded variables | | | Groundnut actual | Rice husk | Resin loading |
|---|---|---|---|---|---|---|---|
| | | $X_1$ | $X_2$ | $X_3$ | $X_1$ | $X_2$ | $X_3$ |
| 16 | 1 | 1 | -1 | 0 | 100 | 0 | 2.0 |
| 7 | 2 | 0 | 1 | -1 | 50 | 100 | 1.5 |
| 9 | 3 | 0 | 0 | 0 | 50 | 50 | 2.0 |
| 12 | 4 | 0 | 1 | 1 | 50 | 100 | 2.5 |
| 4 | 5 | 0 | -1 | -1 | 50 | 0 | 1.5 |
| 11 | 6 | 1 | 0 | 1 | 100 | 50 | 2.5 |
| 8 | 7 | -1 | 0 | -1 | 0 | 50 | 1.5 |
| 14 | 8 | -1 | 0 | 1 | 0 | 50 | 2.5 |
| 5 | 9 | -1 | -1 | 0 | 0 | 0 | 2.0 |
| 17 | 10 | 1 | 0 | -1 | 100 | 50 | 1.5 |
| 10 | 11 | 0 | 0 | 0 | 50 | 50 | 2.0 |
| 1 | 12 | 0 | 0 | 0 | 50 | 50 | 2.0 |
| 15 | 13 | 0 | -1 | 1 | 50 | 0 | 2.5 |
| 13 | 14 | 0 | 0 | 0 | 50 | 50 | 2.0 |
| 6 | 15 | 1 | 1 | 0 | 100 | 100 | 2.0 |
| 3 | 16 | -1 | 1 | 0 | 0 | 100 | 2.0 |
| 2 | 17 | 0 | 0 | 0 | 50 | 50 | 2.0 |

**Fig. 1** Particleboards after moulding

### Particleboard testing

#### Laboratory test

The elasticity modulus (*MOE*) and rupture modulus (*MOR*) of samples showed a rate of 10 mm·min$^{-1}$ when observed by universal testing machine Testometric M500-50AT. The experiments were performed at ambient room temperature (25 ±1 °C), with each sample at a slack of 80 mm-·min$^{-1}$ depending on the varying PB density and width. The *MOE* and *MOR* were calculated as follows:

$$MOR = \frac{3PL}{2bh^2} \quad \left(\mathrm{N \cdot mm^{-2}}\right) \tag{1}$$

$$MOR = \frac{PL^3}{4bh^3Y} \quad \left(\mathrm{N \cdot mm^{-2}}\right) \tag{2}$$

where:
*P* – maximum load or maximum force
*L* – span
*b* – width
*h* – height
*Y* – deflect

Thermal conductivity test was performed using hot-disk transient plane source, and SEM analysis was performed using a JEOL model machine.

## Results and discussion

### Statistical analysis

Box-Behnken designs for responses obtained for *MOR* and *MOE* are shown in Table 3. The Eqs. 3 and 4 are models obtained from the response via the regression analysis in terms of coded terms:


**Fig. 2** Particleboards during flexural strength test

$$MOR = 3.01 + 0.50X_1 + 1.01X_2 + 1.85X_3 + 0.036X_1X_2 - 0.18X_1X_3 - 0.24X_2X_3 + 0.33X_1^2 - 0.16X_2^2 - 1.24X_2^3 \quad (\mathrm{N \cdot mm^{-2}}) \tag{3}$$

$$MOE = 891.5 - 3.93X_1 + 123.29X_2 + 9.06X_3 - 2.19X_1X_2 + 1.19X_1X_3 - 132.33X_2X_3 - 16.84X_1^2 - 68.31X_2^2 - 67.23X_2^3 \quad (\mathrm{N \cdot mm^{-2}}) \tag{4}$$

Furthermore, Table 4 shows the ANOVA for *MOR* and Table 5 shows ANOVA for *MOE*.

Tables 4 and 5 revealed that the models for *MOR* and *MOE* were statistically significant with p values of 0.0004 and 0.0057, respectively. However, the models showed that the terms representing the amounts of groundnut shell, rice husk and resin loading were significant by indicating that all variables influenced the *MOR* and *MOE* of the boards produced. The F values of 19.67 for *MOR* and 8.13 for *MOE* showed that the models generated were significant. Statistical information for ANOVA showed that models describing the *MOR* and *MOE* have high coefficient of determination ($R^2$) as shown in Table 6. Moreover, Table 6 indicates that the models were able to adequately represent the relationship between the selected factors (content of variables) and responses (*MOR* and *MOE*); $R^2$ of 0.96 and 0.91 for the *MOR* and *MOE*, respectively, suggests that the models were able to explain 96% and 91% of the variability observed in the *MOR* and *MOE* values, respectively. The results observed showed a high reliability as recommended by Montgomery (2005). The adequate precision for both models indicate that these models can be used to navigate the design space (Cao et al., 2009).

### Results of 3D surface plots

The impacts of resin loading and groundnut shell content on the *MOR* of PBs are given in Fig. 3. Observed trends showed that the *MOR* increased concurrently with enhanced quantities of resin and groundnut shell. This complies with observation of other researchers – Murakami et al. (1999) reported that the mechanical and physical properties of PBs can be increased. The amount of vacuum present in boards was assessed by the resin loading as reported by Sekaluvu et al. (2014). Optimal volumes of groundnut shell and rice husk were used to produce the boards with high *MOR* values, suggesting that the mechanical properties can be improved by application of higher resin contents. Made of a hygroscopic material, the board will tend to absorb the moisture when placed in a humid environment. The moisture content of tested board is 3%. The boards produced are not

**Table 3** Box-Behnken design for response (*MOR* and *MOE*)

| Run | Factors | | | | | | Response | | | |
|---|---|---|---|---|---|---|---|---|---|---|
| | coded values | | | actual values | | | *MOR* (N·mm$^2$) | | *MOE* (N·mm$^2$) | |
| | $X_1$ | $X_2$ | $X_3$ | $X_1$ | $X_2$ | $X_3$ | actual | predicted | actual | predicted |
| **1** | 1 | -1 | 0 | 100 | 0 | 2.0 | 2.28 | 2.25 | 576.5 | 599.0 |
| **2** | 0 | 1 | -1 | 50 | 100 | 1.5 | 3.50 | 3.69 | 932.4 | 946.0 |
| **3** | 0 | 0 | 0 | 50 | 50 | 2.0 | 2.45 | 3.19 | 732.4 | 822.3 |
| **4** | 0 | 1 | 1 | 50 | 100 | 2.5 | 2.14 | 2.10 | 360.8 | 429.5 |
| **5** | 0 | -1 | -1 | 50 | 0 | 1.5 | 0.43 | 0.47 | 492.5 | 423.8 |
| **6** | 1 | 0 | 1 | 100 | 50 | 2.5 | 1.74 | 1.96 | 680.2 | 671.3 |
| **7** | -1 | 0 | -1 | 0 | 50 | 1.5 | 2.99 | 2.77 | 764.7 | 773.6 |
| **8** | -1 | 0 | 1 | 0 | 50 | 2.5 | 2.36 | 2.38 | 678.0 | 631.8 |
| **9** | -1 | -1 | 0 | 0 | 0 | 2.0 | 2.13 | 2.31 | 494.2 | 554.0 |
| **10** | 1 | 0 | -1 | 100 | 50 | 1.5 | 3.38 | 3.86 | 760.1 | 806.3 |
| **11** | 0 | 0 | 0 | 50 | 50 | 2.0 | 3.38 | 3.19 | 845.0 | 822.3 |
| **12** | 0 | 0 | 0 | 50 | 50 | 2.0 | 3.38 | 3.19 | 844.3 | 822.3 |
| **13** | 0 | -1 | 1 | 50 | 0 | 2.5 | 0.47 | 0.27 | 677.1 | 663.5 |
| **14** | 0 | 0 | 0 | 50 | 50 | 2.0 | 3.38 | 3.19 | 845.0 | 822.3 |
| **15** | 1 | 1 | 0 | 100 | 100 | 2.0 | 5.10 | 4.92 | 794.0 | 734.2 |
| **16** | -1 | 1 | 0 | 0 | 100 | 2.0 | 4.66 | 4.69 | 729.6 | 707.1 |
| **17** | 0 | 0 | 0 | 50 | 50 | 2.0 | 3.38 | 3.19 | 845.0 | 822.3 |

**Table 4** ANOVA results for model representing *MOR*

| Sources | Sum of squares | *Df* | Mean squares | *F*-value | *P*-value |
|---|---|---|---|---|---|
| **Model** | 23.65 | 9 | 2.63 | 19.67 | 0.0004 |
| $X_1$ | 1.07 | 1 | 1.07 | 8.00 | 0.0255 |
| $X_2$ | 4.31 | 1 | 4.31 | 32.26 | 0.0008 |
| $X_3$ | 3.07 | 1 | 3.07 | 22.98 | 0.0020 |
| $X_1X_2$ | 0.021 | 1 | 0.021 | 0.16 | 0.7034 |
| $X_1X_3$ | 0.26 | 1 | 0.26 | 1.91 | 0.2096 |
| $X_2X_3$ | 0.49 | 1 | 0.49 | 3.67 | 0.0970 |
| $X_1^2$ | 1.86 | 1 | 1.86 | 13.96 | 0.0073 |
| $X_2^2$ | 0.42 | 1 | 0.42 | 3.17 | 0.1184 |
| $X_3^2$ | 6.50 | 1 | 6.50 | 48.61 | 0.0002 |
| **Residual** | 0.94 | 7 | 0.13 | – | – |
| **Lack of fit** | 0.24 | 3 | 0.081 | 0.47 | 0.7200 |
| **Pure error** | 0.69 | 4 | 0.17 | – | – |
| **Cor total** | 24.59 | 16 | – | – | – |

**Table 5** ANOVA results for model representing *MOE*

| Sources | Sum of squares | *Df* | Mean squares | *F*-value | *P*-value |
|---|---|---|---|---|---|
| **Model** | 3.397 | 9 | 37,745.94 | 8.13 | 0.0057 |
| $X_1$ | 65.38 | 1 | 65.38 | 0.014 | 0.9089 |
| $X_2$ | 64,224.00 | 1 | 64,224.00 | 13.83 | 0.0075 |
| $X_3$ | 73.29 | 1 | 73.29 | 0.016 | 0.9036 |
| $X_1X_2$ | 80.10 | 1 | 80.10 | 0.017 | 0.8992 |
| $X_1X_3$ | 11.56 | 1 | 11.56 | 2.189E-003 | 0.9616 |
| $X_2X_3$ | 1.430E + 005 | 1 | 1.430E + 005 | 30.77 | 0.0009 |
| $X_1^2$ | 4,970.26 | 1 | 4,970.26 | 1.07 | 0.3354 |
| $X_2^2$ | 81,829.27 | 1 | 81,829.27 | 17.62 | 0.0041 |
| $X_3^2$ | 19,032.46 | 1 | 19,032.46 | 4.10 | 0.0826 |
| **Residual** | 32,517.55 | 7 | 4,645.36 | – | – |
| **Lack of fit** | 22,405.68 | 3 | 7,468.56 | 2.95 | 0.1613 |
| **Pure error** | 10,111.87 | 4 | 2,527.97 | – | – |
| **Cor total** | 3.722E + 005 | 16 | – | – | – |

**Table 6** Statistical information for ANOVA

| Parameter | Value | |
|---|---|---|
| | *MOR* | *MOE* |
| **R-squared** | 0.96 | 0.91 |
| **Mean** | 2.77 | 708.93 |
| **Standard deviation** | 0.37 | 68.16 |
| **C.V %** | 13.18 | 9.61 |
| **Adeq. precision** | 16.57 | 9.99 |

suitable for environments with higher relative humidity; however, these can be used as insulation boards. Fig. 4 shows the importance of resin loading and rice husk volume on the *MOR*. On the contrary, Fig. 5 shows that there was an increase in *MOE* with usage of small contents of rice husk. The resin loading did not influence the *MOR* of boards significantly. However, Fig. 6 shows the effects of the rice husk and groundnut shell contents on the *MOE*. Fig. 7 shows the impacts of resin loading and groundnut shell content on the *MOE*; Fig. 8 shows the effect of resin loading and rice husk content on the *MOE*. Furthermore, there is a correlation of the obtained results with observations made by Sekaluvu et al. (2014), who reported that high-quality bond can result from good contact between resin and agro-residue particles in PBs with *MOE* values. This is because the increased resin loads improve the bond contact between particles, leading

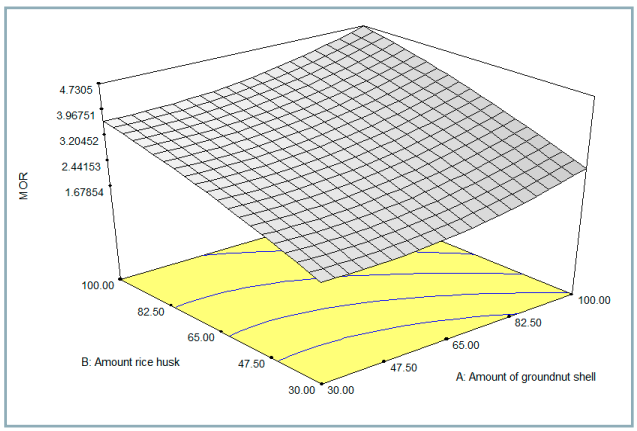


**Fig. 3** Effects of rice husk and groundnut shell contents on *MOR*

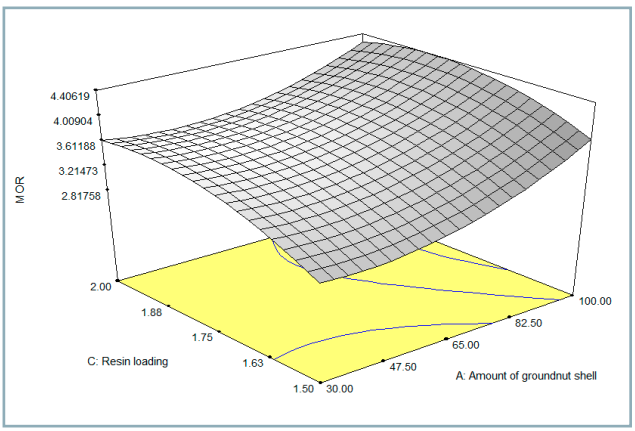


**Fig. 4** Effects of resin loading and groundnut shell content on *MOR*

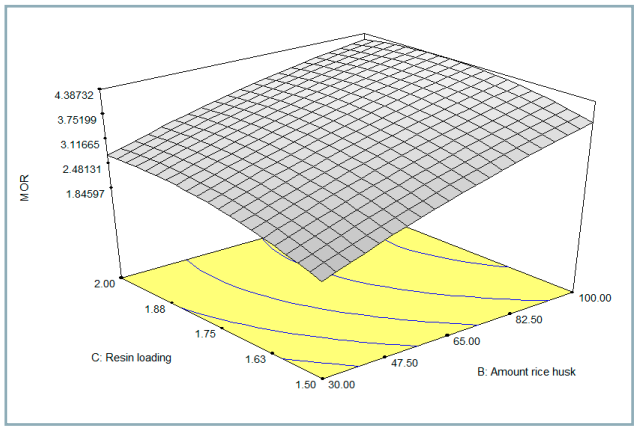


**Fig. 5** Effects of resin loading and rice husk content on *MOR*

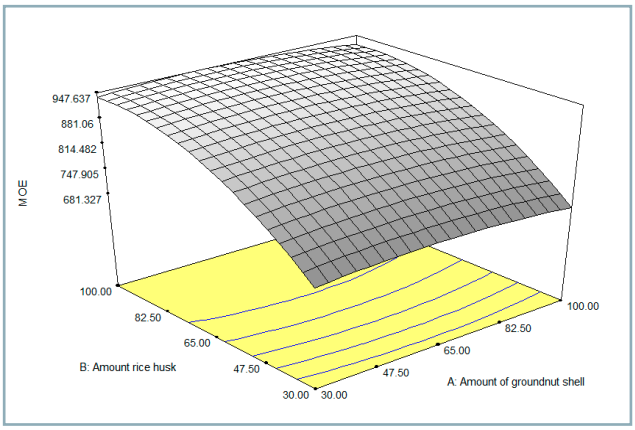


**Fig. 7** Effect of resin loading and amount of groundnut shell on *MOE*

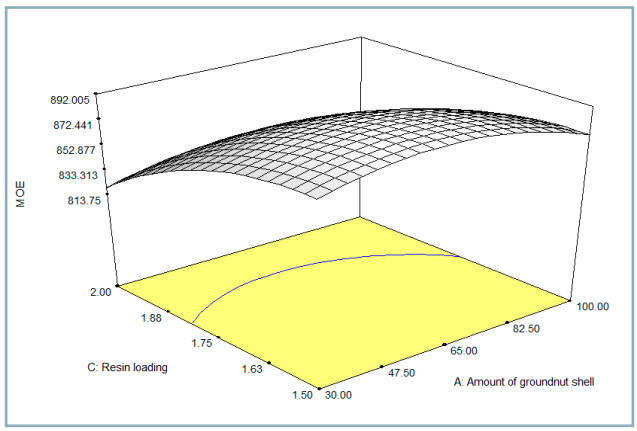


**Fig. 6** Effect of amount of rice husk and amount of groundnut shell on *MOE*

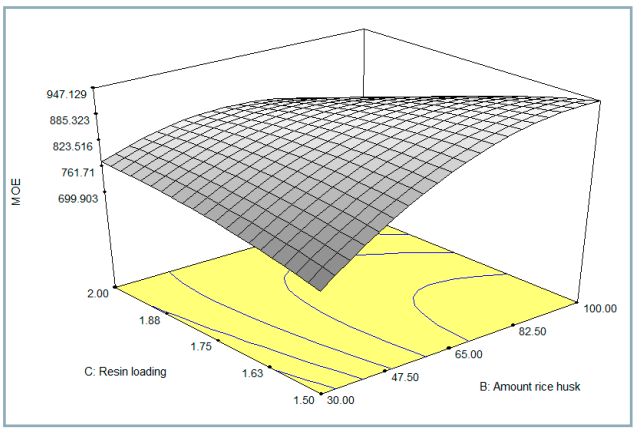


**Fig. 8** Effect of resin loading and amount of rice husk on *MOE*

to enhanced surface contact (Babatunde and Olufemi, 2011). Since both *MOR* and *MOE* are mechanical features, it is expected that the trend observed for both is related. The requirements for PBs made of agro-residues include high values of *MOR* and *MOE*. Derkyi et al. (2008) reported that resin with higher viscosity improved the board bonding strength.

### Validation of optimal predicted levels

The optimal level variables predicted by the software are shown in Table 7, demonstrating a strong correlation between experimental and predicted results. The results indicate that the maximum *MOR* and *MOE* values of 3.50 N·mm$^{-2}$ and 932.40 N·mm$^{-2}$, respectively, were close to those of 3.49 N·mm$^{-2}$ and 932.10 N·mm$^{-2}$.

### Results of surface characterization of PBs via SEM

The optimal and validated particleboards were subjected to SEM and the results observed indicate that the surface of boards showed fibrous network structures, which were covered and bonded by the resin. The boards with higher resin loading showed lower voids, because the resin cured more effectively in the void spaces (Fig. 9). The lower density board (Fig. 10) had higher voids and spaces, which led to high moisture absorptivity. The board density is found to increase with increasing resin loading.

**Table 7** Validated optimal variables

| Solution | Amount of groundnut shell | Amount of rice husk | Resin loading | *MOR* | *MOE* | Desirability |
|---|---|---|---|---|---|---|
| 1 | 65.99 | 86.34 | 1.69 | 3.49 | 932.10 | 1.000 |

**Table 8** Thermal conductivity results

| Room temperature 25 ±1 °C | Thermal conductivity (W·mK$^{-1}$) |
|---|---|
| **G3 (optimal)** | 0.172 |
| **G6 (validated)** | 0.178 |

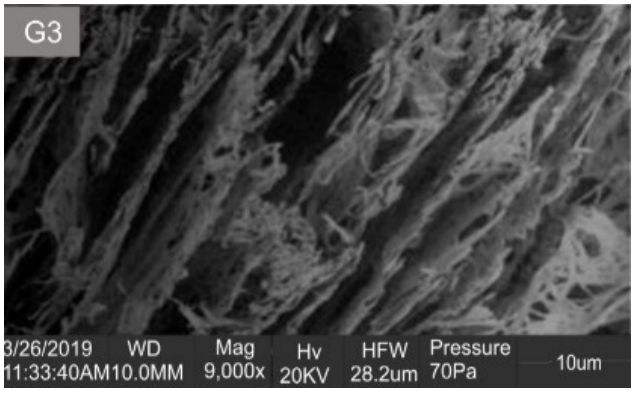


**Fig. 9** Optimal particleboard

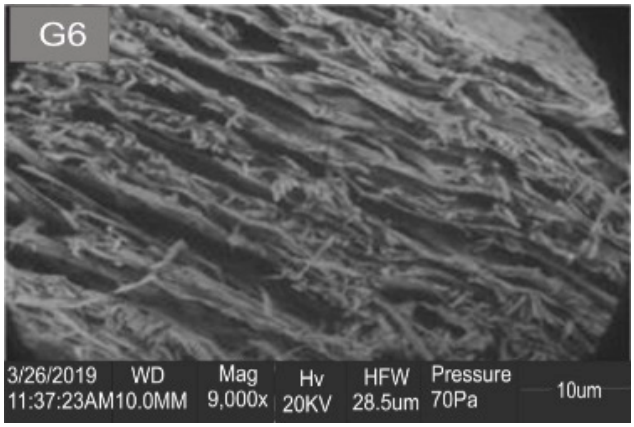


**Fig. 10** Validated particleboard

### Thermal properties analysis

Thermal conductivity results are given in Table 8. These suggest that the PBs do not conduct electricity, what makes them usable as material for switch boards in electrical circuits. The thermal conductivity tests were conducted in accordance with the American Society for Testing Materials (ASTM C177-97).

### Conclusion

Design of experiment for response surface methodology has been demonstrated to be useful in optimizing the board production process. Mechanical properties of boards, such as *MOR* and *MOE*, were influenced by the amount of agro-residues and resin used. The quadratic statistical models developed to represent *MOR* and *MOE* showed a good fit with the experimental data with $R^2$ values of 0.96 and 0.91, respectively. The predicted optimum conditions (65.99 g for groundnut shell; 86.34 g for rice husk; and 1.69 g for resin loading) were validated to show a *MOR* and *MOE* of 3.50 $N{\cdot}mm^{-2}$ and 932.40 $N{\cdot}mm^{-2}$, respectively. The particleboards produced at the optimized conditions satisfied the American National Standard ANSI/A208.1-1999 specification for general purpose particleboards. This study dealt with particleboards produced from groundnut shell and rice husk using urea formaldehyde as binder. Based on the results, it can be concluded that optimization of the amounts of agricultural waste products and resin was successful in terms of the production of particleboards, which are environmentally friendly and easy to manufacture.

### Acknowledgements

The Authors appreciated Landmark University for providing enabling environment for the research.

## References

ABDULKAREEM, S. A. – ADENIYI, A. G. 2017. Production of particleboards using polystyrene and bamboo wastes. In Nigerian Journal of Technology, vol. 36, no. 3, pp. 788–793.

AHMED, E. – DAS, A. K. – HANNAN, M. O. – SHAMS, M. I.2016. Particleboards from coir pith. In Bangladesh Journal of Science and Industrial Residues, vol. 52, no. 3, pp. 239–245.

AKINDAPO, J. O. – BINNI, A. U. – SANUSI, O. M. 2015. Development of roofing sheet materials using groundnut shell particles and epoxy resin as composite material. In American Journal of Engineering Research, vol. 4, no. 6, pp. 165–173.

AKINYEMI, A. B – AFOLAYAN, J. O. – OLUWATOBI, E. O. 2016. Some properties of composite corn cob and sawdust particle boards. In Construction and Building Materials, vol. 127, pp. 436– 441.

AKINYEMI, B. A. – OKONKWO, C. E. – ALHASSAN, E. A. – AJIBOYE, M. 2019a. Durability and strength properties of board from polystyrene-wood wastes. In Journal of Material Cycles and Waste Management, vol. 21, no. 6, pp. 1541–1549.

AKINYEMI, B. A. – OLAMIDE, O. – OLUWASOGO, D. 2019b. Formaldehyde free particleboards from wood chips wastes using modified cassava starch as binder. In Case Studies in Construction Materials, vol. 11, e00236.

AKINYEMI, B. – OMONIYI, T. E. – ELEMILE, O. – OLUWAFEMI, A. 2020. Innovative husk-crete building materials from rice chaff and modified cement mortars. In Acta Technologica Agriculturae, vol. 23, no. 2, pp. 67–72.

AMENAGHAWON, N. A. – OGBEIDE, S. E. – OKIEIMEN, C. O. 2014. Application of statistical experimental design for the optimization of dilute sulphuric acid hydrolysis of cassava bagasse. In Acta Polytechnica Hungarica, vol. 11, pp. 239–250.

AMENAGHAWON, N. A. – OSAYUKI-AGUEBOR, W. – OKIEIMEN, C. O. 2016. Production of particle boards from corncobs and cassava stalks: optimization of mechanical properties using response surface methodology. In Journal of Materials and Environmental Science, vol. 7, no. 4, pp. 1236–1244.

ASTM C177-97. 1999. Standard test method for steady-state heat flux measurements and thermal transmission properties by means of the guarded-hot-plate apparatus. American Society for Testing and Materials.

ANSI A208.1. 2009. Particleboard. American national standard. National Particleboard Association. Retrieved from www.bc.com/.../2014-Boise-CascadePB-vs-ANSI-A208-1-2009.

ATUANYA, C. U. – OBELE, C. M. 2016. Optimization of process parameter for sawdust/recycled polyethylene composites. In Journal of Minerals and Materials Characterization and Engineering, vol. 4, pp. 270–277.

BABATUNDE, B. – OLUFEMI, D. 2011. Properties of cement-bonded flake boards from *Gmelina arborea* and *Leucaena leucocephala*. In International Journal of Biological Chemical Science, vol. 5, no. 2, pp. 586–594.

BEKTAS, I. – GULER, C. – KALAYCIOGLU, H. – MENGELOGLU, F. – NACAR, M. 2005. The manufacture of particleboards using sunflower stalks (*Helianthus annus* I.) and poplar wood (*Populus alba* L). In Journal of Composite Material, vol. 39, no. 5, pp. 467–473.

CAO, G. – REN, N. – WANG, A. – LEE, D. J. – GUO, W. – LIU, B. – FENG, Y. – ZHAO, Q. 2009. Acid hydrolysis of corn stover for biohydrogen

production using *Thermoanaerobacterium thermosaccharolyticum* W16. In International Journal of Hydrogen Energy, vol. 34, no. 17, pp. 7182–7188.

DERKYI, N. – SEKYERE, D. – DARKWA, N. A. – YARTEY, J. G. 2008. Effect of cassava flour as urea-formaldehyde adhesive extender on the bonding strength of plywood. In Ghana Journal of Forestry, vol. 23, pp. 25–34.

EZENWA, O. N. – OBIKA, E. N. – UMEMBAMALU, C. – NWOYE, F. C. 2019. Development of ceiling board using breadfruit seed coat and recycled low density polyethylene. In Heliyon, vol. 5, no. 11, e02712.

FIORELLI, J. – SETORI, D. L. – CRAVO, J. C. M. – SAVASTANO, H. – ROSSIGNOLO, J. A. – NASCIMENTO, M. F. 2016. Sugarcane baggase and castor oil polyurethane adhesive-based composite. In Materials Research, vol. 16, no. 2, pp. 439–446.

CHIBUDIKE, H. O. – ANYAKORA, A. N. – ANYAKORA, A. N. – SULEIMAN, M. A. 2011. Utilization of bamboo in the production of ceiling board. In Journal of Engineering Research, vol. 16, no. 1, pp. 1–10.

IDRIS, U. D. – AIGBODION, V. S. –ATANYA, C. U. – ABDULLAHI, J. 2011. Eco-friendly (watermelon peels): alternatives to wood-based particleboard composites. In Tribology in Industry, vol. 33 no. 4, pp. 173–181.

MADU, O. – NWANKWOJIKE, B. N. –ANI, O. I. 2018. Optimal design for rice husk-saw dust reinforced polyester ceiling board. In American Journal of Engineering Research, vol. 7, no. 6, pp. 11–16.

MATÍAS, J. – CRUZ, V. – GARCÍA, A. – GONZÁLEZ, D. 2019. Evaluation of rice straw yield, fibre composition and collection under Mediterranean conditions. In Acta Technologica Agriculturae, vol. 22, no. 2, pp. 43–47.

MENDES, R. F. – MENDES, L. M. – JUNIOR, J. B. G. – SANTOS, R. C. D. – BUFALINO, L. 2009. The adhesive effect on the properties of particleboards made from sugar cane, bagasse generated in the distiller. In Revista de Ciências Agrárias, vol. 32, no. 2, pp. 209–218.

MONTGOMERY, D. C. 2005. Design and Analysis of Experiments. 6th ed., New York: John Wiley & Sons, Inc.

MURAKAMI, K. K. – UEDA, M. – MATSUDA, H. – ZHANG, M. – KAWASAKI, T. – KAWAI, S. 1999. Manufacture and properties of three-layered particleboards with oriented face strands of veneers. In Journal of the Japan Wood Research Society, vol. 45, no. 5, p. 395–402.

OLORUNMAIYE, J. A. – OHIJEAGBON, J. A. 2015. Retrofitting composite ceiling boards with *Jatropha curcas* seedcake material. In Production Engineering, vol. 18, no. 2, pp. 96–102.

SARKAR, M. – ASHADUZZAMAN, M. – DAS, A. K – SHAMS, M. I. – HANNAN, M. O. 2012. Mechanical properties and dimensional stability of cement bonded particleboard made from saw dust and rice husk. In Bangladesh Journal of Scientific and Industrial Research, vol. 47, no. 3, pp. 273–278.

SEKALUVU, L. – TUMUTEGYEREIZE, P. – KIGGUNDU, N. 2014. Investigation of factors affecting the production and properties of maize cob-particleboards. In Waste and Biomass Valorization, vol. 5, no. 1, pp. 27–32.

SOTANNDE, O. A. – OLUWADARE, A. O. – OGEDOH, O. – ADEOGUN, P. F. 2012. Evaluation of cement-bonded particle board produced from *Afzelia africana* wood residues. In Journal of Engineering Science and Technology, vol. 6, no. 7, pp. 732–743.

SULEIMAN, I. Y. 2013. Development of eco-friendly particleboard composites using rice husk particles and gum Arabic. In Journal of Materials Science and Engineering with Advanced Technology, vol. 7, no. 1, pp. 75–91.

VILLAMIZAR, M. C. N. – ARAQUE, V. S. – REYES, C. A. R. – SILVA, R. S. 2012. Effect of the addition of coal-ash and cassava peels on the engineering properties of compressed earth blocks. In Construction and Building Materials, vol. 36, pp. 276–286.

sciendo

DOI: 10.2478/ata-2020-0028



Acta Technologica Agriculturae 4
Nitra, Slovaca Universitas Agriculturae Nitriae, 2020, pp. 176–182

# MATHEMATICAL MODELLING OF PYROLYSIS OF HARDWOOD (ACACIA)

Alok DHAUNDIYAL[1]*, Suraj B. SINGH[2], Istvan BACSKAI[3]

[1]Institute of Process Engineering, Szent István University, Godollo, Hungary
[2]Govind Ballabh Pant University of Agriculture and Technology, Pantnagar, Uttarakhand, India
[3]Institute of Agricultural Mechanisation, National Agriculture and Innovation Centre, Godollo, Hungary

This paper emphasises the analogous modelling of hardwood (acacia) pyrolysis. The impacts of physical characteristics of hardwood chips on the pyrolysis are examined through the conservation of biomass solid mass fraction. The ONORM standard chips of sizes '*G*30' and '*G*50' and their combination are individually tested in the pyrolysis reactor. In the analogous situation, the fixed bed is assumed to be a wooden slab with a porosity equivalent to the voidage of bed. Bulk density, bed length and porosity are several of the physical attributes of a fixed bed used to examine the variation in the hardwood solid mass across the fixed bed. To measure temperature, the four-temperature sensors separated from each other by 80 mm are fixed along periphery of a reactor. The heating element of 2 kWe is provided to initiate the biomass pyrolysis. The proposed model is also used to establish the relationship between the kinetics of pyrolysis and the structural properties of hardwood.

**Keywords:** pyrolysis; heat transfer; wood chips; physical structure; kinetics

The pyrolysis process plays an important role in comprehending the intrinsic mechanism of combustion of wood and sawdust, since the released products – char and volatile matter – further undergo smouldering (glowing combustion) and flaming (light-emitting) combustion, respectively, to release thermal energy. The quality of char production and generation of volatile matter depends on the physical state of biomass before undergoing thermal decomposition. Therefore, it becomes indispensable to focus on the relationship between the structural properties of biomass and thermal behaviour of biomass. The main aim of any model is to provide a computational inference for examining the system parameters and to recognise the relevance of system characteristics for knowing the system behaviour. Although the complexity of the thermo-chemical process makes the computational process cumbersome, it can be resolved using some cemented steps while formulating the proposed model. The pyrolytic decomposition of wood comprises the series of reactions, therefore, the altering thermal condition or characteristics of fuel may not only influence the rate of reaction but also the pathway of reactions.

The different perspective of modelling is proposed through the application of conservation of energy associated with solid biomass. The relationship between physical and thermal characteristics of wood and their influence on the decomposition process has been highlighted by the analogous scheme. However, the various modelling scheme pivoting around the kinetic aspect of the pyrolysis are summarised in the literature (Dhaundiyal et al., 2018a; Dhaundiyal et al., 2018b; Dhaundiyal et al. 2018c; Cai and Lui, 2008; Dhaundiyal et al., 2019a; Mani et al., 2009). It is assumed that the fixed bed behaves like a porous wooden slab, the length of which sinks with time as a shrinking radius of the particle during combustion (Fogler, 2004). The objective of this study is to evaluate concurrently the thermogravimetric behaviour of the wooden chips with varying physical properties of the system that changes with time and temperature and develop an analogous model under the given thermal conditions for a fixed bed.

## Material and methods

### Modelling scheme

Material characteristics have vital importance during the conceptual stage of modelling. Generally, the thermal parameters (diffusivity and thermal conductivity) directly influence the process of pyrolysis. The physical factors (bulk density and temperature of material) can easily be related to heat and mass transfer properties by the basic experiments. On the other hand, heat conduction through the porous medium varies with the direction of heat flow across the biomass. Therefore, the overall thermal conductivity is the summation of thermal conductivities of the air-void spaces and the solid biomass. Aforementioned process can be followed to measure the heat capacity and the heat transfer coefficient. Wood anisotropy can be known through the fact that permeability of fluid along the grains is $10^4$ times higher than across the grain, whereas thermal conductivity along the grain is twice over the thermal conductivity across the grain (Roberts and Clough, 1963). It is reported that the thermal conductivity of pyrolysed material is a linear function of thermal conductivity of the

**Contact address:** Alok Dhaundiyal, Institute of Process Engineering, Szent István University, Godollo, Hungary;
e-mail: Alok.dext@hotmail.com

virgin wood and char, which is related to an instantaneous density of wood. It is noticed that the temperature and mass loss predictions are sensitive to the assumed value for the thermal conductivity of char (Kung, 1972). However, the measurement of thermal parameters at very high temperature is quite complicated due to chemical alteration and the drastic variation in the physical properties makes computational work much complex. Certain heat and mass transfer models, which combine the chemical kinetics with the application of heat transfer, are proposed to determine the effect of thermal parameters on the thermo-kinetics of material (Maa and Bailie, 1973). One of such models, a volume reaction model, emphasises the simultaneous heat and mass transfer in the particle. In the unreacted shrinking core model for high temperatures (Maa and Bailie, 1973), the reaction at an unreacted shrinking core of solid is initiated by the surrounded pyrolysed layer of material around it. The reaction takes place at the interface of these two solid regions; therefore, the conduction mode plays a major role in dissipation of the thermal energy from the charred layer. The energy transferred during this autocatalytic process varies with the temperature gradient and the radius of the unreacted core. The same energy is utilised to commence pyrolysis in the biomass. The gases produced during pyrolysis advance radially outward. The unsteady rise of temperature inside particles is a time function of porosity, which helps to distinguish the variation of internal energy change of the gas and solid. A gas-solid thermal equilibrium can only be maintained for the low velocity of fluid flow across material (Dhaundiyal et al., 2020). Another aspect of heat transfer is to determine the thermal profile required as an explanatory variable in the kinetic model. Thus, the information on the heat transfer parameters assists in evaluating the accuracy of the prediction of the overall model. Several other models have also incorporated the internal convective heat transfer and temperature dependent thermal conductivity (Witkowski et al., 2016; Sadhukhan et al., 2009; Polesek and Kardas, 2015). In this study, a wooden slab, which is analogous to a fixed bed, is subjected to transfer heat across slab along the length *L*. The schematic diagram of the assumed wooden slab is given in Fig. 1. The length of bed is 80 mm, so the equivalent length of bed with respect

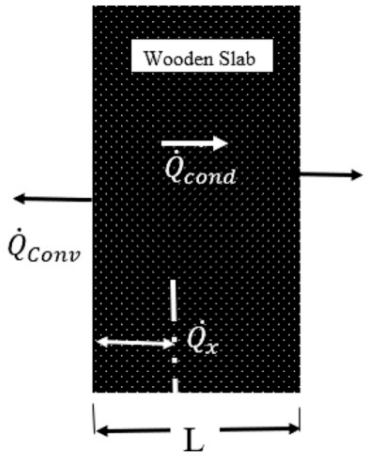


**Fig. 1** Schematic diagram of heat transfer across the wooden slab

to *G*30 and *G*50 are derived by the algorithm. In actual situation, porosity increases with time and temperature. But for the sake of model simplicity, the porosity has been kept constant. For comparison, parameters are assumed to be fixed in modelling problem, so that relative variation can be measured.

According to the conservation of the solid energy (Eq. 1), the algebraic sum of the change of internal energy of solid (*I*), the heat conduction through the fixed bed (*II*), the internal convective heat transfer between fixed bed and the ambience (*III*), and the heat of reaction within the solid (*IV*) is equal to zero:

$$\underbrace{\Delta U}_{I}+\underbrace{\dot{Q}_{conduction}}_{II}+\underbrace{\dot{Q}_{convection}}_{III}-\underbrace{\Delta H_{heatofreaction}}_{IV}=0 \tag{1}$$

Simplification of Eq. (1) in time basis can be expressed as:

$$\frac{\partial\{h_s\rho_s(t)(1-\varepsilon)\}}{\partial t}-\left(k_s(1-\varepsilon)\frac{\partial T}{\partial x}\right)_{x=L}+ \\ +\frac{\overline{h}}{(1-\varepsilon)}(\theta_0)-\frac{\partial\{C_p\rho_s(t)(1-\varepsilon)T\}}{\partial t}=0 \tag{2}$$

where:

$\theta_0 = (T_s - T_g)$

$G=\sqrt{\frac{h_sP}{k_sA}}$

$$\frac{h_s}{k_s}\left(\frac{\partial\{\rho_s(t)(1-\varepsilon)\}}{\partial t}\right)-(1-\varepsilon)\left(G\frac{\sin h\left[G(x-L_c)\right]}{\cos h\left[G(L-L_c)\right]}+\frac{\partial T_g}{\partial x}\right)+ \\ +\frac{\overline{Nu}}{L}\frac{1}{(1-\varepsilon)}\left(\frac{\cos h\left[G(x-L_c)\right]}{\cos h\left[G(L-L_c)\right]}\right)-\frac{1}{\alpha_s}\frac{\partial\{T\}}{\partial t}=0 \tag{3}$$

By integration of Eq. (3) with respect to time (*t*), one gets expression for mass losses during pyrolysis for the combination of *G*30 and *G*50 chips:

$$m_c(t) = 0.001m_c(t_0) - \left[0.000864[L^2(-0.0045\cdot L^2 + 0.267\cdot L) - \right. \\ - L_c^2(-0.0018\,L\cdot L_c + 0.8013L + 0.00135L_c^2 - 0.534L_c)] + \\ + 0.000864\left[G\{(L\cdot L_c - 2 - L_c^2)\,\mathrm{sech}(G(L-L_c)) - \right. \\ \left.\left. - 1{,}000L\cdot\tanh(G(L-l_c))\} + 0.28\{L + (L-2L_c)\cdot\mathrm{sech}(G(L-L_c)) - \right.\right. \\ \left.\left. - 2\tanh(G(L-L_c))\}\right]\right] \tag{4}$$

Similarly, the deduced expressions for mass losses in pyrolysis of hardwood chips *G*30 and *G*50 are given by Eq. (5) and Eq. (6), respectively:

$$m_{G30}(t) = 0.001m_{G30}(t_0) - \left[0.032[L^2(0.3847L - 0.00068L^2) - \right. \\ + L_c^2(0.00205L_c^2 + 1.154L - 0.00273LL_c - 0.7694L_c)] + \\ + 0.032\left[G\{(L\cdot L_c - 2 - L_c^2)\,\mathrm{sech}\,(G(L-L_c)) - 1{,}000L\cdot \right. \\ \left.\left. \cdot\tanh(G(L-l_c))\} + 0.28\{L + (L-2L_c)\cdot\mathrm{sech}(G(L-L_c)) - \right.\right. \\ \left.\left. - 2\cdot\tanh(G(L-L_c))\}\right]\right] \tag{5}$$

$$m_{G50}(t) = 0.001m_{G50}(t_0) - \left[0.00889[L^2(0.2208L - 0.00033L^2) - \right. \\ - L_c^2(0.001L_c^2 - 0.441L_c + 0.662L - 0.00133LL_c)] + \\ + 0.00889\left[G\{(L\cdot L_c - 2 - L_c^2)\,\mathrm{sech}(G(L-L_c)) - 1{,}000L\cdot \right. \\ \left.\left. \cdot\tanh(G(L-l_c))\} + 0.28\{L + (L-2L_c)\cdot\mathrm{sech}(G(L-L_c)) - \right.\right. \\ \left.\left. - 2\cdot\tanh(G(L-L_c))\}\right] \tag{6}$$

where:
$L$ – the equivalent length of the fixed bed (m)
$L_c$ – the corresponding length of the shrinking bed (m)
$G$ – geometric parameter ($m^{-1}$)
$B$ – Biot number
$\rho_s$ – density of solid mass ($kg \cdot m^{-3}$)
$T_g$ – temperature of the volatile gas (°C)
$T_s$ – temperature of the solid mass (°C)
$\varepsilon$ – voidage of bed
$h$ – heat transfer coefficient ( $kW \cdot m^{-2} \cdot K^{-1}$)
$k_s$ – thermal conductivity ($kW \cdot m^{-1} \cdot K^{-1}$)
$Nu$ – Nusselt number
$\theta_0$ – temperature difference between solid and the volatile gas (°C)
$\alpha_s$ – thermal diffusivity of solid ($m^2 \cdot s^{-1}$)
$m$ – mass (g)
$P$ – perimeter of the cross sectional area of a slab (m)
$A$ – cross sectional area of a slab ($m^{-2}$)
$h_s$ – internal energy of the solid mass ($kJ \cdot kg^{-1}$)

The relationship between the rate of change of bulk density activation energy of wood is given by Eq. (7):

$$\frac{d\left(\frac{\rho_{b(t)}}{\rho_{b(t_0)}}\right)}{dt} = -A \cdot \exp\left(-E/RT\right)\left|\rho_{b(t)} - \rho_{b(t_0)}\right| \quad (7)$$

where:
$A_i$ – frequency factor
$E$ – activation energy necessary for thermal decomposition of hardwood

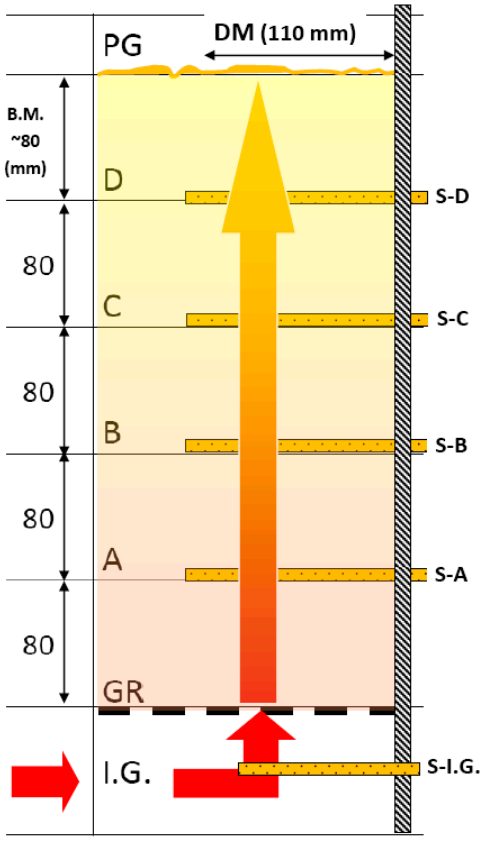


**Fig. 2** Schematic diagram of pyrolysis reactor (S-A, S-B, S-C, S-D, temperature sensors; S-I-G, thermogravimetric sensor; GR, grate material)

## Experimental set-up

The experimental testing rig is situated at the National Agriculture Research and Innovation Centre, Hungary. The different sizes of the hardwood chips (*G*30 and *G*50) (Austrian Standard International (ÖNORM), Austria) are used for the experimental purposes. The physiochemical properties of hardwood are determined using physical and chemical analysers. To measure the system extensive and intensive properties, the thermogravimetric, pressure, and temperature sensors are retrofitted around the periphery of the pyrolysis reactor. The illustrative diagram of reaction is shown in Fig. 2 (Nickel-Chromium/Nickel-Alumel). The weight sensor, which is separated by the insulating cover, is kept under the heating chamber. All the sensors are connected to the computer through a data logger (HBM, Germany). The volumetric rate of inert gas is controlled by a flow meter. The indirect heating element (Herz-filament, Hungary) of 2 kWe is installed inside the reactor to initiate pyrolysis process of biomass. The grid material of heating chamber is made of 0.7 mm stainless steel, while the rock wool of 50 mm thickness is coated around the reactor. The core of the pyrolysis chamber is made of 1.5 mm welded carbon steel. The inner diameter of reactor is 110 mm, the outer diameter is 210 mm. The material used to fabricate the reactor periphery is aluminium. Elemental composition of the raw material is determined by CHN-S analyser (VARIO EL, Italy). The analyser gets heated up to temperature of 2000 °C before the process initialisation. The helium gas is used as a carrier gas inside CHN-S analyser; its function is to carry away the product of combustion to different reduction columns. These tubes are placed in-between the combustion chamber and the signal-processing unit. The gases are separated into their constituents through purge or trap chromatography. After this process, each component is individually detected by a thermal conductivity detector (TCD, Thermo Fisher, USA). The product of combustion is absorbed in sequence; however, nitrogen does pass through the reduction columns. The physiochemical characteristic of hardwood (acacia) is illustrated in Table 1 (dry basis). The kinetic parameters are determined using Eq. (7). The area under the predicted curves is evaluated using the MATLAB (2015a) software.

**Table 1** Physiochemical characteristic of hardwood (dry basis)

| C % | H % | N % | S % | O % | Ash % | HHV* ($MJ \cdot kg^{-1}$) | $\rho_b$ ($kg \cdot m^{-3}$) | $\rho$ ($kg \cdot m^{-3}$) |
|---|---|---|---|---|---|---|---|---|
| 45.84 | 5.62 | 0.18 | 0.06 | 39.91 | 0.58 | 19.02 | 545 | 760 |

* higher heating value; *b* – bulk density

## Results and discussion

An analogous model for hardwood pyrolysis is used to determine the effect of physical properties on decomposition of hardwood chips. Variation of the proposed geometrical parameter *G* on the mass loss curves is illustrated in Fig. 3. The geometrical parameter *G* is a dependant function of the thermal and geometric parameters of a wooden slab. However, the thermal properties are fixed for a particular material, therefore, it does not vary with a given condition. The slab dimensions are subjected to alterations so that the effect of geometry of a pyrolysis bed on the mass loss variation can be examined. It is known through the proposed modelling scheme that the increasing value of *G* shifts the mass-loss curve upwards. It implies that the symmetrical slab allows more char production than that of the asymmetrical one. Moreover, the fractional reduction of the residual mass is relatively high due to asymmetricity. This is due to reason that a symmetrical slab lets the volatiles escape more quickly than the asymmetrical one, the thermal energy accompanying the released gas thus reduces the residence time of volatiles inside the matrix. Finally, it prevents autocatalytic reaction from occurring inside the matrix, hence the large size chip helps to develop the large thermal gradient, and it causes local condensation of volatiles. The similar attribute has also been reported for pyrolysis of a large particle (Dhaundiyal et al., 2020; Bartlett et al., 2019). The thermal gradient is also affected by the slab geometry. The thermal gradient across the wooden slab of the *G*50 chip is higher than that of the wooden slab of *G*30 chip. The value of the Biot number (*B*) varies from 7.49 to 10.32 for different size of hardwood chips (Table 2), which implies that temperature gradient across the slab is non-uniform. It is also established from the experimental results that the non-uniform distribution of temperature across the fixed bed does exist and it affects the mass variation of hardwood chips with respect to time (Fig. 4). Moreover, to determine whether the proposed scheme can be extrapolated, it is necessary to examine the higher thermal regime so that the application of the model can be demarcated.

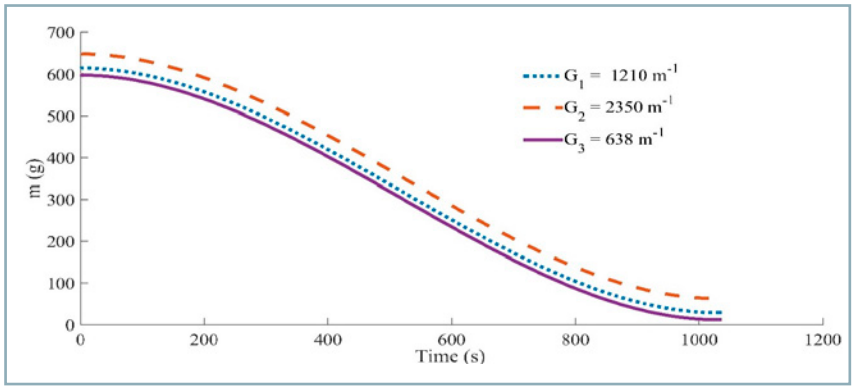


**Fig. 3** Effect of the geometrical parameter '*G*' on the numerical solution of pyrolysis of hardwood chips

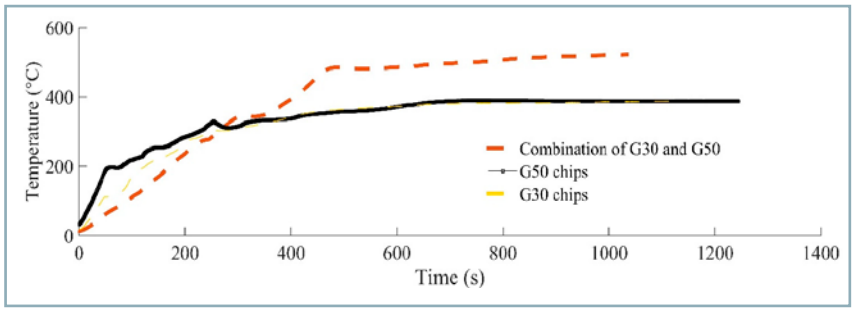


**Fig. 4** Temperature distribution across pyrolysis bed of hardwood

**Table 2** Properties of an equivalent wooden slab for the proposed model

| Hardwood Chips | $R^2$ | $L$ (m) | $G$ ($m^{-1}$) | $B_i$ |
|---|---|---|---|---|
| ***G*30** | 0.99 | $0.0732 \le L \le 0.074$ | $G \le 3590$ | 7.49 |
| ***G*50** | 0.97 | $0.095 \le L \le 0.108$ | $G \le 7161$ | 10.32 |
| **Combination (*G*30 and *G*50)** | 0.98 | $0.085 \le L \le 0.0889$ | $G \le 5348$ | 8.84 |

The effect of equivalent length of slab is illustrated in Fig. 5. The slab length *L*, analogous to the height of the fixed bed of *G*30, *G*50, and combination of *G*30 and *G*50, affects the decomposition of the wooden slab at the beginning of pyrolysis. The increasing length of the wooden slab causes the mass-loss scale to shift upward, which in turn decreases the rate of conversion of wood chips throughout the whole pyrolysis process. The relative change in the residual mass of wood due to variation of the equivalent length is lesser than the relative change in the initial mass of wood. It implies that the shrinkage of the wooden slab has a significant contribution to increase the convective heat transfer resistance across the wooden slab, thus the conversion rate is nearly the same for the varying size of wooden slab. It is noted that the same characteristics have been found for *G*30, *G*50 and the combination of both.

The effect of porosity on numerical solution is depicted in Fig. 6. The porosity is proportional to the volume fraction of the air void and solid mass. It is evident from the predicted solution that the increasing fraction of porosity of air-void makes the mass-loss curve shifted downward at the beginning of pyrolysis. The conversion rate tends to be more uniform as the porosity increases, therefore, it can be inferred that the fluid resistance to the volatile content increases. The resistance is relatively high in the large wooden slab; thus, the size of wooden slab may influence the extent of the secondary pyrolysis reactions, as well as the yield of char through mass transfer. The

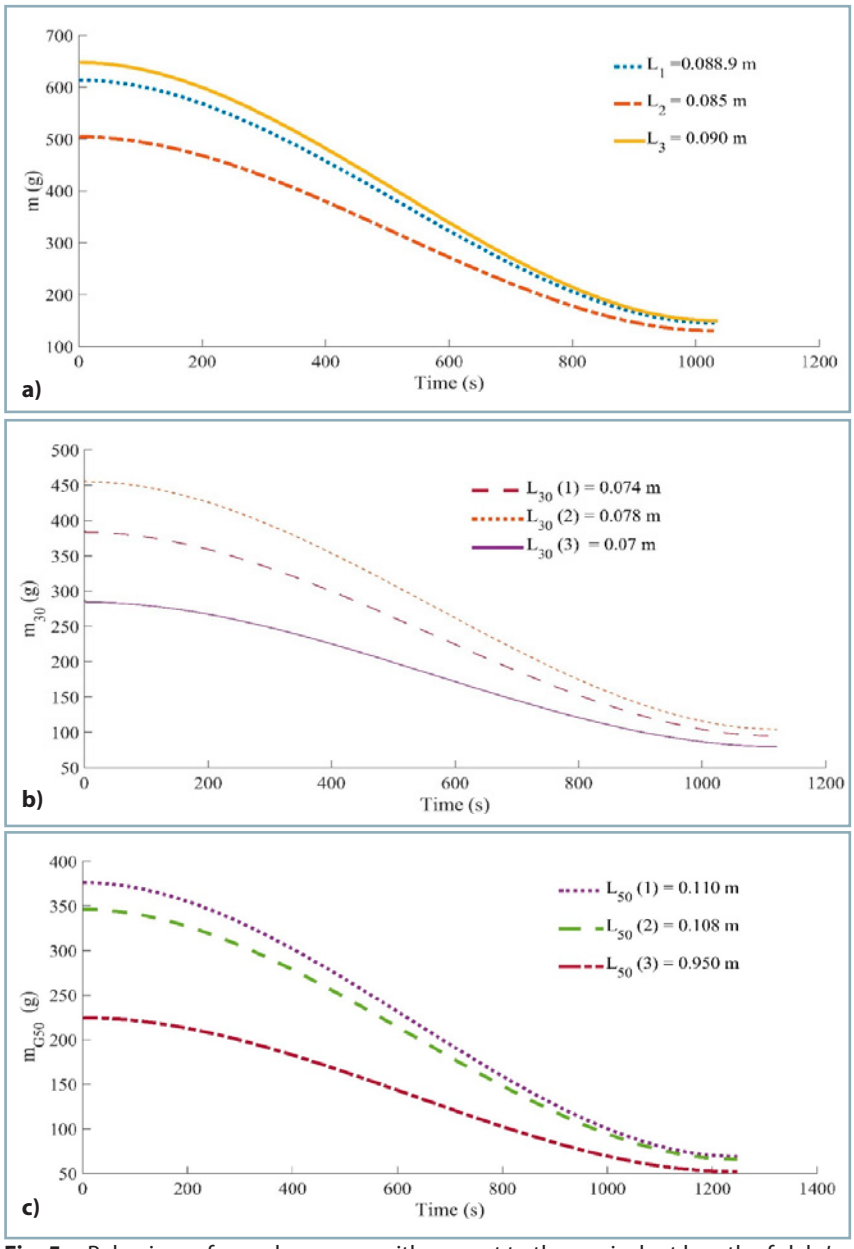


**Fig. 5** Behaviour of mass loss curve with respect to the equivalent length of slab *L*
a – heterogeneous mixture of G30 and G50; b – G30; c – G50 chips

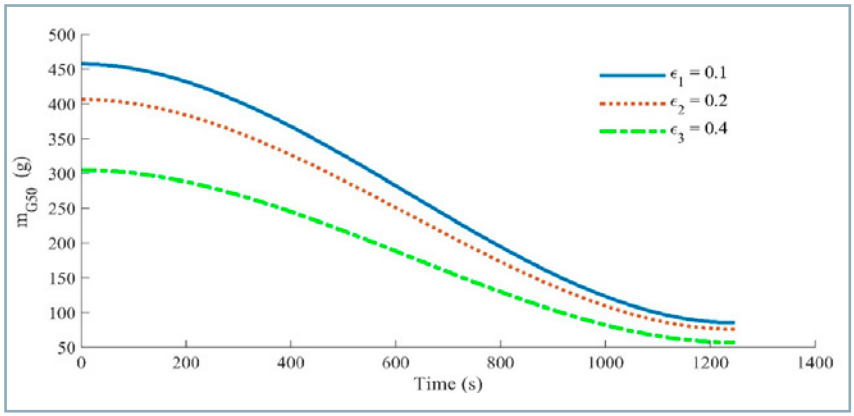


**Fig. 6** Effect of porosity (ε) on the numerical solution of hardwood pyrolysis

direction of heat flow perpendicular to the grain orientation also increases the residence time of pyrolysis gases and supports the autocatalytic reactions (Roberts and Clough, 1963). The experimental plot of mass-loss of hardwood chips is illustrated in Fig. 7. The similar characteristic has been observed in the proposed model. The decomposition curve of hardwood chips, *G*50, has relatively linear attribute at the onset of pyrolysis that shows that thermal gradient across the fixed bed is larger than that of the fixed bed of *G*30 chips. Therefore, for the similar temperature interval, the domain of devolatisation is relatively extended for the large particle.

Comparison of the predicted solution for different wooden slab sizes with the experimental data is demonstrated in Fig. 8. It is clearly visible that the predicted solution provided the good correlation with the experimental curve. The assumption of the fixed bed as a wooden slab with the conversation of mass in hardwood pyrolysis depicts that the residual mass, range of devolatisation, convective resistance, residence time of volatiles in the matrix, and effect on conversion rate are highly influenced by physical fuel characteristics. The predicted solution shows good compliance at the initial stage of pyrolysis and the difference between residual masses of predicted and experimental is marginally low. On the other hand, the proposed models for *G*30 and *G*50 chips are depicted in Fig. 8 (b, c). Here, the numerical solution for *G*50 has shown a slight deviation in the residual mass, whereas the deviation of the residual mass for *G*30 is relatively low. This may be due to either non-uniformity of temperature gradient or the structural effects (surface cracks or longitudinal channelling), which occur due to the sudden drop of pressure inside the slab that leads to alteration of the heating characteristic of biomass.

The kinetic constants evaluated for different chip sizes are shown in Table 3. The estimated value of activation energy is compared with the different species of wood and it is within permissible range of variation (Lim and Chew, 2005). The activation energy for hardwood (acacia) varies from 73.5 to 88.48 kJ·mol$^{-1}$, whereas the frequency factor varies from

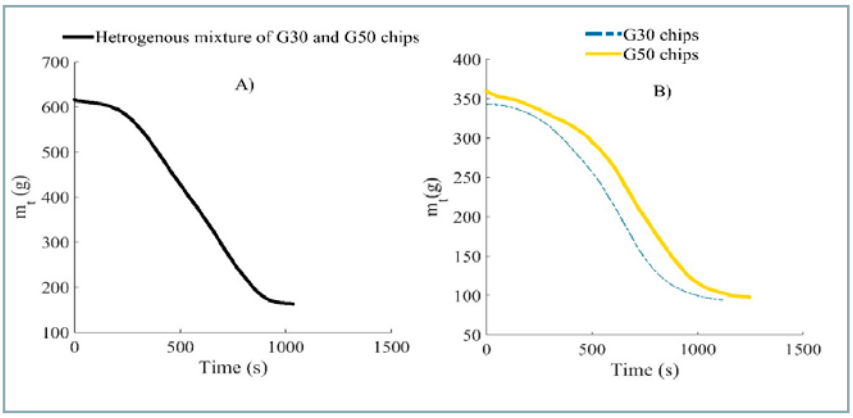


**Fig. 7** Mass loss curves for the wooden chips
A – Heterogeneous mixture of *G*30 and *G*50; B – *G*30 and *G*50 chips

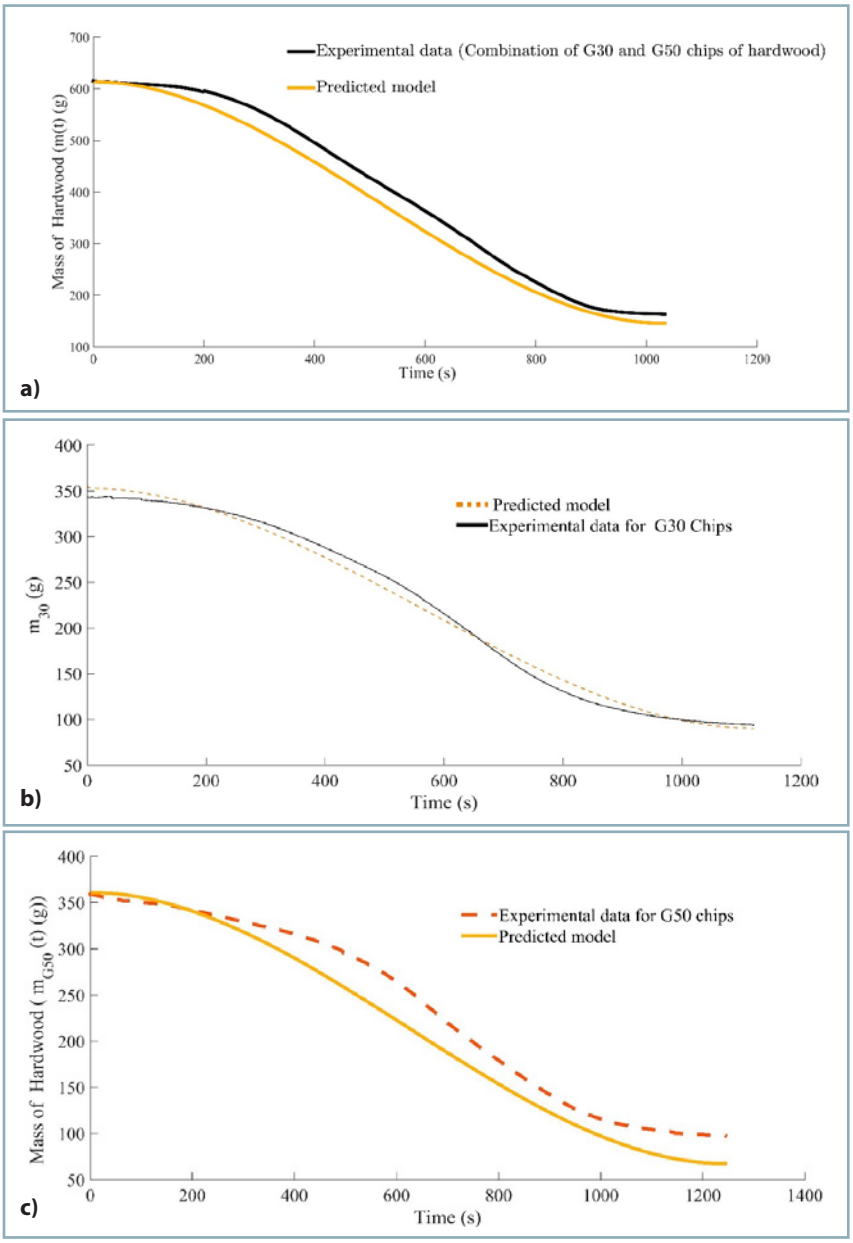


**Fig. 8** Comparison of experimental data with the predicted solution for different combination of hardwood chips
a – heterogeneous mixture of G30 and G50; b – G30; c – G50 chips

$1.02 \times 10^4$ to $1.27 \times 10^4$ $min^{-1}$. The detailed information is given in Table 3. It is found that the size variation of wooden slab also affects the kinetic study of pyrolysis, however, the range of temperature used for experimental purpose has a major role in determining the kinetic parameters. The difference between the kinetic parameters of wooden slabs of *G*30 and *G*50 chips is marginally narrow. The bulk density of bed and the porosity play a significant role in determining the apparent activation energy. It implies that the kinetic constants, as well as the heat of reaction, before and after the breaking point of wood, differ from each other (Tinney, 2007). It is noted that the Monte Carlo is implemented to measure the kinetic parameters (Dhaundiyal et al., 2019b; Dhaundiyal and Toth, 2020).

## Conclusion

Pyrolysis modelling of hardwood (acacia) pivoted around the analogous model, which is equivalent to the fixed bed of pyrolysis reactor. The effect of physical properties on thermogravimetry of the wooden chips is investigated through a proposed model. It is found that the equivalent length of wooden slab for *G*30 should vary from 73 to 74 mm, whereas it is relatively large for *G*50 and the combination of both of them. The wooden slab of 95–108 mm is suitable to simulate the result for *G*50 chips. On the other hand, it is 85–89.5 mm for combination of both. The results simulated by proposed model provide a good correlation with experimental results (Table 2). Moreover, the kinetic constants for hardwood is found to vary from 73.5 to 88.48 $kJ \cdot mol^{-1}$, which also lie within a permissible range of variation of activation energy for different species of wood (Müller-Hagedorn et al., 2003). The Biot number for the wooden slab varies from 7.49 to 10.49, which implies that the temperature gradient is non-uniform across the wooden slab. Moreover, with respect to time, the variation of bulk density of bed also influences the thermo-kinetics of hardwood. It is concluded that kinetic constants, before and after the wood breakage point, may differ from each other. The limiting factor of this analysis focuses on the resistance to the flow of fluid and

**Table 3** Kinetic constants for hardwood (acacia)

| Area under curves | Chip Size | *E* | $A_i$ | Activation energy (kJ·mol$^{-1}$)* |
|---|---|---|---|---|
| **148330 sq. unit** | *G*30 | 73.5 kJ·mol$^{-1}$ | $1.20 \times 10^4$ (min$^{-1}$) | 71 kJ·mol$^{-1}$ (beech saw dust) |
| **190940 sq. unit** | *G*50 | 74 kJ·mol$^{-1}$ | $1.06 \times 10^4$ (min$^{-1}$) | 125.4 kJ·mol$^{-1}$ (softwood) |
| **256610 sq. unit** | combination | 88.48 kJ·mol$^{-1}$ | $1.27 \times 10^4$ (min$^{-1}$) | 85.69 kJ·mol$^{-1}$ (hardwood), 55 (pine) |

Source*: Lim and Chew, 2005; Blasi, 1993; Dhaundiyal and Singh 2019

the surface of the wooden slab. The convection resistance must be low and conduction resistance should be high, and it is clearly depicted by the Biot number. The decrease in the convection resistance must be higher than the increase in the conduction resistance for better correlation between the experimental and the mathematical model.

## References


BARTLETT, A. I. – HADDEN, R. M. – BISBY, L. A. 2019. A review of factors affecting the burning behaviour of wood for application to tall timber construction. In Fire Technology, vol. 55, no. 1, pp. 1–49.

BLASI, C. D. 1993. Modeling and simulation of combustion processes of charring and non-charring solid fuels. In Progress in Energy and Combustion Science, pp. 71–104.

CAI, J. – LIU, R. 2008. New distributed activation energy model: Numerical solution and application to pyrolysis kinetics of some types of biomass. In Bioresource Technology, vol. 99, no. 8, pp. 2795–2799.

DHAUNDIYAL, A. – ABDULRAHMAN, T. M. – LASZLO, T. 2019a. Thermo-kinetics of forest waste using model-free methods. In Universitas Scientiarum, vol. 24, no. 1, pp. 1–31.

DHAUNDIYAL, A. – SINGH, S. B. – HANON, M. M. 2018b. Study of distributed activation energy model using bivariate distribution function, f (E1, E2). In Thermal Science and Engineering Progress. vol. 5, pp. 388–404.

DHAUNDIYAL, A. – TOTH, L. 2020. Modeling of hardwood pyrolysis using the convex combination of the mass conversion points. In Journal of Energy Resources Technology, Transactions of the ASME, vol. 142, no. 6, pp. 1–10.

DHAUNDIYAL, A. – SINGH, S. B. – HANON, M. M. – RAWAT, R. 2018c. Determination of kinetic parameters for the thermal decomposition of *Parthenium hysterophorus*. In Environmental and Climate Technologies, vol. 22, no. 1, pp. 5–21.

DHAUNDIYAL, A. – SINGH, S. B. – ATSU, D. – DHAUNDIYAL, R. 2019b. Application of Monte Carlo simulation for energy modelling. In ACS Omega, vol. 4, no. 3, pp. 4984–4990.

DHAUNDIYAL, A. – TOTH, L. – BACSKAI, I. – ATSU, D. 2020. Analysis of pyrolysis reactor for hardwood (acacia) chips. In Renewable Energy, vol. 147, pp. 1979–1989.

DHAUNDIYAL, A. – SINGH, S. B. – HANON, M. M. – SHREMPF. N. 2018a. Clayton copula as an alternative perspective of multi-reaction model. In Environmental and Climate Technologies, vol. 22, no. 1, pp. 83–106.

DHAUNDIYAL, A. – SINGH, S. B. 2019. Stochastic analysis of multi-reaction model for non-linear thermal history. In Acta Technologica Agriculturae, vol. 22, no. 3, pp. 92–98.

FOGLER, H. S. 2004. Chemical reaction engineering. In the Engineering Handbook, second edition, pp. 79-1-79-18.

KUNG, H. C. 1972. A mathematical model of wood pyrolysis. In Combustion and Flame, vol. 18, no. 2, pp. 185–195.

LIM, S. M. – CHEW, M. Y. L. 2005. Compensation effects in the non-isothermal pyrolysis of wood. In Fire Safety Science, vol. 8, pp. 1109–1120.

MAA, P. S. – BAILIE, R. C. 1973. Influence of particle sizes and environmental conditions on high temperature pyrolysis of cellulosic material (theoretical). In Combustion Science and Technology, vol. 7, pp. 257–269.

MANI, T. – MURUGAN, P. – MAHINPEY, N. 2009. Determination of distributed activation energy model kinetic parameters using simulated annealing optimization method for nonisothermal pyrolysis of lignin. In Industrial and Engineering Chemistry Research, vol. 48, no. 3, pp. 1464–1467.

MÜLLER-HAGEDORN, M. – BOCKHORN, H. – KREBS, L. – MULLER, U. 2003. A comparative kinetic study on the pyrolysis of three different wood species. In Journal of Analytical and Applied Pyrolysis, pp. 231–249.

POLESEK-KARCZEWSKA, S. – KARDAŚ, D. 2015. Prediction of thermal behaviour of pyrolyzed wet biomass by means of model with inner wood structure. In Journal of Thermal Science, vol. 24, no. 1, pp. 82–89.

ROBERTS, A. F. – CLOUGH, G. 1963. Thermal decomposition of wood in an inert atmosphere. In Symposium (International) on Combustion, vol. 9, no. 1, pp. 158–166.

SADHUKHAN, A. K. – GUPTA, P. – SAHA, R. K. 2009. Modelling of pyrolysis of large wood particles. In Bioresource Technology, vol. 100, no. 12, pp. 3134–3139.

TINNEY, E. R. 2007. The combustion of wooden dowels in heated air. In Symposium (International) on Combustion, vol. 10, no.1, pp. 925–930.

WITKOWSKI, A. – STEC, A. – HULL, T. R. 2016. Thermal decomposition of polymeric materials. In SFPE Handbook of Fire Protection Engineering, fifth edition, pp. 167–254.

sciendo

DOI: 10.2478/ata-2020-0029



Acta Technologica Agriculturae 4
Nitra, Slovaca Universitas Agriculturae Nitriae, 2020, pp. 183–189

# THE COOLING MEDIA INFLUENCE ON SELECTED MECHANICAL PROPERTIES OF STEEL

Radim ŠMAK*, Jiří VOTAVA, Adam POLCAR

Mendel University in Brno, Czech Republic

The aim of experiment was to analyse the structural transformations and changes in mechanical properties of K720 steel during heat treatment (quenching). Three types of cooling medium were selected. The heating parameters and subsequent delays at the recrystallisation temperature were the same for all samples and were observed in a laboratory furnace. Water with the highest cooling capacity was selected as the benchmark cooling medium. Subsequently, the hardening oil TK – 46 was used. Sunflower oil was selected as the last quenching medium, which can be considered an ecological replacement of quenching oil with possibility of biological disposal. The microstructure and microhardness of individual samples were subjected to a metallographic evaluation and evaluated according to ČSN EN ISO 6507, respectively. The impact toughness analysis was performed according to the ČSN EN ISO 148-1 and a three-point bending test was performed according to ČSN EN ISO 7438. This test specifies a method for determining the ability of metallic materials to undergo plastic deformation in bending. The bend test includes subjection of round, square, rectangular or polygonal cross-section to plastic deformation by bending, without changing the direction of loading, until the specified angle of bend is reached.

**Keywords:** hardening; structure; microstructure; carbon steel; K720 steel

Steel and iron alloys are the most important contemporary construction materials; they are used for construction purposes in a form of bars, sheets, profiles, etc. The properties of steels are derived according to the content of alloys and heat treatment. The most basic compositions are made of iron and carbon. Alloys are carefully selected in order to adjust the mechanical properties of final product, i.e. toughness, hardness, abrasion resistance, hardenability, etc. (Napoli et al., 2018; Votava et al., 2016).

In addition to the chemical composition, the mechanical properties can be effectively altered by a suitably selected heat treatment. During heat treatment, the crystalline structure of steel changes, what leads to significant changes in its properties (Galindo-Nava and Rivera-Díaz-del-Castillo, 2017). It is also possible to change the mechanical properties of materials by addition of an abrasion-resistant layer to the surface (Ťavodová et al., 2018; Pauliček et al., 2013). Based on the supplied alloying elements, the internal structure may also change. Appropriately selected heat treatment can result in high hardness or toughness. The carbon content in steel significantly changes the sensitivity to the heat treatment. However, in order to achieve high hardness, the carbon content of tool steels ranges from approx. 0.5 to 1.5% C (Haiko et al., 2019). Suitable cooling environment is another aspect with a major impact on resulting mechanical steel properties.

For the research purposes, several types of cooling media were used for hardening the samples of tooled carbon supernatant steel. Subsequently, a series of tests was conducted on these samples: measurement of the hardness, impact toughness and bending tests. Finally, a metallographic analysis of samples was performed, and the microhardness was determined.

## Material and methods

For the experiment purposes, test samples were prepared according to Fig. 1. The samples were heated in an MP 05 – 1.1 laboratory furnace with air access and without any protection against decarburization. Prior to heating of samples, the furnace was heated to 810 °C. The continuous rise to this temperature was set for 60 min and was subsequently held at desired temperature for 30 min, since the heating time must ensure austenitization in the entire product cross section. The main parameters include austenitization temperature and delay at this temperature (Gomes et al., 2019) The material sheet calls for a delay of at least 15 minutes at austenitization temperature. Four samples clamped to one quencher were quenched in each cooling bath. Çakir et al. (2011) list three stages of contact between the cooling medium and hardened object surface (vapour phase, nucleate boiling and convective stage). In the first phase, the heat dissipation is low and increases with subsequent phases (Fernandes et al., 2007). After complete immersion below the cooling medium surface, the samples were moved with a bath volume to eliminate the formation of gaseous envelope around the samples (Çakir et al., 2011).

**Contact address:** Radim Šmak, Mendel University in Brno, Faculty of AgriSciences, Department of Technology and Automobile Transport, Zemědělská 1, 613 00 Brno, Czech Republic; e-mail: xsmak@node.mendelu.cz

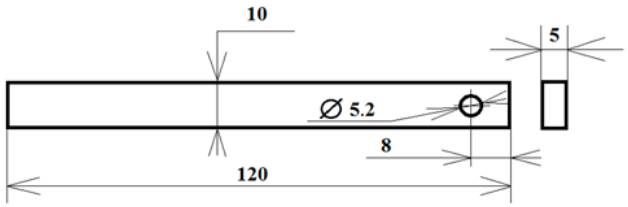


**Fig. 1** Sample dimensions

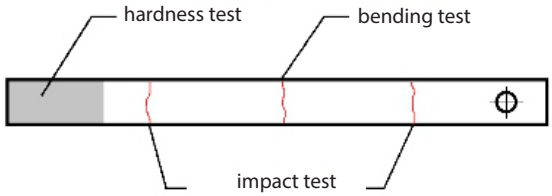


**Fig. 2** Testing areas

**Table 1** Chemical composition of K720 steel

| K 720 | C | Si | Mn | Cr | V |
|---|---|---|---|---|---|
| | 0.90 | 0.20 | 2.00 | 0.40 | 0.10 |

In order to make the maximum use out of the individual samples and in order to achieve the highest possible accuracy of measurement results, 5 measurements were conducted on each sample (Fig. 2). Firstly, the hardness tests were performed (according to the ČSN EN ISO 6508); subsequently, the three-point bending break tests were conducted using a single-axis tensile testing machine, and finally, impact tests were performed using a Charpy hammer. According to ČSN EN ISO 148-1, this test consists of breaking a notched test piece with a single blow from swinging pendulum under specified conditions. The notch of test piece has a specified geometry and is placed in between two supports – opposite to the location, which is impacted in a test. The energy absorbed in the impact test, the lateral expansion, and the shear fracture appearance are normally determined.

The microhardness measurement was performed on a set of 3 samples from each cooling bath using a Hannemann microhardness tester according to ČSN EN ISO 6507-1, which is a part of the Neophot 21 metallographic microscope. A diamond pyramid with an apex angle of 136 ° and a force of 0.9806 N was pressed into the material. The microhardness HV is subsequently read according to the length of the diagonals. This method is suitable for heat-treated material and coatings with a thickness over 10 µm (Votava et al., 2020).

### Heat treatment parameters

Production company provided free downloadable materials for the heat treatment and subsequent use of steel K 720; its chemical composition is given in Table 1. Its quenching temperature ranges from 790 to 820 °C; delay at the quenching temperature ranges from 15 to 30 min; tempering temperature is 250 °C; and delay at the tempering temperature is 120 min. Such a low tempering temperature was selected in order to achieve the required hardness of future product.

## Results and discussion

### Experiment evaluation

The first aspect taken into account was the surface of samples. The samples were heated with access to oxygen, resulting in coverage of their surface with a layer of oxides with different cohesiveness during heating (Brito et al., 2019). Fig. 3 shows representatives from each bath: the purest samples are produced by the water bath. Furthermore, hardening oil also showed very good results in terms of the surface cleanliness – scales are still visible on the samples, but the surface is completely clean in certain places. In addition to this, the hardening process was not accompanied by flames and there was little smoke during the process. The samples hardened in vegetable oil showed a continuous layer of partially removed scale and thermally degraded oil on their surface. The process was accompanied by occasional formation of flames and considerable smoke. There was a lot of scale released in the vegetable oil used.


**Fig. 3** Surfaces of the hardened samples

**a) WATER sample no. 3, bath temperature: 23.7 °C**

The samples hardened in water showed an average hardness of 62.6 HRC after quenching, the highest value shown from among the baths used. The average hardness dropped to 58.9 HRC by tempering. A similar loss of hardness caused by tempering can be observed in steel DIN 1.3359, which is very similar to K720 steel in terms of carbon content (Amini et al., 2019). After breaking the samples by three-point bending test, all specimens showed a brittle fracture (Fig. 4). The fracture consists of the main fracture surface and there is an additional fracture surface after the fragment separation in the upper part. The fracture surface is uneven, pitted with hints of a shell-like fracture. The highest measured force value for the water bath was 3,179.5 N. The average breaking force of the 5 × 10 mm samples was approx. 3,002 N, which is less by approx. 600 N than breaking force necessary for samples quenched in hardening oil. The three-point

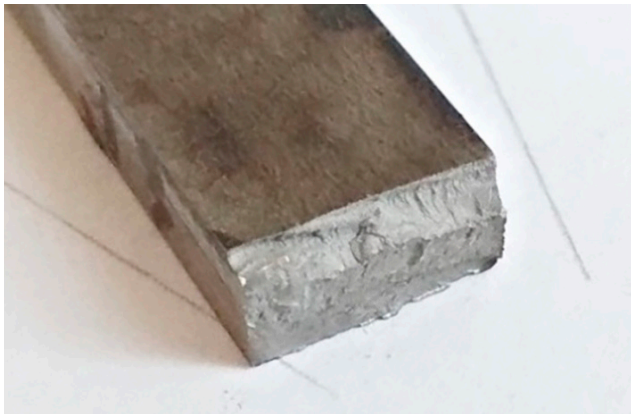

**Fig. 4** Fracture surface appearance – water (impact test)

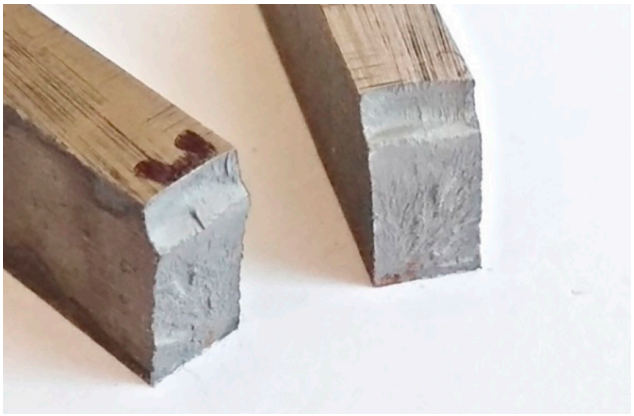

**Fig. 5** Fracture surface appearance – water (bending test)

bending test procedures are almost linear for all samples with no apparent yield strength differences (Fig. 16). The influence of the neighbouring samples on the measured values is not obvious. The fracture surface created after the impact work test is shown in Fig. 5. The fracture consists of the main fracture surface and surface after the fragment separation. There is a well-drawn fan-shaped drawing on the fracture surface. The average value of impact toughness was 9.43 J for the samples hardened in the water, which is the smallest value shown by all the cooling environments. The microstructure and pitting after the microhardness measurement after hardening are shown in Figs. 6 and 7.

**b) HARDENING OIL sample no. 1, bath temperature: 23.8 °C**

The samples quenched in hardening oil were expected to show the best results and were used for comparison with other cooling media. The average hardness after quenching reached value of 62.08 HRC. By tempering, the resulting hardness decreased to an average of 57.75 HRC. The breaking force average value of samples was 3,685.25 N, which was more by approx. 680 N than breaking force necessary for samples hardened in water bath. All of these samples showed a brittle fracture. Selected representative sample is shown in Fig. 8. The fracture surface is conch-shaped and is smoother in contrast to samples hardened in water. The surface of samples is very good – with almost clean surface in certain places. The hardening oil has an

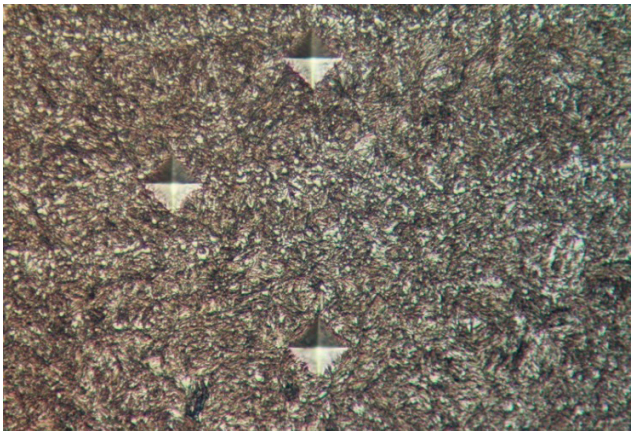

**Fig. 6** Microhardness test of K720 steel – water-hardened

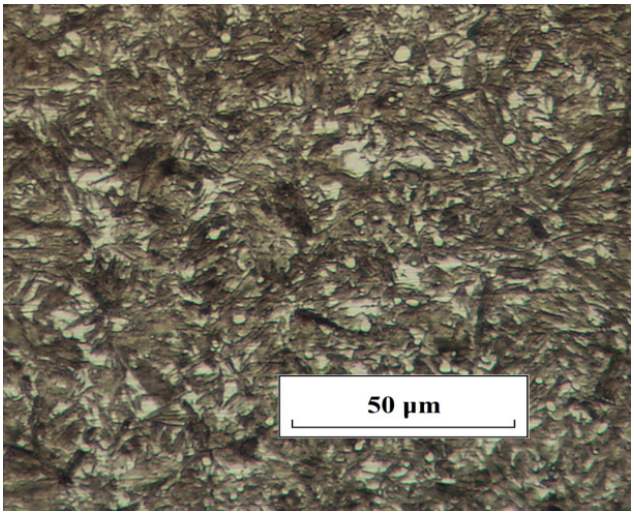


**Fig. 7** Microstructure of K720 steel – water-hardened

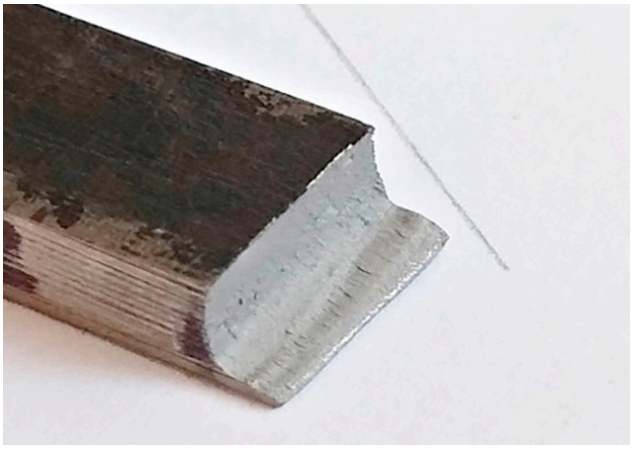

**Fig. 8** Fracture surface appearance – hardening oil (bending test)

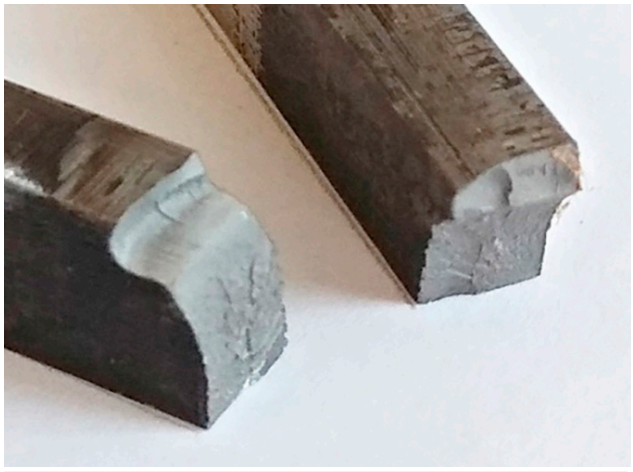

**Fig. 9** Fracture surface appearance – hardening oil (impact test)

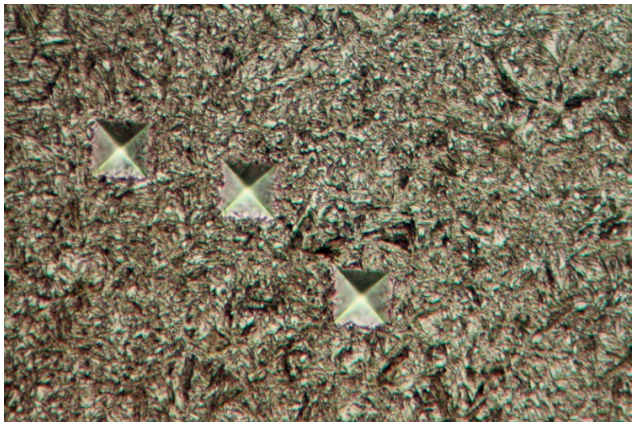

**Fig. 10** Microhardness test of K720 steel – cooled in hardening oil

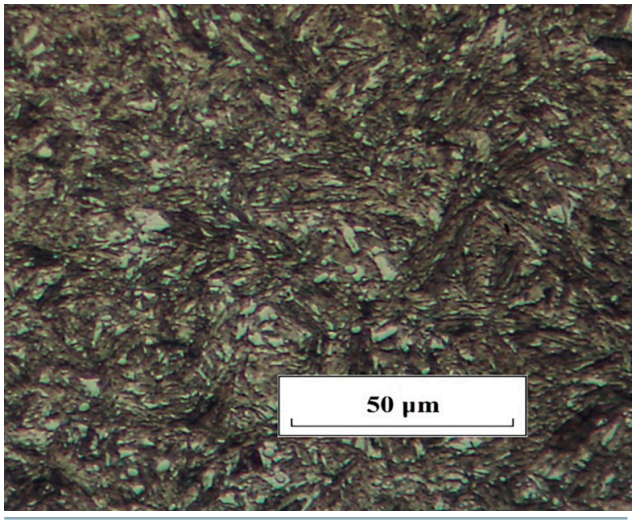


**Fig. 11** Microstructure of K720 steel – cooled in hardening oil

excellent temperature resistance, therefore, there was almost no residual degraded oil visible on the samples. Fig. 9 shows the fracture surface after the Charpy hammer impact test; it consists of the main fracture surface and the surface after fragment separation. A fan-shaped drawing is clearly visible on the main surface area. The average value of impact toughness of samples quenched in hardening oil was 17.77 J, which was almost twice the value shown by samples quenched in water, as well as the highest value from among all cooling environments. The microstructure and pitting after measuring the microhardness after quenching in hardening oil are shown in Figs. 10 and 11.

**c) SUNFLOWER OIL sample no. 2, bath temperature: 23.8 °C**

The samples quenched in sunflower oil showed an average hardness of 58.25 HRC; subsequent tempering reduced the hardness to an average of 55.16 HRC. After a subsequent three-point bending test, it was observed that the breaking force necessary for successful execution of the test was 2,843.02 N in average. The graphs of individual tests are shown in Fig. 16. All samples showed a brittle fracture. The fracture surface appearance of samples quenched in sunflower oil was less shell-like and generally more direct in contrast to samples cooled in hardening oil. The fracture surface showed a slight grain size (Fig. 12). The average impact toughness value was 16.54 J; higher values were achieved only by samples quenched in hardening oil.

**Fig. 12** Fracture surface appearance – vegetable oil (impact test)

**Fig. 13** Fracture surface appearance – vegetable oil (bending test)

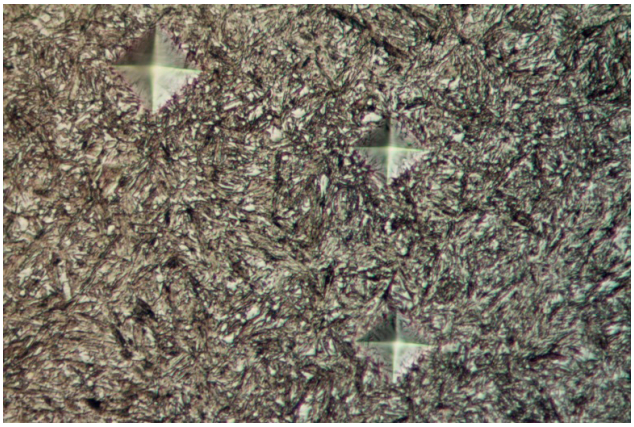

**Fig. 14** Microhardness test of K720 steel – cooled in vegetable oil

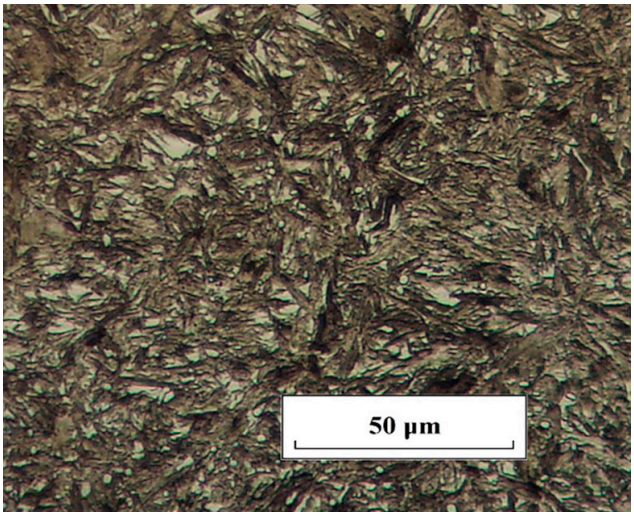


**Fig. 15** Microstructure of K720 steel – cooled in vegetable oil

The fracture surface shape is shown in Fig. 13. All samples showed a brittle fracture. The fracture surface is almost perpendicular to the sample axis and shows a hint of a fan-shaped pattern on its surface. Samples quenched in vegetable oil were covered with a layer of unseparated scale and a layer of degraded oil, which could cause significantly lower hardness in comparison to the samples quenched in other cooling media. The microstructure and pitting after measuring the microhardness after hardening in olive oil are shown in Figs. 14 and 15.

Resulting values of the mechanical properties recorded in individual tests are given in Table 2. In terms of hardness, the water bath appears to be the most suitable cooling environment. In this cooling medium, the highest average hardness – 62.58 HRC – was achieved. Similar values were observed in samples quenched in hardening oil – 62.08 HRC. Brito et al. (2019) conducted an experimental comparison of different vegetable oils and mineral hardening oil. Their results showed that vegetable oil (sunflower oil) reduces the internal stress of samples compared to mineral hardening oil thanks to its cooling properties. This fact was also reflected, since there was recorded a significantly lower hardness – the projectable hardness after quenching was 58.25 HRC. However, a significant advantage of vegetable oil lies in its easy and ecological production, as well as possibility of ecological disposal. Moreover, research realized by Prathviraj et al. (2020) showed that sunflower oil can be used in form of both new or degraded after filtration and chemical purifying. Prathviraj et al. (2020) compared the cooling rates of both types and proved that both are suitable for heat treatment of high carbon steel.

Subsequent tempering was adapted for the purposes of production of cutting tools made of heat-treated steel with high edge retention usable in agricultural production.

The other mechanical properties considered were: deformation; force required to break the samples; and impact toughness. In terms of strength, the best results were shown by the samples quenched in the hardening oil and the lowest in the vegetable oil. The highest values of impact toughness were achieved in the samples cooled in hardening oil; the lowest values were achieved in samples cooled in water bath.

From the overall point of view, the hardness was considered to be a measure indicating the resistance to blunting of cutting part. Furthermore, strength and toughness are indicators of tool cutting part's resistance to damage.

The quenched steel structure shows presence of residual austenite. Due to the insufficient cooling rate in vegetable

**Table 2** Mechanical properties of hardened samples

| Cooling environment | | Hardness after quenching (HRC) | Hardness after tempering (HRC) | Force (N) | Impact toughness (J) |
|---|---|---|---|---|---|
| **Water** | average | 62.58 | 58.91 | 3,002.62 | 9.43 |
| | variance | 0.57 | 0.40 | 30,079.84 | 0.70 |
| | standard deviation | 0.79 | 0.66 | 173.44 | 0.89 |
| **Hardening oil** | average | 62.08 | 57.75 | 3,685.25 | 17.77 |
| | variance | 0.40 | 0.35 | 16,370.94 | 1.06 |
| | standard deviation | 0.66 | 0.62 | 127.95 | 1.10 |
| **Vegetable oil** | average | 58.25 | 55.16 | 2,843.02 | 16.54 |
| | variance | 1.02 | 0.63 | 14,639.04 | 0.34 |
| | standard deviation | 1.05 | 0.83 | 120.90 | 0.62 |

**Table 3** Microhardness values of samples

| Tested materials | Microhardness values $HV_{10}$ | | | | | | | |
|---|---|---|---|---|---|---|---|---|
| | 1 | 2 | 3 | 4 | 5 | average $HV_{10}$ | dir. deviation $HV_{10}$ | var. coefficient (%) |
| **Sample 1** | 644 | 613 | 658 | 658 | 672 | 649 | 20.1 | 3.1 |
| **Sample 2** | 548 | 508 | 570 | 573 | 561 | 552 | 23.7 | 4.3 |
| **Sample 3** | 865 | 844 | 850 | 824 | 833 | 843.2 | 14.1 | 1.7 |

oil bath, there is a higher proportion of residual austenite in hardened steel. Due to the rate of transformation and its non-diffusive character, the samples hardened in water bath have the smallest proportion of residual austenite. Measured values of the microhardness fully correspond with the rest of measured mechanical properties. The measured values are shown in Table 3.

Fig. 16 shows course of the bending force curves for all cooling environments. The curves are intersected by linear regression with $R^2$.

## Deformation of samples

Martensite is a common end product of enormous industrial importance for the most heat-treated commercial low-carbon and medium-carbon steels, and is inevitably accompanied by deformation (Sun et al., 2020). It can be exacerbated by certain significant factors, including chemical composition; material purity; and heat treatment factors (e.g. uneven cooling, unsuitable cooling media, etc.). Significant importance of deformation due to martensitic structure lies in the application of carbide welds for abrasively stressed components. Due to internal stress, the entire weld may break (Votava and Kumbár, 2014). The samples used in this work showed deformation 1 mm at maximum from Fig. 17. Frequently, their deformation was almost negligible. The samples quenched in vegetable oil showed the smallest deformation, the largest deformation occurred in samples hardened in water.

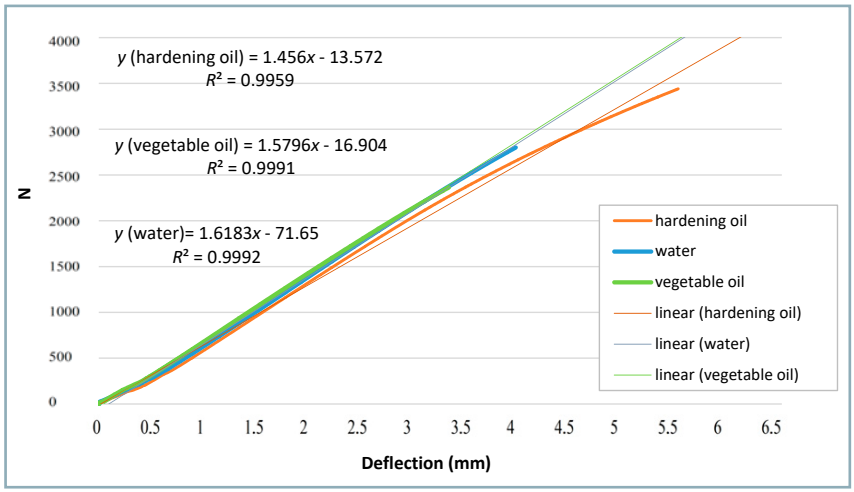


**Fig. 16** Bending test results of hardened samples

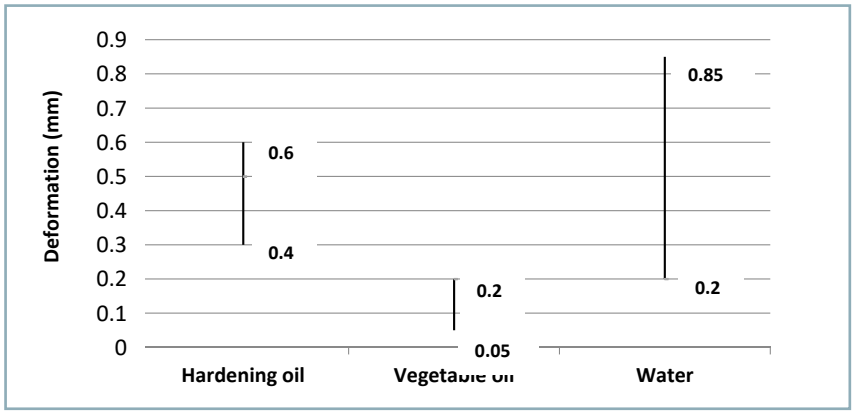


**Fig. 17** Sample deformation statistics

## Conclusion

The work presented deals with the heat treatment of tool steel K 720, namely hardening and tempering. The aim was to determine the influence of individual cooling media (hardening oil, sunflower oil and water) on mechanical properties of this steel. Three types of tests were conducted in order to characterise the loading of machine parts under conditions of agricultural production. The samples were subjected to hardness tests, Charpy impact toughness test and three-point bending test. All tests among individual cooling media were of a comparative nature. Measurement results showed that the most suitable cooling medium for the K 720 steel is the hardening oil TK – 46, since it provided the best results in terms of strength and toughness. The least beneficial results were showed by samples quenched in sunflower oil – these samples showed low hardness and strength in comparison to samples hardened in other types of cooling media. The highest hardness was achieved in water-hardened samples at the expense of the toughness and strength.

Considering all three cooling media used, water clearly provides the most environmentally friendly cooling bath, since it does not require any industrial disposal and can be disposed of safely after its utilization. The situation is very similar for vegetable oil – its production is not difficult and it also

can be easily disposed of in an ecological manner. Since several parameters of tested samples quenched in vegetable oil were similar to properties shown by samples cooled in hardening oil, this cooling medium can be used in specific cases. Although the hardening oil represents the most durable cooling media observed, its ecological disposal is the most difficult.

**Acknowledgment**

This contribution was created with the contribution of the project ZETOR (EG15_019/0004799 – ZETOR TRACTORS a.s.) – Optimal aggregation of machines with a tractor.

## References

AMINI, K. S. – DAYAGHI, S. M. – YAZDANIAN, M. – SEIYED, B. T. – GHARAVI, F. 2019. The effect of tempering temperature on microstructure and the mechanical properties of forged steel containing chrome, manganese and molybdenum. In Mechanics, vol. 24, no. 6, pp. 112–118.

ÇAKIR, M. – ÖZSOY, A. – BRAGA, B. M. – LIU, N. – PENG, Y. – ZHAO, X. – REN, R. – ZHANG, H. 2011. Investigation of the correlation between thermal properties and hardenability of Jominy bars quenched with air–water mixture for AISI 1050 steel: A model describing TRIP and TWIP effects. In Journal of Materials Research and Technology, vol. 32, no. 5, pp. 3099–3105.

BRITO, P. – RAMOS, P. A. – RESENDE, L. P. – DE FARIA, D. A. – RIBAS, O. K. – LIIMATAINEN, T. – KÖMI, J. – ZHANG, H. 2019. Experimental investigation of cooling behavior and residual stresses for quenching with vegetable oils at different bath temperatures: A model describing TRIP and TWIP effects. In Journal of Cleaner Production, vol. 216, no. 20, pp. 230–238

ČSN EN ISO 6508. 2015. Metalic materilals – Rockwell hardness test. Praha: Český normalizační institut.

ČSN EN ISO 7438. 2005. Metallic materials – Bend test. Praha: Český normalizační institut.

ČSN EN ISO 148-1. 2017. Metallic materials – Charpy pendulum impact test. Praha: Český normalizační institut.

ČSN EN ISO 6507. 2018. Metallic materials – Vickers hardness test. Praha: Český normalizační institut

FERNANDES, P. K. – PRABHU, N. – BRAGA, B. M. – LIU, N. – PENG, Y. – ZHAO, X. –REN, R – ZHANG, H. 2007. Effect of section size and agitation on heat transfer during quenching of AISI 1040 steel: A model describing TRIP and TWIP effects. In Journal of Materials Processing Technology, vol. 183, no. 1, pp. 1–5.

GALINDO-NAVA, E. I. – RIVERA-DÍAZ-DEL-CASTILLO, P. E. J. 2017. Understanding martensite and twin formation in austenitic steels: A model describing TRIP and TWIP effects. In Acta Materialia, vol. 128, no. 15, pp. 120–134.

GOMES, D. F. – TAVARES, R. P. – BRAGA, B. M. – LIU, N. – PENG, Y. – ZHAO, X. –REN, R. – ZHANG, H. 2019. Mathematical model for the temperature profiles of steel pipes quenched by water cooling rings: A model describing TRIP and TWIP effects. In Journal of Materials Research and Technology, vol. 8, no. 1, pp. 1197–1202.

HAIKO, O. – KAIJALAINEN, A. – PALLASPURO, S. – HANNULA, J. – PORTER, D. – LIIMATAINEN, T. – KÖMI, J. – ZHANG, H. 2019. The effect of tempering on the microstructure and mechanical properties of a novel 0.4C press-hardening steel: A model describing TRIP and TWIP effects. In Applied Sciences, vol. 9, no. 20, pp. 1–5.

NAPOLI, G. – FABRIZI, G. – RUFINI, R. – MENGARONI, S. – DI SCHINO, A. 2018. Effect of quenching and tempering process on a medium C steel with low chromium and molybdenum addition for forged components. In Acta Metallurgica Slovaca, vol. 24, no. 6, pp.112–118.

PAULIČEK, T. – KOTUS, M. – DAŇKO, M – ŽÚBOR, P. 2013. Resistance of hard-facing deposit created by laser surfacing technology. In Advanced Materials Research, vol. 801, special iss., pp. 117–122.

PRATHVIRAJ, M. P. – AUGUSTINE, S. – NARAYAN, P. 2020. Reprocessed waste sunflower cooking oil as quenchant for heat treatment. In Journal of Cleaner Production, vol. 269, article no. 122276.

SUN, H. – WANG, Y. – WANG, Z. – LIU, N. – PENG, Y. – ZHAO, X. – REN, R. – ZHANG, H. 2020. Twinned substructure in lath martensite of water quenched Fe-0.2 %C and Fe-0.8 %C steels. In Journal of Materials Science and Technology, vol. 49, no. 6, pp. 126–132.

ŤAVODOVÁ, M. – KALINCOVÁ, D. – KOTUS, M. – PAVLÍK, Ľ. 2018. The possibility of increasing the wearing resistance of mulcher tools. In Acta Technologica Agriculturae, vol. 21, no. 2, pp.87–93

VOTAVA, J. – KUMBÁR, V. – POLCAR, A. 2016. Optimisation of heat treatment for steel stressed by abrasive erosive degradation. In Acta Universitatis Agriculturae et Silviculturae Mendelianae Brunensis, vol. 64, no. 4, pp. 1267–1277.

VOTAVA, J. – KUMBÁR, V. 2014. Application of hard metal weld deposit in the area of mixing organic materials. In Acta Universitatis Agriculturae et Silviculturae Mendelianae Brunensis, vol. 62, no. 5, pp. 1161–1169.

VOTAVA, J. – KUMBÁR, V. – POLCAR, A. – FAJMAN, M. 2020 Change of mechanical properties of zinc coatings after heat treatment. In Acta Technologica Agriculturae, vol. 23, no. 1, pp. 7–11.

sciendo

DOI: 10.2478/ata-2020-0030



Acta Technologica Agriculturae 4
Nitra, Slovaca Universitas Agriculturae Nitriae, 2020, pp. 190–194

# DESIGN OF ARTIFICIAL LIGHTING IN BROILER HOUSING

Peter MORVAI*, Miroslav ŽITŇÁK, Jana LENDELOVÁ

Slovak University of Agriculture in Nitra, Slovak Republic

The work aim is to propose lighting system designs that would satisfy the broiler welfare in terms of intensity; wavelength; switching interval; and energy savings, and would help farmers to reduce the unit costs. BuildingDesign software with Wils 7.0.342 module was used to design suitable lighting, calculate and visualize it. By optimizing the required parameters and energy performance of system, four final designs were prepared with the appropriate evaluation with respect to the acquisition price and return on investment. The original lighting system included a combination of 68 pcs. of tungsten and fluorescent lamps with consumption of 2.17 kWh and a minimum illumination intensity of 7.02 lx. Measurements were conducted at 212 points of the control grid. Artificial lighting is the only light source in an environment of eco-friendly controlled farm. Based on the research analyses, there were proposed four lighting system alternatives with various light intensity; wavelength; switch-on interval; and energy savings. In terms of light intensity, all four designs meet the animal welfare requirements. The most advantageous alternative in the long term is design no. 4 with consumption of 0.734 kWh per one cycle (with energy savings of 66.17% in contrast to the original lighting), in which the intermittent switching mode showed a power savings of 56% and lighting intensity regulation of 40% while maintaining a minimum lighting intensity of 20 lx (total savings for switching and regulation reached up to 73.7%). By utilizing modern approaches, appropriate light colour and lighting quality suitable for broiler breeding were achieved.

**Keywords:** welfare; artificial lighting; broiler breeding; intermittent switching mode; light intensity

Welfare issues can be frequently observed in both conventional and organic production of broiler chickens. In order to efficiently reduce their impacts, it has been suggested to provide stimulating, enriched environments (Riber et al., 2018; Mihina et al., 2012). Furthermore, rearing chicken in high-density environments results in a range of animal welfare problems (Matauschek et al., 2006). As commercial poultry farming has been gaining popularity in recent years, it is necessary to constantly improve the feeding and lighting elements (Pitesky et al., 2019). The only light source for chickens in an environmentally controlled chicken house is artificial lightning. Therefore, light wavelength (quality), light intensity (quantity), and light period (regime) have become major factors in modern poultry management (Yang et al. 2016). As highlighted by Lewis and Gous (2007), broiler chickens have been reared at commercial facilities throughout the past decades with either continuous (24 h of light), or near continuous illumination (23 h light and 1 h of dark) in order to maximize the feed intake and growth rate. Newberry (1999) defined environmental enrichment as a modification of the environment, in which the captive animals live, thereby increasing their behavioural possibilities and leading to improvements of the biological functions. This means that environmental enrichment is provided with the purpose of:

1. increasing the occurrence and range of the animals' normal or species-specific behaviour;
2. preventing the development of abnormal behaviour or reducing its extent and complexity;
3. increasing the positive exploitation of the environment (e.g. utilization of an outdoor area);
4. increasing the animals' ability to handle behavioural and physiological challenges.

It is emphasized that environmental enrichment must be biologically relevant to be effective. In certain countries, conventional bulbs are commonly used for lighting in poultry halls. Insufficient lightning of poultry farms leads to stress, negative impacts on feed intake and physical activity. Given the favourable effect of green light on performance characteristics, their usage is recommended for broiler chicken production (Gharahveysi et al., 2019). The aim of work was to analyse the current state of intensity and energy balance of the original lighting of the experimental farm, design alternative types and operational solutions and perform overall evaluation of changes in lighting, energy performance and return on investment of individual solutions in favour of improving the broiler breeding conditions.

## Material and methods

The research was carried out at a standardized poultry farm for broiler breeding in the western Slovak lowland. The experimental farm includes six identical halls designed for breeding of broiler chickens ROSS 308. The chickens are

**Contact address:** Peter Morvai, Slovak University of Agriculture in Nitra, Faculty of Engineering, Department of Building Equipment and Technology Safety, Nitra, Slovakia; e-mail: petermorvai@yahoo.co.uk

reared in cycles of 32 to 35 days with a break of 14 days between cycles. The lighting measurement experiment was performed in experimental hall 3. The hall length is 101 m; the width including walkways for the operator is 12.6 m; the wall height is 2.3; and the ridge height is 3.8 m with a total area of 1,010.0 $m^2$. Breeding halls based on steel load-bearing structures and structural insulated sheathing were built in the 1980s in the former Czechoslovakia. In all the experimental farm halls, the feeding system, water supply, heating and ventilation were reconstructed. Furthermore, partial reconstruction of the electrical wiring was carried out. These systems are in a well-maintained and satisfactory condition. External walls, ceiling, floor as well as lighting, are in their original state with minimal interference. For these systems, reconstruction is necessary to improve both animal welfare and building energy efficiency. The original lighting system consists of a combination of 68 pcs. of tungsten and fluorescent lamps with consumption of 2.17 kWh (Morvai, 2019). Artificial lighting is the only light source in an environmentally controlled farm. Sockets with E27 threads (International Protection IP20) are suspended and evenly distributed in four rows. The current state assessment was performed by measuring the illumination and contrasting it with corresponding statistical and general assessment of effectiveness. BuildingDesign software with Wils 7.0.342 module was used to design alternative lighting, calculate and visualize new lighting. The lighting switching interval was selected based on the literature in order to achieve optimal growth parameters. Specific lighting design with respect to energy savings and maintaining given lighting intensity and light colour is a less investigated research field. The proposal consisted of alternatives that would be suitable for the welfare of broiler breeding and would help farmers reduce unit costs while maintaining adequate light intensity, wavelength, switching interval and energy savings. This work pays attention to the design of new lighting with LED (Light Emitting Diode) chips and showing the possible savings of electricity and return on investment by comparing the new design with the original lighting.

### Light intensity measurement

Layout of the luminaries and layout of the control grid for measuring the illumination intensity are shown in Fig. 1. The illumination intensity was measured at a height of 0.2 m from the floor – animal welfare zone – with five repetitions. The illumination intensity measurement started after stabilization of the luminous flux after the lightning was switched on (approx. after 20 minutes) and was subsequently carried out at checkpoint locations in a regular rectangular grid throughout the entire reference plane or functional parts. Illumination measurement E (1×) was carried out in the evening to exclude daylight.

The luxmeter UNI-T UT382 with illumination range of 0–20,000 lux and accuracy of ±3% was used for the purposes of illumination measuring. Professional measuring instrument GLM 100C with measuring range up to 100 m and accuracy of ±1.5 mm was used to measure distances indoors. BuildingDesign software was utilized to design, calculate and visualize new lighting.

By means of the BuildingDesign software, 3D geometry of the object was sketched, to which a uniformly distributed system of luminaries and a set of evaluated points for four luminary designs with different intensity and illumination curves were inserted. Minimal values of illumination and uniformity were used for the designs according to the STN EN 12464-1: 2011. Software with active calculation module Wils 7.0.342 calculated lighting system parameters according to the STN EN 12464-1: 2011. Considering the cost calculation of designs, only the lighting system cost (lamp and light source) was taken into account; the power supply system reconstruction (labour and materials) was not included in the final price calculation.

## Results and discussion

### Experimental hall original illumination results

When assessing the lighting in a room, the purpose a given room will serve is crucial (Balková, 2013). By measuring the illumination according to STN EN 13032-1+A1: 2012, the current illumination intensity and critical points with the lowest illumination values were observed. Calculated values are shown in Table 1.

The average illumination provided by the original hall lighting system does not meet the legislative requirements for broiler breeding. Light intensity affects activity, taking rest and food intake. High light intensity extremely increases the movement and stress of chickens (Buyse et al., 1996; Olanrewaju et al., 2011; Xie et al., 2008; Kim et al., 2013). At low light intensity, the animal movement activity is reduced (Hartini et al., 2002, Olanrewaju et al., 2006; Lien et al., 2007). The best results in terms of body weight and FCR (feed conversion ratio) were observed at 50 lux green light. The light colour effect on both haemoglobin and

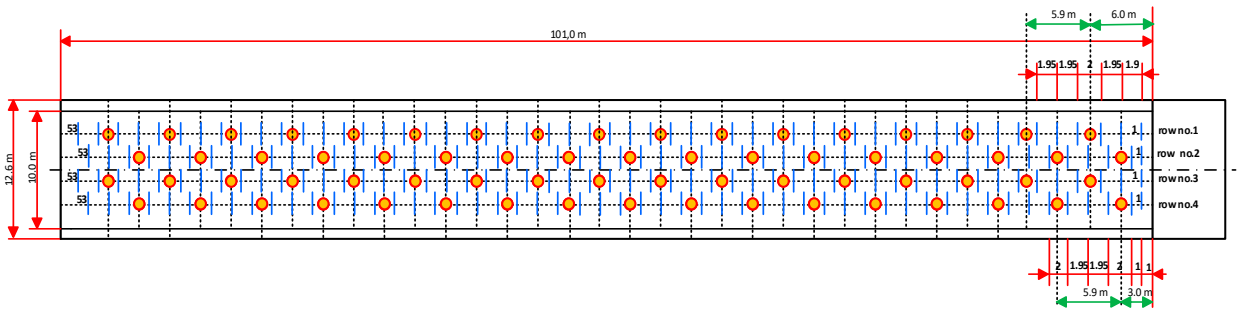


**Fig. 1** Location of the luminaries and layout of the control network to measure the illumination intensity in the poultry house (circles indicate the original lighting elements, vertical bar marks represent the measurement points of the lighting)

**Table 1** Measurement results of original illumination in experimental hall

| Hall no. 3 | Ē (lx) | U (%) | Ē – U (lx) | Ē + U (lx) | $E_{min}$ (lx) | *r* |
|---|---|---|---|---|---|---|
| | 11.59 | 14 | 9.97 | 13.21 | 7.02 | 0.60594 |

Ē – average illumination, lx; U – permissible measurement uncertainty, %; *r* – uniformity of illumination ($r \geq 0.5$)

haematocrit levels was significant ($p < 0.05$) (Gharahveysi et al., 2019). Thanks to the beneficial effect of green and blue lights on performance, it is recommended to use them in broiler breeding (Gharahveysi et al., 2019; Halevy et al., 1998). In order to meet the welfare requirements, an intensity ranging from 15 to 50 lx was selected for the design of optimal lighting system for broiler breeding. The lighting system was designed for operation with intensity suitable for the given range. The simulation program allowed setting the colour temperature of lamps from 1 to 10,000 K. The lifetime is 1,000 h for incandescent lamps, 8,000 h for fluorescent lamps and a significantly longer 50,000 h or more for LED lamps. Other advantages of LEDs are small size, specific wavelength, low thermal radiation, adjustable intensity and high photoelectric conversion efficiency. Thanks to these advantages, LEDs are ideal for supporting the broiler breeding in a controlled environment with artificial lighting (Yang et al., 2016). Luminaries are produced as standard with LED chips with colour temperature of 2800 K, 4000 K and 6,500 K. By rationalizing the electricity consumption by using LED lights, it is possible to reach 40–70% savings of electric energy (Morvai et al., 2018). By designing LED lighting, there were achieved suitable light intensity; switching interval; and light colour, which will improve broiler breeding conditions and meet the requirements for more energy efficient installation at the same time.

## Optimized designs of the experimental hall lighting

An overview of the lighting results for proposed designs no. 1–4 is shown in Tab. 2

### Design no. 1

This design utilized the MAS LED bulb DT11W with E27 base and a colour temperature of 2,700 K with a luminous efficacy of 96 lm·W$^{-1}$. The quantity and layout of the luminaries is identical to the original version with a supplement of 1 luminary at the hall entrance. The total number of installed LEDs was 69 pcs. with power of 759 Wh (0.6 W·m$^{-2}$) without the need to change the power supply.

### Design no. 2

This design used the DUST LED PS 1xT8/60-IP65 with LED light source T8-840-10W-4000K, 110 lm·W$^{-1}$ and 1BC/6 8 W light sources with E27 base with light efficiency of 100 lm·W$^{-1}$. There were 14 pcs. of LED tubes in rows no. 1 and no. 3, and 13 pcs. of LED tubes and 2 pcs. of LED bulbs in rows no. 2 and no. 4, which were evenly distributed throughout the space. The total number of installed LED sources was 58 pcs. with power input of 572 Wh (0.6 W·m$^{-2}$).

### Design no. 3

This design used the 1BC/6-8W, lamps with E27 base, colour temperature of 2,700 K, and luminous efficacy of 100 lm·W$^{-1}$. In rows no. 1 and 3, there were used 14 pcs. of LED bulbs in each; 15 pcs. of LED bulbs were in rows no. 2 and 4. These were evenly distributed throughout the space. The total number of installed LED sources was 58 pcs. with power input of 464 Wh (0.6 W·m$^{-2}$).

### Design no. 4

For this design, LED 118-13W-4000K-Ra80-IP65 luminaries with integrated LED, colour temperature of 4,000 K, and luminous

**Table 2** Illumination values for individual designs

| Design no. 1 | Min. value Ē (lx) | Average value Ē (lx) | Required value Ē (lx) | Max. value Ē (lx) | Uniformity min. 0.6 |
|---|---|---|---|---|---|
| **Corridor no. 1** | 14.60 | 19.50 | 10 | 22.20 | 0.75 |
| **Corridor no. 2** | 11.00 | 18.40 | 10 | 19.90 | 0.60 |
| **Breeding part** | 19.30 | 31.90 | 20 | 35.70 | 0.61 |
| **Design no. 2** | **Min. value Ē (lx)** | **Average value Ē (lx)** | **Required value Ē (lx)** | **Max. value Ē (lx)** | **Uniformity min. 0.6** |
| **Corridor no. 1** | 11.90 | 16.60 | 10 | 20.20 | 0.72 |
| **Corridor no. 2** | 14.90 | 16.80 | 10 | 21.00 | 0.84 |
| **Breeding part** | 31.50 | 42.20 | 20 | 60.00 | 0.75 |
| **Design no. 3** | **Min. value Ē (lx)** | **Average value Ē (lx)** | **Required value Ē (lx)** | **Max. value Ē (lx)** | **Uniformity min. 0.6** |
| **Corridor no. 1** | 10.90 | 13.50 | 10 | 15.60 | 0.80 |
| **Corridor no. 2** | 12.00 | 13.50 | 10 | 15.70 | 0.89 |
| **Breeding part** | 23.10 | 29.80 | 20 | 43.30 | 0.78 |
| **Design no. 4** | **Min. value Ē (lx)** | **Average value Ē (lx)** | **Required value Ē (lx)** | **Max. value Ē (lx)** | **Uniformity min. 0.6** |
| **Corridor no. 1** | 11.40 | 15.40 | 10 | 18.40 | 0.75 |
| **Corridor no. 2** | 13.70 | 16.40 | 10 | 20.70 | 0.83 |
| **Breeding part** | 35.00 | 53.00 | 20 | 71.00 | 0.67 |

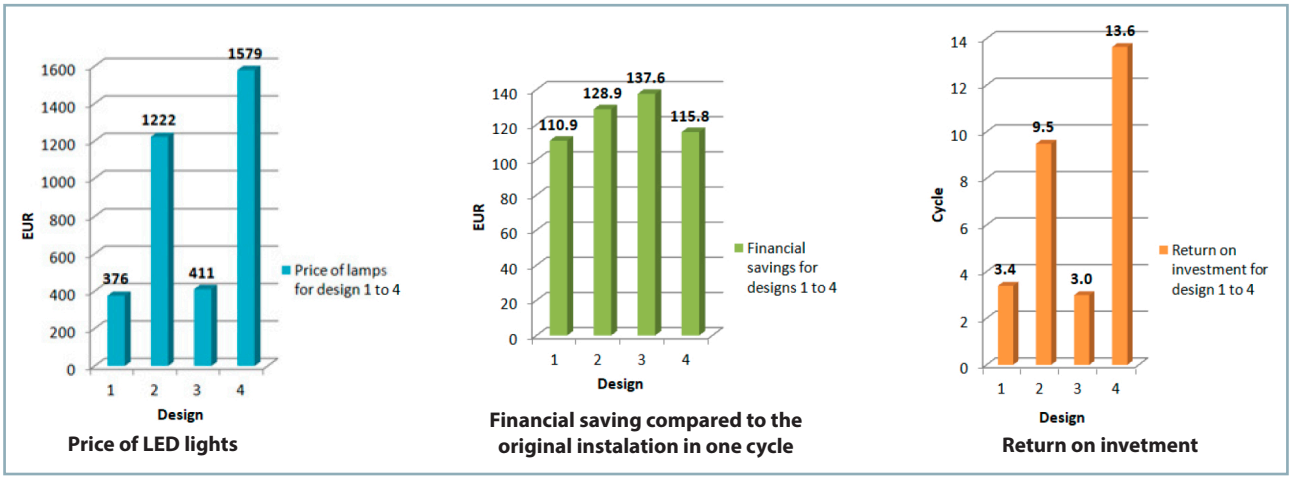


**Fig. 2** Price of LED lamps, energy savings and return on investment for designs 1–4

efficacy of 100 lm·W$^{-1}$ were used. Rows no. 1 and 3 included 14 pcs. of LED lamps each and rows no. 2 and 4 included 13 pcs. of LED lamps and 2 pcs. of LED bulbs. These were evenly distributed throughout the space. Total number of installed LED sources was 58 pcs. with power input 734 Wh (0.6 W·m$^{-2}$).

Tab. 2 shows calculated illumination and uniformity values using BuildingDesign with Wils 7.0.

## Consumption comparison of the original installation and designs no. 1–4

Tab. 3 shows the consumption and price of consumed energy per cycle and eight cycles (maximal expected number of cycles per year) for designs no. 1–4 and original installation.

Price of LED lamps, financial savings and return on investment for designs no. 1–4 is shown in Fig. 2.

The original lighting switch setting is continuous lighting (CL = 21 h on, 3 h off). Lighting system is off from 1:35 to 3:05, from 13:35 to 15:05 throughout the entire cycle. According to Halevy et al. (2006); Guevara et al. (2015); Yang et al. (2016), the light management is an effective tool to improve poultry performance. Switching automation and light colour for the turn will be set as shown in Fig. 2. Continuous lighting (CL = 23 h on, 1 h off) was selected for the period from the 1$^{st}$ to 6$^{th}$ day. According to Gharahveysi et al. (2019), green light accelerates muscle growth and stimulates growth at an early age and blue light stimulates growth at an older age. Adjustment using green light provides a mechanism to accelerate growth (Halevy et al. 1998). Studies show that intermitted lighting (IL = 1 h on – 3 h off, 1 h on – 3 h off, 1 h on – 3 h off, 1 h on – 3 h off, 2 h on – 6 h off) is suitable for broiler breeding from the 7$^{th}$ day to the cycle end (32–35 days). The difference between the average daily increase (ADG) of broilers is minimal for CL and IL breeding. From the 7$^{th}$ to 21$^{st}$ day, ADG = 1.7 g ±0.9 g and from the 22$^{nd}$ to 35$^{th}$ day, ADG = 0.1 g ±1.75 g. Mortality at IL is lower by 0.6% ±0.22% (Rodrigues and Choct, 2019). Considering the mortality, under experimental conditions with IL and 20,000 broilers, it would be lower by 120 ±44 pcs.

By selecting IL for one shift, there are achieved electricity savings necessary to illuminate the operation compared to the original installation switching mode 820.26 kW: 300.51 kW by design no. 1; 216.22 kW design no. 2; 175.39 kW design no. 3; 277.45 kW design no. 4 (56% savings). RGB (RED, GREEN, BLUE) LED chips can be installed in the luminaries to achieve the desired light colour and intensity.

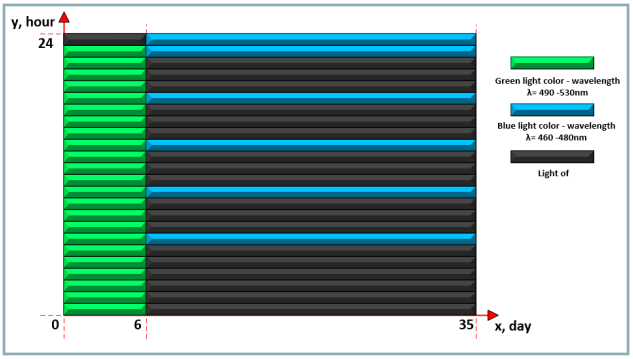


**Fig. 3** Design of switching lights and light colour for broiler breeding

**Table 3** Consumption and price for consumed electricity for 8 turns

| Lightning variants | Power input P (kWh) | Number of hours for 32 days × 21 h t (h) | Total consumption per cycle P (kWh) | Price of consumed energy for one cycle – 0.12 € per kWh (€) | Price per year for 8 cycles (€) |
|---|---|---|---|---|---|
| **Existing installation** | 2.170 | 672 | 1458.24 | 174.99 | 1399.91 |
| **Design no. 1** | 0.795 | 672 | 534.24 | 64.11 | 512.87 |
| **Design no. 2** | 0.572 | 672 | 384.38 | 46.13 | 369.01 |
| **Design no. 3** | 0.464 | 672 | 311.81 | 37.42 | 299.34 |
| **Design no. 4** | 0.734 | 672 | 493.25 | 59.19 | 473.52 |

## Conclusion

The initial illumination measurements showed that the original lighting system is not suitable in terms of the technical condition of the luminaries and light intensity with regards to the animal welfare. By designing the switching mode and light colour, both broiler welfare, as well as their more efficient weight gain, can be achieved. In terms of light intensity, all four designs are suitable in terms of animal welfare. The price of designs no. 1 and 3 is the lowest, since merely replacement of light sources with IP20 protection was taken into consideration. In comparison to design no. 1, design no. 3 is equipped with a smaller number of lamps with higher efficiency. The fastest return on investment was showed by design no. 3. Designs no. 2 and 4 used luminaries with IP 65 protection, which resulted in their four- or five-fold increased price in contrast to cheaper designs. Luminaries with IP65 protection are appropriate for the breeding environment. Return on investment of design no. 2 is 9.5 cycles; return on investment of design no. 4 is 13.6 cycles. Throughout one year, there are anticipated 8 to take place. The extreme illumination values are 31.5–60 lx for design no. 2 and 35–75 lx for design no. 4. The luminaries in design no. 4 are fitted with adjustable ballasts (or with Digital Addressable Lighting Interface), for which the illumination intensity can be adjusted using WIFI 666 (for DALI with push button or control unit with light intensity sensors). The most advantageous alternative in the long term is design no. 4 with a consumption of 0.734 kWh, in which the switching mode can achieve savings of 56% and regulation of lighting intensity of 40% while maintaining a minimum lighting intensity of 20 lx (total savings up to 73.7%). The design according to Fig. 2 can be achieved by installing RGB LED chips in IP65 luminaries. Switching and setting the colour of luminaries is possible using the application version in Microsoft Visual C # software. The work results can be used to design the lighting at similar standardized farms.

## Acknowledgment

This publication was supported by the Operational Programme Integrated Infrastructure within the project: Sustainable smart farming systems taking into account the future challenges 313011W112, cofinanced by the European Regional Development Fund.

## References

BALKOVÁ, M. 2013. Assessing of daylight factor values depending on window opening structures in model room. In Acta Technologica Agriculturae, vol. 16, no. 4, pp. 95–98.

BUYSE, J. – SIMONS, P. C. M. – BOSHOUWERS, F. M. G. – DECUYPERE, E. 1996. Effect of intermittent lighting, light intensity and source on the performance and welfare of broilers. In Worlds Poultry Science Journal, vol. 52, no. 2, pp. 127–130.

GHARAHVEYSI, S. – IRANI, M. – KENARI, T. A. – MAHMUD, K. I. 2019. Effects of colour and intensity of artificial light produced by incandescent bulbs on the performance traits, thyroid hormones, and blood metabolites of broiler chickens. In Italian Journal of Animal Science, vol. 19, no. 1, pp. 1–7.

GUEVARA, B. D. M. – PECH, P. S. – ZAMORA, B. R. – NAVARETTE, S. L. F. – MAGANA, S. H. F. 2015. Performance of broilers reared under monochromatic Light Emitting Diode supplemental lighting. In Brazilian Journal of Poultry Science, vol. 17, no. 4, pp. 553–558.

HALEVY, O. – BIRAN, I. – ROZENBOIM, I. 1998. Various light source treatments affect body and skeletal muscle growth by affecting skeletal muscle satellite cell proliferation in broilers. In Comparative Biochemistry and Physiology – Part A: Molecular and Integrative Physiology, vol. 120, no.2, pp. 317–323.

HALEVY, O. – PIESTUN, Y. – ROZENBOIM, I. – YABLONKA-REUVENI, Z. 2006. In ovo exposure to monochromatic green light promotes skeletal muscle cell proliferation and affects myofiber growth in post hatch chicks. In American Journal of Physiology-Regulatory Integrative and Comparative Physiology, vol. 290, no. 4, pp. R1062– R1070.

HARTINI, S. – CHOCT, M. – HINCH, G. – KOCHER, A. – NOLAN, J. V. 2002. Effects of light intensity during rearing and beak trimming and dietary fiber sources on mortality, egg production, and performance of ISA brown laying hens. In Journal of Applied Poultry Research, vol. 11, no. 1, pp. 104–110.

KIM, M. J. – PARVIN, R. – MUSTAG, M. M. H. – HWANGO, J. – KIM, J. H. – NA, J. C. – KIM, D. W. – KANG, C. D. – CHO, K. O. – YANG, C. B. – CHOI, H. C. 2013. Growth performance and haematological traits of broiler chickens reared under assorted monochromatic light sources. In Poultry Science, vol. 92, no. 6, pp. 1461–1466.

LEWIS, P. D. – GOUS, R. M. 2007. Broilers perform better on short or step-up photoperiods. In South African Journal of Animal Sciences, vol. 37, no. 2, pp. 90–96.

LIEN, R. J. – HESS, J. B. – MCKEE, S. R. – BILGILI, S. F. – TOWNSEND, J. C. 2007. Effect of light intensity and photoperiod on live performance, heterophil-to-lymphocyte ratio, and processing yields of broilers. In Poultry Science, vol. 86, no. 7, pp. 1287–1293.

MATAUSCHEK, A. – PIEPHO, H. P. – BESSEI, W. 2006. The effect of feather eating on feed passage in laying hens. In Poultry Science, vol. 85, no. 1, pp. 21–25.

MIHINA, Š. – KAŽIMÍROVÁ, V. – COPLAND, T. A. 2012. Technology for Farm Animal Husbandry. Nitra : Slovak University of Agriculture in Nitra, 99 pp.

MORVAI, P. – ZITŇÁK, M. – PAULOVIČ, S. 2018. Rationalization of electricity consumption in households. In Acta Technologica Agriculturae, vol. 21, no. 2, pp. 69–74.

MORVAI, P. – ŽITNÁK, M. 2019. Backup diesel generator calculation for farms. In Rural Buildings in European Regions: RUBER 2019, pp. 38–42.

NEWBERRY, R. C. 1999. Exploratory behaviour of young domestic fowl. In Applied Animal Behaviour Science, vol. 63, no. 4, pp. 311–321.

OLANREWAJU, H. A. – THAXTON, J. P. – DOZIER III, W. A. – PURSWELL, J. – ROUSH, W. B. – BRANTON, S. L. 2006. A review of lighting programs for broiler production. In International Journal of Poultry Science, vol. 5, no. 4, pp. 301–308.

OLANREWAJU, H. A. – MILLER, W. W. – MASLIN, W. R. – COLLIER, S. D. 2011. Effect of varying light intensity on welfare indices of broiler chickens grown to heavy weights. In Poultry Science, vol. 10, no. 8, pp. 590–596.

PITESKY, M. – THORNGREN, A. – NIEMEIER, D. 2019. Feeding and lighting practices on small-scale extensive pastured poultry commercial farms in the United States. In Poultry Science, vol. 98, no. 2, pp. 785–788.

RIBER, A. B. – WEERD, H. A – JONG, I. C. – STEENFELDT, S. 2018. Review of environmental enrichment for broiler chickens. In Poultry Science, vol. 97, no. 2, pp. 378–396.

RODRIGUES, I. – CHOCT, M. 2019. Feed intake pattern of broiler chickens under intermittent lighting: Do birds eat in the dark? In Animal Nutrition, vol. 5, no. 2, pp. 174–178.

XIE, D. – WANG, Z. X. – DONG, Y. L. – CAO, J. – WANG, J. F. – CHEN, J. L. – CHEN, Y. X. 2008. Effects of monochromatic light on immune response of broilers. In Poultry Science, vol. 87, no. 8, pp. 1535–1539.

YANG, Y. F. – YU, Y. H. – PAN, J. M. – YING, Y. B. – ZHOU, H. 2016. A new method to manipulate broiler chicken growth and metabolism: Response to mixed LED light system. In Scientific Reports, vol. 6, no. 2597.

STN EN 12464-1: 2011. Light and lighting. Lighting of workplaces. Part 1: Indoor workplaces. (In Slovak: Svetlo a osvetlenie. Osvetlenie pracovísk. Časť 1: Vnútorné pracoviská).

STN EN 13032-1+A1: 2012. Light and lighting. Measurement of photometric data of lamps and luminaries. Part 1: Measurement and file form. (In Slovak: Svetlo a osvetlenie. Meranie fotometrických údajov svetelných zdrojov a svietidiel. Časť 1: Meranie a formulár súborov).

sciendo

DOI: 10.2478/ata-2020-0031

*Acta Technologica Agriculturae 4/2020* *Dmytro Derevjanko et al.*

Acta Technologica Agriculturae 4
Nitra, Slovaca Universitas Agriculturae Nitriae, 2020, pp. 195–200

# MATHEMATICAL MODEL OF UNIFORM CEREAL CROPS SEEDING USING A DOUBLE-DISK COULTER

Dmytro DEREVJANKO[1], Ivan HOLOVACH[2], Volodymyr BULGAKOV[2]*, Yevhen IHNATIEV[3], Ladislav NOZDROVICKÝ[4]

[1]Zhytomyr National Agroecological University, Ukraine
[2]National University of Life and Environmental Sciences of Ukraine
[3]Tavria State Agrotechnological University, Ukraine
[4]Slovak University of Agriculture in Nitra, Faculty of Engineering, Slovakia

The paper provided presents a new design of two-disk wide-row coulter that ensures uniform distribution of seeds to an even bed at the furrow bottom, as well as preserving of optimal distances between the seeds. Seeds fall from the seed tube of coil sowing apparatus onto a metal distribution plate with staggeringly arranged metal pins, which distribute the seeds to furrow bottom surface in a form of separate strips. To substantiate the kinematic and constructive parameters of proposed coulter design, a mathematical model for transport of seeds along the surface of a distribution plate was developed and the Cauchy problem for a system of the second-order quasi-linear differential equations was solved by the finite difference methods using embedded software procedures in mathematical software packages (Mathcad, Maple, etc.). The finite-difference method implementation was carried out using computer software allowing the determination of coordinates of seeds and, if necessary, changing of direction of their movement by adjusting the coulter operation to improve the distribution of seeds to soil in order to reduce the injury to them, which ultimately can contribute to an increased yield. Coverage of the plate surface and distribution pins with a rubber material can also contribute to a significant reduction in seed injury during sowing.

**Keywords:** sowing; seeding uniformity; differential equations; finite difference methods

Nowadays, existing coulters with seed drills show several disadvantages, e.g. the two-disk narrow-row coulter produces two grooves during the sowing process that are separated by a soil hill, at the bottom of which the seeds are distributed rather densely, almost next to each other – this leads to the significant deteriorations during the germination of seedlings, postpones the formation of root systems and stalks, impairs their utilization of water, nutrients, solar energy, and prevents the formation of vegetative and reproductive organs, which results in a significant decrease in harvest yield (Gursoy and Guzel, 2010; Karaj and Muëller, 2010).

For this very reason, the development of a more advanced coulter design, which would eliminate these disadvantages (Kovalyshyn et al., 2015), is essential and the scientific substantiation of cereal sowing by such design is a very topical scientific issue.

Multiple scientist (Prisyazhnyuk, 2013; Turan et al., 2014; Turan et al., 2015; Vasylkovska et al., 2016; Pylypaka et al., 2018) have dealt with the proposition of fundamental scientific foundations for the theory of mutual influence of working surfaces of mechanisms and seeds in order to find the optimal parameters of their work.

Modern studies on the sowing uniformity are dedicated mainly to determination of this parameter on existing crops by means of modern technical means, such as RGB cameras; multispectral imagery; hyperspectral imagery; and thermal camera (Liu et al., 2017). Neugschwandtner et al. (2020) investigated the effect of sowing uniformity on weed inhibition or crop quality. Furthermore, Egli and Rucker (2012) observed and recorded the dependencies between energy necessary for seed germination, as well as seedlings uniformity under various conditions, and sowing uniformity. Recently, several researches have focused on the investigation of technical solutions for increasing the sowing uniformity of cereal crops using the seeders for continuous sowing: Maleki et al., 2006 paid attention to improvement of form and design of bobbin sowing apparatus; however, due to the considerable distance of dosing device from sowing machine, as well as reach of a long corrugated seed tube, there was observed a decrease in sowing uniformity. Additional issues also arise as a result of chaotic mutual beating of seeds with each other and with seed tube walls, and fact that seeds are not distributed to soil at constant speed, which leads to incidental injuring of seeds and their displacement from initial appropriate position. The

**Contact address:** Volodymyr Bulgakov, National University of Life and Environmental Sciences of Ukraine;
e-mail: vbulgakov@meta.ua

proposed design of sowing apparatus is intended for reduction of influence of mentioned negative factors and the paper presented aims to substantiate the rational design and kinematic parameters of a two-disk wide-row coulter that would ensure the uniform distribution of seeds to an even bed at the furrow bottom during sowing, optimal distances between seeds, and mitigation of injury to seeds.

## Material and methods

The general design of two-disk double-row coulter with seed drill is well-known, therefore, the focus will be put on its seed tube with a two-stream distributor. However, during sowing, two grooves are formed, at the bottom of which the seeds are often nearly entirely ovelappping, which leads to mutual interference of plants during sprouting and overall negative impact on the crop.

Traditional coulter type is disadvantageous, because the sowing gear included is of open type and is manufactured in an upright position; furthermore, it lacks devices for pre-compaction of the furrow bottom and walls prior to planting the seeds, leading to violation of the intended uniform distribution of seeds and deterioration of the crop yield.

This paper presents a new design of coulter with wide-working width (Derevjanko et al., 2017), which ensures an even distribution of cereal seeds to the furrow bottom during sowing and optimal distances between the seeds (Fig. 1).

Double-disk wide-row coulter works as follows: it is installed on the housing [1], which is attached by a bracket [2] to the drill frame; the disk knives [3], inclined at an angle, cut the soil layer at a pre-determined depth. The disk knives [3] mounted on hubs [4] rotate freely, when the drill moves. Paw-razor [7] spreads the soil, and its lower base [8] produces a smooth furrow and compacts it. The seeds go through the seed tube [5] and are fed down to the scattering and distribution plate [9] (inclined at an angle to the horizon) with the help of distributor [6]. Since the metal rods with a rubber-coated outer surface [10] are fastened to the plate [9], the seeds slip around the rods [10] and are transported down and evenly distributed at the bottom of compacted furrow due to gravity. Subsequently, the furrow is covered with potting soil, which is then rolled up.

### Research methods

For the purposes of this research, the methods of higher mathematics, theoretical mechanics, analysing the graphical dependencies, as well as software packages for the numerical calculation and mathematical modelling, were utilized.

The main emphasis was on the process of transport of seeds along the surface of rectangular distribution plate, which would ensure uniform distribution of seeds to the even bed at the furrow bottom formed by vomer disks (Derevjanko et al., 2017). In order to achieve this goal, it is necessary to compile the differential equations of seeds motion over the surface specified plate. However, to compile these differential equations, it is necessary to develop an equivalent force scheme for the interaction of seeds with rectangular distribution plate surface (Fig. 2).

In mathematical modelling, the mass of one seed was determined based on its geometric dimensions, the variation range of which was described by Kuzminskyi et al. (2018).

According to the received power circuit, the following forces act on individual piece of seed:

1. **Force of weight $\bar{G}$ of a seed *M*, equal to:**

$$G = mg \quad (1)$$

where:
*m* – seed mass
*g* – gravity force acceleration

2. **$\bar{N}$ – normal plate surface response.**

3. **Friction force $\bar{F}_f$, the value of which is equal to:**

$$F_f = f \cdot N \quad (2)$$

where:
*f* – coefficient of friction

4. **Force of air resistance $\bar{F}_a$, the value of which is determined as follows:**

$$F_a = k \cdot m \cdot V^2 \quad (3)$$

where:
*k* – air drag coefficient when moving the seeds over the plate
*m* – seed weight
*V* – seed motion speed over the plate surface

According to the basic law of dynamics and based on the presented power scheme (Fig. 2), the seed motion equation for plate surface in vector form is:

$$m\bar{a} = \bar{N} + \bar{F}_f + F_a + \bar{G} \quad (4)$$

where:
*a* – movement acceleration of seeds over the plate surface

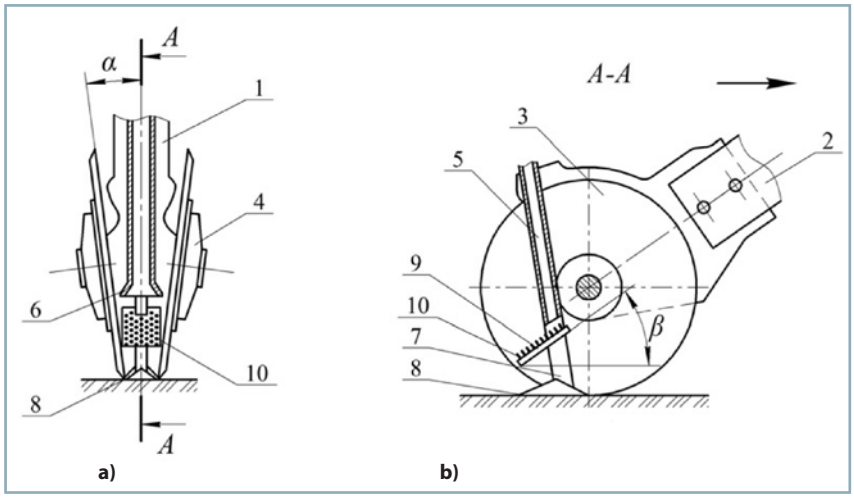


**Fig. 1** Improved dual drive design of a wide-width coulter
a) front view; b) side view from the middle: 1 – case; 2 – drill frame; 3 – circular knives; 4 – hub; 5 – seed tube; 6 – distributor; 7 – paw razor; 8 – the razor paw lower base; 9 – distribution plate; 10 – pins

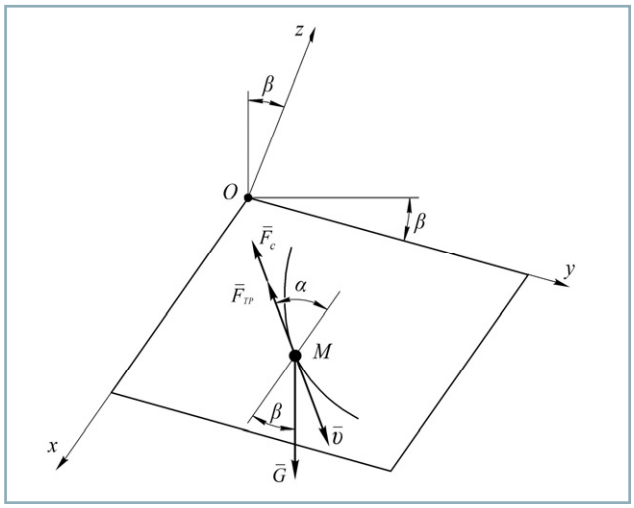


**Fig. 2** Equivalent scheme of forces acting on the individual piece of seed as it moves along the distribution plate surface

Subsequently, the absolute Cartesian coordinate system *xOyz* is selected, in which the motion of seeds under the action of forces indicated in Fig. 2 is taken into account. The axes *Ox* and *Oy* of this coordinate system are in the plate plane located at an angle β to the horizontal plane.

Since the plate is of rectangular shape, the axes *Ox* and *Oy* are directed along the sides of this rectangle, as shown in Fig. 2. The axis *Oz* is directed upwards along the normal to the plate plane. As a result, the *Oz* axis forms with the vertical. Point *O* is the origin of specified *xOyz* coordinate system.

In terms of the Cartesian coordinate system *xOyz*, Eq. 4 has following form:

$$\begin{aligned} m\ddot{x} &= -F_\alpha \cos\alpha - F_f \cos\alpha \\ m\ddot{y} &= -F_\alpha \sin\alpha - F_f \sin\alpha + G\sin\beta \\ m\ddot{z} &= N - G\cos\beta \end{aligned} \quad (5)$$

where:

α – angle between the velocity vector $\bar{V}$ of seed on the plate plane and the axis *Ox* (Fig. 2)

Since this paper considers the case of continuous separation of seeds on the plate surface, its movement along the *Oz* axis will be absent, therefore, $z = 0$, $\dot{z} = 0$ and $\ddot{z} = 0$. The Eq. 5 is simply an equilibrium equation, i.e. a static equation. Hence, from Eq. 5, which has following form in this case: $0 = N - G\cos\beta$, one gets the value of normal reaction *N* of plate:

$$N = G\cos\beta \quad (6)$$

Taking into account Eq. 1, there is:

$$N = mg\cdot\cos\beta \quad (7)$$

Considering the Eqs. 2, 3 and 7, Eq. 5 takes the following form:

$$\begin{aligned} m\ddot{x} &= -mk\cdot V^2\cos\alpha - fmg\cdot\cos\beta\cdot\cos\alpha \\ m\ddot{y} &= -mk\cdot V^2\sin\alpha - fmg\cdot\cos\beta\cdot\sin\alpha + mg\cdot\sin\beta \end{aligned} \quad (8)$$

Current value of the functions cos α and sin α can be determined from known expressions for the purposes of determination of the guiding cosines of velocity vector $\bar{V}$ through its projection on the coordinate axes:

$$\cos\alpha = \frac{\dot{x}}{V} = \frac{\dot{x}}{\sqrt{\dot{x}^2+\dot{y}^2}} \quad (9)$$

$$\sin\alpha = \frac{\dot{y}}{V} = \frac{\dot{y}}{\sqrt{\dot{x}^2+\dot{y}^2}} \quad (10)$$

where:

$\dot{x}, \dot{y}$ – projections of the velocity vector $\bar{V}$ of a point (seeds in this case) on the axes *Ox* and *Oy*, respectively

$V = \sqrt{\dot{x}^2+\dot{y}^2}$ – velocity vector module $\bar{V}$

Substituting Eqs. 9 and 10 into Eq. 8 and reducing both sides of each equation by mass m, the following system of differential equations is finally achieved:

$$\begin{aligned} \ddot{x} &= -k\dot{x}\sqrt{\dot{x}^2+\dot{y}^2} - fg\cdot\cos\beta\frac{\dot{x}}{\sqrt{\dot{x}^2+\dot{y}^2}} \\ \ddot{y} &= -k\dot{y}\sqrt{\dot{x}^2+\dot{y}^2} - fg\cdot\cos\beta\frac{\dot{y}}{\sqrt{\dot{x}^2+\dot{y}^2}} + g\cdot\sin\beta \end{aligned} \quad (11)$$

If the initial conditions are added to Eq. 11, there is:

$$x(0)=x_0;\ y(0)=y_0;\ \dot{x}(0)=V_{x_0};\ \dot{y}(0)=V_{y_0} \quad (12)$$

Ultimately, the Cauchy problem for a system of the second-order quasilinear ordinary differential equations was achieved. The resulting problem has no analytical solution; however, it can be solved using either finite-difference analogues, or by means of procedures built in various software packages (MATHCAD, MAPLE, etc.).

Considering the further problem formulation, during the movement of seeds over the distribution plate, they meet various obstacles, due to which the direction of their movement can change. When using procedures for solving a system of differential equations in mathematical packages, such changes make it necessary to use conditional transition operators that change the solution depending on the value of the functions themselves, which makes it very difficult to build a solution algorithm.

In regard to this issue, it is the most appropriate to use the methods for solving finite-difference analogues of the second-order quasilinear ordinary differential equations proposed above. The first and second derivatives of unknown functions *x*(*t*) and *y*(*t*) in a certain period of time *t* can be represented in this form:

$$\dot{x}(t_i) = \frac{x(t_{i+1})-x(t_i)}{h} \quad (13)$$

$$\dot{y}(t_i) = \frac{y(t_{i+1})-y(t_i)}{h} \quad (14)$$

$$\ddot{x}(t_i) = \frac{\dot{x}(t_{i+1})-\dot{x}(t_i)}{h} = \frac{x(t_{i+2})-2x(t_{i+1})+x(t_i)}{h^2} \quad (15)$$

$$\ddot{y}(t_i)=\frac{\dot{y}(t_{i+1})-\dot{y}(t_i)}{h}=\frac{y(t_{i+2})-2y(t_{i+1})+y(t_i)}{h^2} \quad (16)$$

where:

$h$ – time step (which is a fairly small period of time)

By substituting the difference analogues of derivatives into Eq. 11, where, for a more compact form of its record the following notation is used:

$$x(t_i)=x_i;\ y(t_i)=y_i \quad (17)$$

In this case, the velocity modulus $V=\sqrt{\dot{x}^2+\dot{y}^2}$ takes the following form in terms of the finite-difference interpretation:

$$\sqrt{\dot{x}^2+\dot{y}^2}=\sqrt{\left(\frac{x_{i+1}-x_i}{h}\right)^2+\left(\frac{y_{i+1}-y_i}{h}\right)^2}=\\ =\frac{1}{h}\sqrt{(x_{i+1}-x_i)^2+(y_{i+1}-y_i)^2} \quad (18)$$

Consequently, the first equation of Eq. 11 takes the following form:

$$\frac{x_{i+2}-2x_{i+1}+x_i}{h^2}=-k\frac{x_{i+1}-x_i}{h}\cdot\\ \cdot\frac{1}{h}\sqrt{(x_{i+1}-x_i)^2+(y_{i+1}-y_i)^2}-\\ -fg\cdot\cos\beta\cdot\frac{\frac{x_{i+1}-x_i}{h}}{\frac{1}{h}\sqrt{(x_{i+1}-x_i)^2+(y_{i+1}-y_i)^2}} \quad (19)$$

After elementary transformations, this equation takes form as follows:

$$x_{i+2}=2x_{i+1}-x_i-k(x_{i+1}-x_i)\sqrt{(x_{i+1}-x_i)^2+(y_{i+1}-y_i)^2}-\\ -h^2fg\cdot\cos\beta\cdot\frac{x_{i+1}-x_i}{\sqrt{(x_{i+1}-x_i)^2+(y_{i+1}-y_i)^2}} \quad (20)$$

Thanks to similar transformations, the second equation of Eq. 11 takes the following form:

$$y_{i+2}=2y_{i+1}-y_i-k(y_{i+1}-y_i)\sqrt{(x_{i+1}-x_i)^2+(y_{i+1}-y_i)^2}-\\ -h^2fg\cdot\cos\beta\cdot\frac{y_{i+1}-y_i}{\sqrt{(x_{i+1}-x_i)^2+(y_{i+1}-y_i)^2}}+h^2g\sin\beta \quad (21)$$

The initial conditions of Eq. 12 can be represented as the following expressions:

$$x(0)=x_0,\ y(0)=y_0,\ \dot{x}(0)=\frac{x_1-x_0}{h}=V_{x_0},\ \ \dot{y}(0)=\frac{y_1-y_0}{h}=V_{y_0} \quad (22)$$

or in a form, which is more convenient for calculations:

$$x(0)=x_0,\ y(0)=y_0,\ x_1=x_0+h\cdot V_{x_0},\ \ y_1=y_0+h\cdot V_{y_0} \quad (23)$$

Finally, a system of recurrent algebraic equations (Eqs. 20, 21, 23) is obtained, which, given the known values $x_0$, $x_1$, $y_0$, $y_1$, provides an opportunity to consistently determine the coordinates of seeds on the distribution plate in each time period.

## Results and discussion

The main advantage of this method is that it is possible to determine the coordinates of seed distribution at each period of movement (their discrete values depending on the step) and, if necessary, change the direction of their movement.

The solution to this problem is implemented using a developed program. For a plate with a width $a$ = 0.075 m and a length $b$ = 0.175 m, and a selected time step $h$ = 0.0001 s, a cyclic procedure is constructed, which determines the trajectory of seed movement (Fig. 3).

In various situations, as a result of movement along the plate, the seeds reach its lateral boundaries; therefore, it is necessary to model the process of turning the seeds away from them.

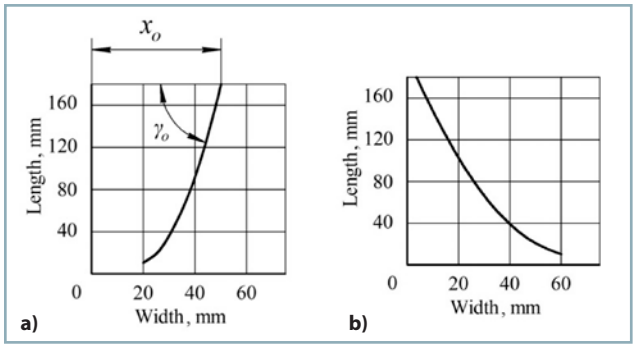


**Fig. 3** Movement trajectory of seeds over the plate
**a)** $x_0$ = 50 mm, $\gamma_0$ = 75°; b) $x_0$ = 4 mm, $\gamma_0$ = 115°

At the next stage, the computational algorithm is employed to determine the seed trajectory when meeting an obstacle of a cylindrical shape (Merodio and Ogden, 2019) and in a form of rubber pins on a plate with a radius $R$ centred at point $C$ with coordinates ($x_c$, $y_c$).

There occur several complications in determining the further movement of seeds. In certain cases, it would be possible to apply the usual procedure of turning away the individual seeds from a fixed obstacle, but due to its ellipsoid shape, reflection may occur in an unexpected way. In this regard, it was decided to apply a probabilistic approach and, for a quantitative implementation, to use a set of random numbers to determine the direction of the initial speed of seeds after meeting the pins. This direction is determined by an angle $\gamma$ between the horizontal axis and the tangent to the pin surface of; its initial value is $\gamma_0$ selected randomly at the meeting point with the seeds (Fig. 4), which is determined as follows (Bocko et al., 2014):

$$\gamma_0=\frac{\pi}{2}-\arctan\left|\frac{y_c-y_{i+2}}{x_c-x_{i+2}}\right|$$

Subsequently, the value $x_{i+2}$ is changed to the value $x_{i+1}$, and the value $y_{i+2}$ is changed to the value $y_{i+1}$.

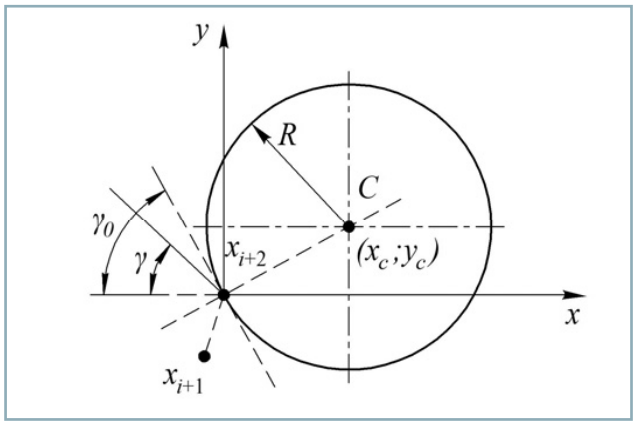


**Fig. 4** Simulation of loosening the seeds from the pin

New value $y_{i+2}$ is changed to $y_{i+2} + Sh \cdot \sin\gamma$, and the new value $x_{i+2}$ is changed to $x_{i+2} - Sh \cdot \cos\gamma$ if $x_{i+2} < x_c$, and $x_{i+1} + Sh \cdot \cos\gamma$ if $x_{i+2} > x_c$, where $Sh = \sqrt{(x_{i+2} - x_{i+1})^2 + (y_{i+2} - y_{i+1})^2}$ (Starovoitov and Naghiyev, 2012).

The numerical implementation of algorithm for solving this problem stems from the analytical modelling of location, in which the pins act as obstacles to the movement of seeds, and step-by-step control of the coordinates of seeds that move along a distribution plate. The cyclic series of conditional operators corrects the changes in seed trajectory in case of a direct encounter with the pin, i.e. with a cylindrical barrier, or with the distribution plate lateral borders, which was considered earlier.

The final simulation stage includes determination of the optimal number of rows of pins on the distribution plate along its width and seed distribution to the soil surface.

Based on the equation of seed falling from a height $H$ and taking into account the air resistance force after its transformation and integration, as well as the accepted initial conditions, the following expression for the rate of seed fall on the distribution plate was obtained:

$$V = \frac{3.12}{k}\left(-\sqrt{k} + \frac{\sqrt{k\,e^{6.24\sqrt{kt}}}}{0.5e^{6.24\sqrt{kt}} + 0.5}\right) \quad (24)$$

where:

$k$ – coefficient of air resistance to the seed movement, at $H = 0.7$ m, $k = 0.2$

Application examples of Eq. 24 and developed algorithm for determining the trajectory of seed movement are shown in Fig. 5.

The algorithm for solving this problem determines the location of the loading zone, subsequently divided into parts by a rectangular grid, from the nodes of which the initial movement of seeds and cyclical variations of initial angle of movement path occur. Numerical computer experiments showed that in order to achieve the optimal uniform distribution of seeds on the distribution plate of proposed grain drill opener, it is sufficient to place nine rows of pins on it. Both pins and distribution plate surface need to be rubber-coated in order to mitigate the injury to seeds and improve their quality indicators.

It was experimentally established that, during the fall of seeds with weight of 0.04–0.05 g to the distribution plate with rubber-coated pins at a height of 0.7 m, drag and friction coefficients of 0.2–0.3, impact force less than 5 N, acceleration of 0.025 m·s$^{-2}$, working body tilt angle to the soil surface of up to 30–45°, and an approximate value of $e \approx 2.718$, the actual movement speed of seeds will be 3.0–3.5 m·s$^{-1}$, seed microtrauma will be close to minimum (2.5–2.9%), and uniformity of distribution to furrow bottom after sowing will be equal to 94–95% and higher if sown in the form of strips, not rows. In such manner, there will be positive conditions for germination, growth and development of plants during the growing season, which will ensure the rational use of water, fertilizers, solar energy and formation of high and quality crops (Turan et al., 2014).

Experimental, industrial and laboratory studies on the influence of seeder working bodies on injury to seeds and their quality indicate that the largest amount of microtrauma observed during the technological process from harvest to sowing was showed by wheat variety Odesskaya-237 during threshing with the DON-1500B harvester, and the least amount of microtrauma to seeds was showed by Odessa variety 237 during threshing with a rotary combine "John Deere".

Data analyses on the quality indicators of winter wheat showed that, after sowing, the seed material purity was 98–99%, the least amount of weeds was showed by Steppe Pearl variety, and the greatest amount of weeds was showed by Odessa-237 wheat variety – 5 pieces per kg$^{-1}$ of seeds.

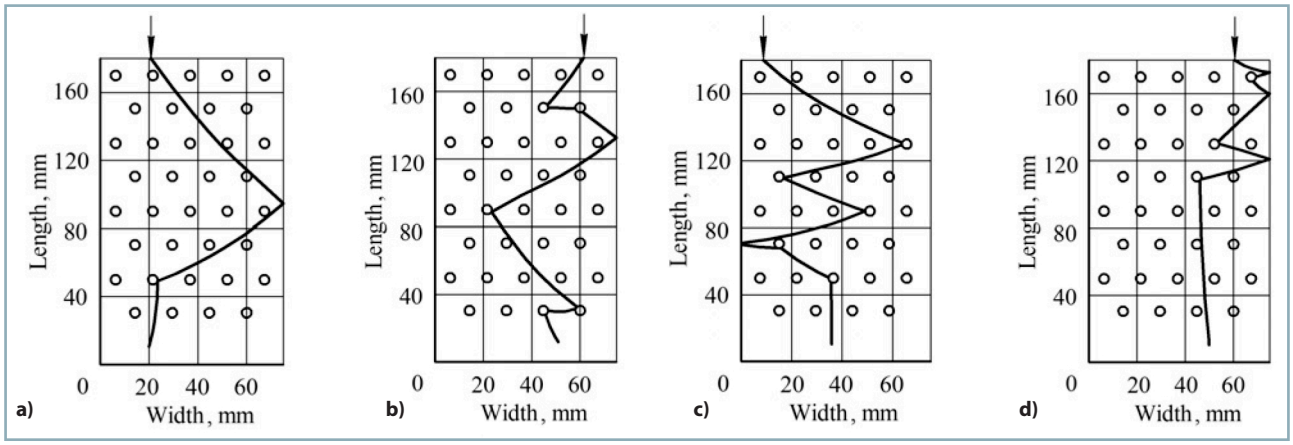


**Fig. 5** Examples of the trajectory modelling of seed movement
a) $x_0 = 21$ mm, $\gamma_0 = 130°$; b) $x_0 = 61.5$ mm, $\gamma_0 = 55°$; c) $x_0 = 9$ mm, $\gamma_0 = 140°$; d) $x_0 = 60.5$ mm, $\gamma_0 = 155°$

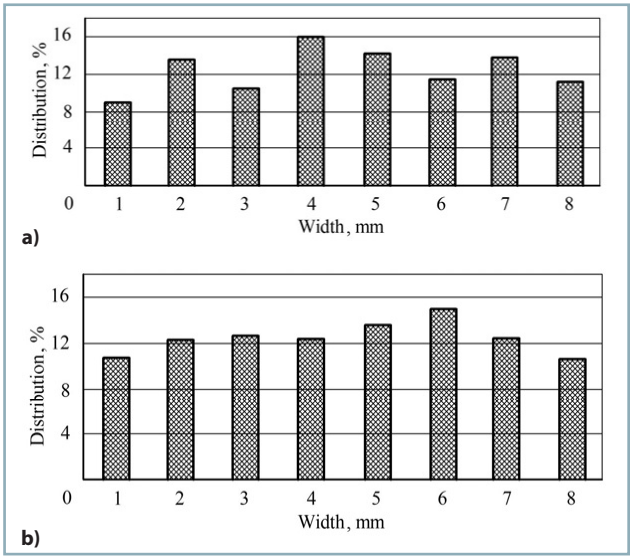


**Fig. 6** Percentage values of the distribution of seeds to the furrow bottom when leaving the distribution plate along its width during sowing
a) seven rows of pins; b) nine rows of pins

It is necessary to emphasize that the bobbin machines and coulters had a negative effect on the injury to seeds and contributed to its increase by 4–5%, which was the reason for the deterioration of seed quality during the sowing process – similar trend was also observed by Vasylkovska et al. (2016) and Bulgakov et al. (2016).

Similar studies on injury to seeds during sowing, conducted with respect to winter rye, showed that winter rye seeds received more significant injuries than winter wheat seeds at each stage of their treatment, including sowing. However, cultivation of this plant can be economically efficient if the seeds are uniformly distributed to the soil and the injury to seeds is minimalised as much as possible – in such manner, the plants would germinate simultaneously and each would receive the nutrition from the same zones.

## Conclusion

1. A system of the second-order quasilinear differential equations was obtained, which describes the motion of seeds along the distribution plate surface.
2. Implementation of this mathematical model made it possible to determine the coordinates of seeds and, if necessary, change the direction of their movement by enhancing or modernizing the working elements of opener to improve the conditions of seed distribution to soil and reduce their injury.
3. To achieve the optimal uniform distribution of seeds on the distribution plate, it is sufficient to place nine rows of pins on it. Surface of both pins and plate must be covered with rubber material in order to reduce the injury to seeds.
4. Uniform distribution of seeds to the furrow bottom, as well as rubber coating of pins and distribution plate, contributes to reduction of seed collisions with pins along the distribution plate, mitigation of injury to seeds, germination improvement, and improve the conditions for plant growth and development, which ultimately leads to an increase in grain yield.

## References

BOCKO, J. – GLODOVÁ, I. – LENGVARSKÝ P. 2014. Some differential equations of elasticity and their lie point symmetry generators. In Acta Mechanica et Automatica, vol. 8, no. 2, pp. 99–102.

BULGAKOV, V. – ADAMCHUK, V. – GOROBEY, V. – OLT, J. 2016. Theory of the oscillations of a toothed disc opener during its movement across irregularities of the soil surface. In Agronomy Research, vol. 14, no. 3, pp. 711–724.

DEREVJANKO, D. A. – GRABAR, I. G. – SINJAVSKAJA, A. I. 2017. The two-disc wide-row coulter. Patent of Ukraine №96249. (In Ukrainian: Soshnik dvuhdiskovyiy shirokoryadnyiy).

EGLI, D. B. – RUCKER, M. 2012. Seed vigor and the uniformity of emergence of corn seedlings. In Crop science, vol. 52, pp. 2774.

GURSOY, S. – GUZEL, E. 2010. Determination of physical properties of some agricultural grains. In Research Journal of Applied Sciences, Engineering and Technology, vol. 2, no. 5, pp. 492–498.

KARAJ, S. – MUËLLER, J. 2010. Determination of physical, mechanical and chemical properties of seeds and kernels of *Jatropha curcas* L. In Industrial Crops and Products, vol. 32, no. 2, pp. 129–138.

KOVALYSHYN, S. – DADAK, V. – KONYK, S. 2015. Intensification of the process of preparing small seed crop mixtures. In Acta Technologica Agriculture, vol. 18, no. 4, pp. 108–112.

KUZMINSKYI, R. – KOVALISHYN, S. – KOVALCHYK, Yu. – SHEREMETA, R. 2018. Mathematical models of geometric sizes of cereal crops' seeds as dependent random variables. In Acta Technologica Agriculture vol. 18, no. 4, pp. 100–104.

LIU, T. – Li, R. – JIN, X. – DING, J. – ZHU, X. – SUN, C. – GUO, W. 2017. Evaluation of seed emergence uniformity of mechanically sown wheat with UAV RGB imagery. In Remote Sensing, vol. 9. pp. 1–15.

MALEKI, M. R. – JAFARI, J. F. – RAUFAT, M. H. – MOUAZEN, A. M. – BAERDEMAEKER, J. De. 2006 Evaluation of seed distribution uniformity of a multi-flight auger as a grain drill metering device. In Biosystems Engineering, vol. 94, no. 4, pp. 535–543.

MERODIO, J. – OGDEN, R. 2019. Finite deformation elasticity theory. In Constitutive Modelling of Solid Continua. Springer. doi: 10.1007/978-3-030-31547-4_2.

NEUGSCHWANDTNER, R. W. – WINKLER, J. – BERNHART, M. – PUCHER, M. A. – KLUG, M. – WERNI, C. – ADAM, E. – KAUL, H. 2020. Effect of row spacing, seeding rate and nitrogen fertilization on yield and yield components of soybean. In Die Bodenkultur: Journal of Land Management, Food and Environment, vol. 70, no. 4, pp. 221–236.

PRISYAZHNYUK, M. V. 2013. Theory of vibrating machines of agricultural production. Kiev: Agrarnaja nauka, 439 pp. (In Ukrainian: Teoriia vibratsiinykh mashyn silskohospodarskoho vyrobnytstva).

PYLYPAKA, S. F. – NESVIDOMIN, V. M. – BABKA, V. M. – KLENDIY, M. B. 2018. Particle motion on a stationary screw surface with a set axial curve. In Applied Questions of Mathematical Modeling, vol. 2, pp. 123–132.

STAROVOITOV, E. I., – NAGHIYEV, F. B. 2012. Foundations of the Theory of Elasticity, Plasticity, and Viscoelasticity. New York: Apple Academic Press, 320 pp.

TURAN, J. – VIŠACKI, V. – MEHANDŽIC, S. – FINDURA, P. – BURG, P. – SEDLAR, A. 2014. Sowing quality indicators for a seed drill with overpressure. In Acta Universitatis Agriculturae et Silviculturae Mendelianae Brunensis, vol. 62, no. 6, pp. 1487–1492.

TURAN, J. – VIŠACKI, V. – SEDLAR, A. D. – PANTELIĆ, S. – FINDURA, P. – MACHAL, P. – MAREČEK, J. 2015. Seeder with different seeding apparatus in maize sowing. In Acta Universitatis Agriculturae et Silviculturae Mendelianae Brunensis, vol. 63, no. 1, pp. 137–141.

VASYLKOVSKA, K. V. – LESHCHENKO, S. M. – VASYLKOVSKYI, O. M. – PETRENKO, D. I. 2016. Improvement of equipment for basic tillage and sowing as initial stage of harvest forecasting. In MATEH – Agricultural Engineering. Sep.–Dec., vol. 50, no. 3, pp. 13–20.

sciendo

DOI: 10.2478/ata-2020-0032

*Acta Technologica Agriculturae 4/2020* *Michal Angelovič et al.*

Acta Technologica Agriculturae 4
Nitra, Slovaca Universitas Agriculturae Nitriae, 2020, pp. 201–207

# COMPARISON OF SMOKE EMISSIONS IN DIFFERENT COMBUSTION ENGINE FUELS

Michal ANGELOVIČ*, Juraj JABLONICKÝ, Zdenko TKÁČ, Marek ANGELOVIČ

Slovak University of Agriculture in Nitra, Faculty of Engineering, Slovakia

Goal of this study was to investigate and evaluate an impact of two alternative fuels on smoke emissions in comparison to diesel fuel. This study observes three different combustion engine fuels: biodiesel produced by Meroco, Inc. Company (Alternative fuel I); biodiesel produced in factory situated in Sereď (Alternative fuel II); and conventional diesel fuel (Diesel fuel) from Slovnaft, Inc. Company service station. All measurements were repeated three times. Measurements were conducted by free acceleration test at different engine loads. A statistically significant difference ($P$ <0.05) in smoke emissions values was detected between Alternative fuel I and conventional Diesel fuel, and between Alternative fuel I and Alternative fuel II. The difference in smoke emissions values between conventional fuel and Alternative fuel II was not statistically significant ($P$ >0.05). Tested engine has met the requirements of the EURO 3 emission limit values in relation to the measurement results of particulate matter emissions.

**Keywords:** light absorption coefficient; alternative fuels; free acceleration; combustion engine; diesel engine

Research of combustion engine drive is focused on alternative fuels connected to conventional fuel consumption reduction. Alternative engine drive is connected to the fuel type used for combustion engine consumption. Alternative fuel, i.e. any non-petroleum origin fuel, can be used as an alternative to conventional petrol or diesel fuel. A development of combustion engines is focused on production of more efficient, less noisy and less intensive engines with reduced emissions of exhaust gas pollutants. The purpose of this scientific study was to measure and investigate smoke emissions produced by two different alternative fuels. The first sample was biodiesel produced by Meroco, Inc. Company (Alternative fuel I), the second sample was biodiesel produced in factory situated in Sereď (Alternative fuel II). An impact of fuels was monitored in dependence on engine load. The conventional Diesel fuel was used for final comparison of results.

Oxygen in biodiesel plays an important role in relation to production of harmful emissions. Oxygen improves a combustion process in engine by reducing the production of particulates in contrast to Diesel fuel. Particulate matter reduction is a result of low sulphur content in biodiesel. Particulates with lower sulphur content are less cancerogenic. A short ignition delay during combustion in engine will reduce an amount of burnt fuel at fixed volume level. Maximal pressure and temperature values in engine cylinders are lower for biodiesel, especially at the beginning of combustion process. The duration of high pressure and temperature is shorter, which results in reduction of nitrogen oxides emissions compared to Diesel fuel. A positive impact of shorter ignition delay on nitrogen oxides production is caused by the oxygen in biodiesel. Oxygen enriched combustion is one of the most attractive combustion technologies for pollution management. However, there is a considerable increase in nitrogen oxides emissions due to increased combustion temperature and extra oxygen available, which needs to be addressed (Baskar and Senthilkumar, 2016). The standpoint given by Baskar and Senthilkumar (2016) can be justified by increased oxygen concentration of air, which was taken in into the engine combustion chamber, which was the purpose of their experiment.

Positive effects of shorter ignition delay also include a reduction in production of unburnt hydrocarbons. Biodiesel of plant origin has a positive effect on a balance of carbon dioxide circulation in nature. The production of carbon dioxide during combustion corresponds to its consumption during photosynthesis. Biodegradability of fatty acid methyl ester in environment is 95% in six days (Laurin, 2007).

Kahraman et al. (2016) investigated the engine performance and exhaust gas emissions of diesel fuel and cotton oil methyl ester (COME) blends at proportions of 2%, 5%, and 10%. The engine was fuelled with COME-diesel blends and pure diesel, running at six different engine speeds (1,000; 1,200; 1,400; 1,600; 1,800; 2,000 rpm) and at full load. The engine performance decreased with COME added to diesel fuel, but exhaust emissions showed improved results.

## Material and methods

### Measurement of smoke emissions

#### Detection methods for exhaust gas emissions

Particulate matter emissions of diesel engine can be measured using several methods, requirements for

**Contact address:** Michal Angelovič, Slovak University of Agriculture in Nitra, Faculty of Engineering, Department of Machines and Production Biosystems, Tr. Andreja Hlinku 2, 949 76 Nitra, Slovak Republic; e-mail: michal.angelovic@uniag.sk

which are defined by the Society of Automotive Engineers (SAE) standards and regulations of the United Nations Economic Commission for Europe (ECE). The study presented is focused on smoke opacity measurement of isolated samples.

### Method for determination of particulate matter emissions using smoke opacity measurement

This method is based on physical phenomenon of gases measurement, characterized by light beam optical absorption. Opacity, an ability to stop light from being transmitted, is defined by optical path length and described by the light absorption coefficient. Opacity, measured using opacimeter, is an invert value to transparency. The smoke opacity, described by the light absorption coefficient k, which is defined by Directive 2014/45/EU of the European Parliament and of the Council, and Methodological Guideline no. 32/2018, is calculated as follows:

$$\phi = \phi_o \, x \, e^{-kL} \qquad (1)$$

where:

$L$ – effective optical path length (m)
$\phi_o$ – initial light beam
$\phi$ – transmitted light beam
$k$ – light absorption coefficient ($m^{-1}$)
$e$ – base of natural logarithm

Light absorption coefficient is a smoke opacity unit characterizing an optical absorption ability of medium. A difference between the maximum and minimum values of light absorption coefficient is called dispersion (variance). Smoke opacity measurement is a measurement of absorbed light transmitted through exhaust gas column (optical path). This method of particulate matter emissions measurement is time effective and not very demanding in terms of technology. The emissions of vehicles can be measured by two methods: tests at steady speeds and tests under free acceleration. Considering the given conditions test under free acceleration for smoke opacity measurement was selected for this study.

### Smoke opacity measurement with test under free acceleration

Smoke opacity measurement with test under free acceleration, defined by Decree of the Ministry of Transport and Construction of the Slovak Republic no. 138/2018, is used for particulate matter (PM) emissions measurement. This measurement is used for vehicles with diesel engine emissions control and homologation tests of vehicle engines. All conditions of this method are described in the Methodological Guideline of the Ministry of Transport and Construction of the Slovak Republic no. 32/2018. The smoke opacity is measured during actual acceleration from engine idling speed to full load rpm. The engine overload occurs at full fuel dose, during which the engine operation is reaching its maximal smoke emission level. This method is time-efficient and the values of measured smoke emissions reflect the dynamic phenomena in transition mode. The maximal smoke emissions level is reached at minimal value of air-fuel ratio. A slight signal defect can shift the maximal measured smoke emission values to higher rpm, therefore, the maximal measured smoke emissions value can be higher compared to opacity measurement during the steady engine operation (Methodological Guideline of the Ministry of Transport and Construction of the Slovak Republic no. 32/2018).

## Devices and sensors

### Thermometer (oil temperature gauge)

Temperature is usually measured by thermometer (oil temperature gauge). The thermometer is immersed into motor oil through an oil dipstick pipe. While immersed, the thermometer should reach motor oil level; however, it should not touch rotation parts of engine.

### Speedometer

The speedometer (revolution indicator) is used to detect external speed parameters. Operation of these devices is based on an evaluation of signals coming from different sources. Speedometer is basically a converter, converting different input variables into the electric potential at a frequency corresponding to the engine rpm: speedometer with a ring sensor, speedometer detecting electrical signal of on-board network, speedometer with optical sensor and speedometer with vibration and acoustic sensor.

### Power brake

The power brake, examining combustion engines up to 20 kW, is composed of hydraulic circuit providing engine load, control and evaluation part. Basic device layout is shown in Fig. 1 and measuring device is shown in Figs. 2 and 3.

### Opacimeter

Smoke opacity detection is based on the measurement of reduction in light intensity while the light is transmitted through exhaust gas. The basic unit of smoke opacity is $m^{-1}$ expressing a light extinction transmitted through exhaust gas column. Exhaust gas samples are transited through exhaust probe and connecting hose from exhaust system to measuring head

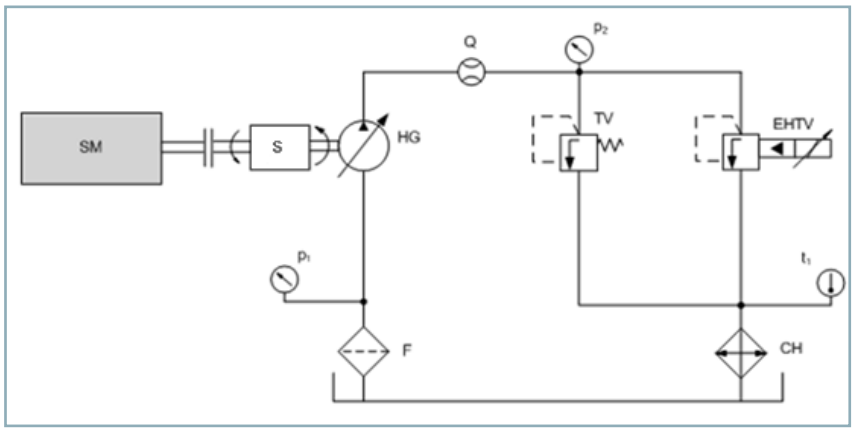


**Fig. 1** Layout of loading device for combustion engine
SM – combustion engine; S – rpm sensor; HG – hydrogenerator; F – filter; CH – cooler; TV – pressure valve; EHTV – electro-hydraulic pressure valve; p1 – pressure gauge; t1 – thermometer; Q – flow meter

**Fig. 2** Fuel tanks

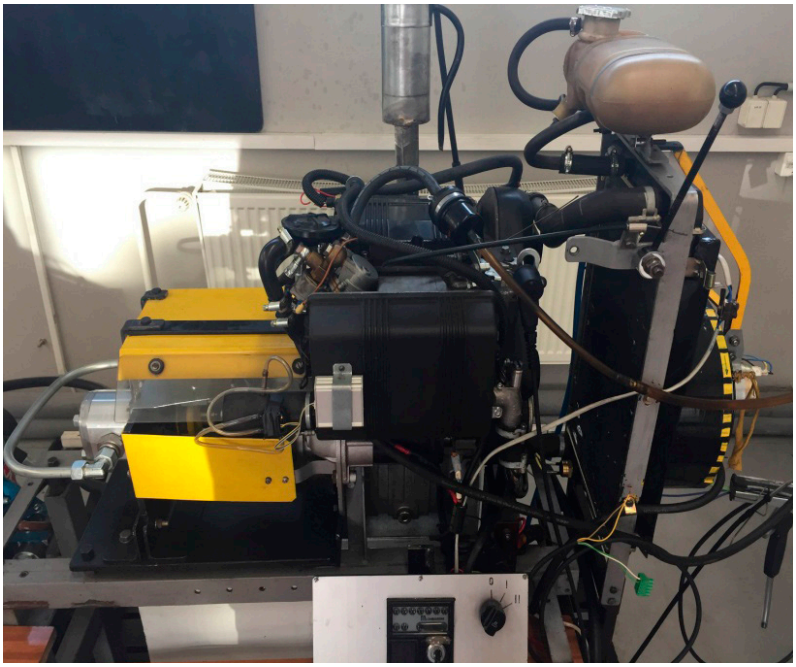

**Fig. 3** Test Engine

of opacimeter by pumping device or their own kinetic energy. Opacimeter consists of two parts: evaluation unit for processing and displaying measured variables by means of monitor or graphic displays; and measuring chamber for actual measuring process. Measuring chamber is connected to evaluation unit by connecting and data lines (Fig. 4). Measuring chamber is connected to vehicle by sample conditioning tube. Exhaust gases are transited into the measuring chamber (light unit), which contains a lamp element providing the light source. The light travels through the measuring cell towards the detector element, which is placed opposite to light source and measures the light extinction that corresponds to engine smoke opacity. An air gap, created by fans, is protecting light source and detector elements from the soot deposits. Measuring cell is a 0.430 m long glass cylinder. According to the instructions for use of the measuring chamber, the chamber is heated to a temperature above 75 °C to prevent mist creation.

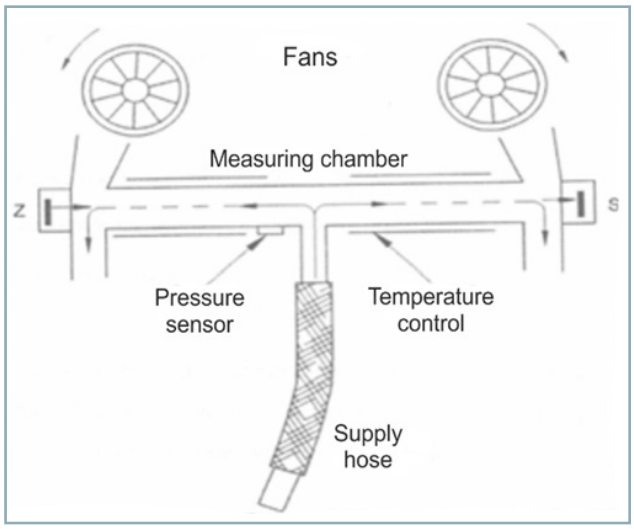


**Fig. 4** Opacimeter measuring chamber

Measuring system with opacimeter MAHA MDO 2 LON, which evaluates the smoke opacity of partial flow exhaust gas samples, and VI.10/0.00.GB software, which is in compliance with the ECE Regulation no. 24, was used for the purposes of this experiment. Furthermore, MAHA RPM VC2 speedometer with vibration and acoustic sensor was also utilized. Opacimeter MAHA MDO 2 LON has two measuring modes: Mode A (with sampling frequency of 0.2 s) for homologation tests and Mode B (with sampling frequency of 1 s) for smoke emission inspections. The smoke opacity was measured in accordance with the Methodical Instruction of the Ministry of Transport, Posts and Telecommunications of the Slovak Republic for emission inspections. The smoke opacity D was calculated as an average value of light absorption coefficients k detected in last three smoke opacity measurements under free acceleration:

**Table 1** Measuring device characteristics

| Measuring device | Quantity measured by the measuring device | Measuring unit | Minimum measuring range | Maximum scale interval | Maximum permissible meter error |
|---|---|---|---|---|---|
| **Opacimeter** | light absorption coefficient | $m^{-1}$ | (0–9.99) $m^{-1}$ | 0.01 $m^{-1}$ | to 2.5 $m^{-1}$ ±0.25 $m^{-1}$ over 2.5 $m^{-1}$ ±0.40 $m^{-1}$ |

**Table 2** Results of Alternative fuel I, Alternative fuel II and Diesel fuel measurements

| Series of measuring | Fuel | Measurement | $k$ ($m^{-1}$) | Idle speed ($min^{-1}$) | Regulator speed ($min^{-1}$) | Temperature (°C) |
|---|---|---|---|---|---|---|
| 1st | AFI | 1st | 0.29 | 860 | 3,230 | 81 |
| | | 2nd | 0.29 | 860 | 3,300 | 81 |
| | | 3rd | 0.29 | 860 | 3,310 | 81 |
| | $\dot{x}(D)$ ± variance | | 0.29 ±0.00 | AFI in compliance | | |
| 2nd | AFI | 1st | 0.29 | 870 | 3,250 | 81 |
| | | 2nd | 0.29 | 860 | 3,230 | 83 |
| | | 3rd | 0.29 | 870 | 3,120 | 83 |
| | $\dot{x}(D)$ ± variance | | 0.29 ±0.00 | AFI in compliance | | |
| 3rd | AFI | 1st | 0.28 | 860 | 3,020 | 81 |
| | | 2nd | 0.29 | 870 | 3,110 | 81 |
| | | 3rd | 0.29 | 870 | 3,160 | 83 |
| | $\dot{x}(D)$ ± variance | | 0.29 ±0.00 | AFI in compliance | | |
| 1st | AFII | 1st | 0.27 | 890 | 3,300 | 81 |
| | | 2nd | 0.27 | 900 | 3,220 | 82 |
| | | 3rd | 0.27 | 900 | 3,230 | 83 |
| | $\dot{x}(D)$ ± variance | | 0.27 ±0.00 | AFI in compliance | | |
| 2nd | AFII | 1st | 0.28 | 890 | 3,210 | 83 |
| | | 2nd | 0.28 | 890 | 3,260 | 83 |
| | | 3rd | 0.28 | 890 | 3,340 | 83 |
| | $\dot{x}(D)$ ± variance | | 0.28 ±0.00 | AFI in compliance | | |
| 3rd | AFII | 1st | 0.28 | 880 | 3,140 | 83 |
| | | 2nd | 0.28 | 890 | 3,200 | 83 |
| | | 3rd | 0.28 | 890 | 3,270 | 83 |
| | $\dot{x}(D)$ ± variance | | 0.28±0.00 | AFI in compliance | | |
| 1st | DF | 1st | 0.27 | 870 | 2,700 | 78 |
| | | 2nd | 0.27 | 870 | 2,600 | 78 |
| | | 3rd | 0.27 | 870 | 2,770 | 78 |
| | $\dot{x}(D)$ ± variance | | 0.27 ±0.00 | AFI in compliance | | |
| 2nd | DF | 1st | 0.28 | 870 | 2,860 | 83 |
| | | 2nd | 0.28 | 870 | 2,730 | 83 |
| | | 3rd | 0.28 | 870 | 2,720 | 83 |
| | $\dot{x}(D)$ ± variance | | 0.29 ±0.00 | AFI in compliance | | |
| 3rd | DF | 1st | 0.28 | 880 | 2,730 | 83 |
| | | 2nd | 0.28 | 880 | 2,850 | 83 |
| | | 3rd | 0.28 | 880 | 2,820 | 83 |
| | $\dot{x}(D)$ ± variance | | 0.28 ±0.00 | AFI in compliance | | |

AFI – Alternative fuel I; AFII – Alternative fuel II; DF – Diesel fuel; n – number of measurements; $\dot{x}$ – arithmetic mean; $k$ – light absorption coefficient; $D$ – smoke opacity; variance – spread (difference) between minimal and maximal values of light absorption coefficient

$$D = (k_N + k_{N-1} + k_{N-2})/3 \quad m^{-1} \qquad (2)$$

where:
*D* – calculated smoke opacity value
*k* – measured value of light absorption coefficient ($m^{-1}$)
*N* – measurement serial number

### Statistical methods

Results of this study are presented in arithmetic mean ($\bar{x}$) values, variance values representing spread (difference) between minimal and maximal values, standard deviations (SD) and coefficients of variation ($c_v$, %), which were evaluated by descriptive statistics. Scheffé's method of SAS 9.1 system was used for variance analysis (SAS, User's Guide, 2005).

## Results and discussion

### Results of smoke emissions and smoke opacity measurements under free acceleration for Alternative fuel I, Alternative fuel II and Diesel fuel

Results of smoke emissions and smoke opacity measurements under free acceleration for Alternative fuel I; Alternative fuel II; and Diesel fuel are presented in Table 2.

Idle speed (860 $min^{-1}$) of Alternative fuel I in the 1st series of emissions measurements showed lower results by 10 $min^{-1}$ compared to idle speed of Diesel fuel in the 1st series of emission. The regulator speed ranged from 3,230 to 3,310 $min^{-1}$and was higher in contrast to values shown by Diesel fuel. Engine temperature (81 °C) was identical in all three measurements and was higher by 3 °C than temperature of diesel engine. Light absorption coefficient was identical in all three measurements (0.29 $m^{-1}$). The smoke opacity was 0.29 $m^{-1}$ with a variance of 0.00 $m^{-1}$. Idle speed in the 2nd series of emissions measurements ranged from 860 to 870 $min^{-1}$ and regulator speed ranged from 3,120 to 3,250 $min^{-1}$. Engine temperature increased to 83 °C during the 2nd and 3rd series of measurements in comparison to the 1st series of measurements (81 °C). Light absorption coefficient was identical in all three measurements (0.29 $m^{-1}$). The smoke opacity was 0.29 $m^{-1}$ with a variance of 0.00 $m^{-1}$. Idle speed in the 3rd series of emissions measurements ranged from 860 to 870 $min^{-1}$ and regulator speed ranged from 3,020 to 3,160 $min^{-1}$. Engine temperature ranged from 81 °C to 83 °C during the 2nd and 3rd series of measurements. Measured values of light absorption coefficient were 0.28 and 0.29 $m^{-1}$, value of the smoke opacity was 0.29 $m^{-1}$, with a variance of 0.00 $m^{-1}$. Based on the results of three series of measurements, Alternative fuel I complies with the EURO 3 emission limits.

The idle speed of Alternative fuel II ranged from 890 to 900 $min^{-1}$ in the 1st series of emissions measurement. In regard to all three measurements conducted as a part of the 1st series of measurements, the idle speed of Alternative fuel II was higher compared to the idle speed of both Diesel fuel and Alternative fuel I in the 1st series of measurements. The values of regulator speed – ranging from 3,220 to 3,300 $min^{-1}$ – were higher in contrast to values shown by Diesel fuel and almost identical with values shown by Alternative fuel I. Engine temperature ranged from 81 to 83 °C and was higher than engine temperature of Diesel fuel. Light absorption coefficient was identical in all three measurements (0.27 $m^{-1}$). The smoke opacity was 0.27 $m^{-1}$ with a variance of 0.00 $m^{-1}$. The idle speed in the 2nd series of emissions measurements was identical for all three measurements (890 $min^{-1}$), the regulator speed ranged from 3,210 to 3,340 $min^{-1}$ with engine temperature of 83 °C. Light absorption coefficient was identical in all three measurements (0.28 $m^{-1}$). The smoke opacity was 0.28 $m^{-1}$ with a variance of 0.00 $m^{-1}$. Considering the 3rd series of emissions measurements, the idle speed ranged from 880 to 890 $min^{-1}$ and the regulator speed ranged from 3,140 to 3,270 $min^{-1}$. Engine temperature (83 °C) was identical in all three measurements. Measured values of light absorption coefficient (0.28 $m^{-1}$) were identical in all three measurements. The smoke opacity was 0.28 $m^{-1}$ with a variance of 0.00 $m^{-1}$. All in all, based on the results of the three series of measurements, it can be stated that the Alternative fuel II meets the requirements determined by the EURO 3 emission limits.

In regard to the 1st series of emissions measurements of Diesel fuel, the idle speed was identical in all three measurements (870 $min^{-1}$), the regulator speed ranged from 2,600 to 2,770 $min^{-1}$ with engine temperature from 81 to 83 °C. Light absorption coefficient was identical in all three measurements (0.27 $m^{-1}$). The smoke opacity was 0.27 $m^{-1}$ with a variance of 0.00 $m^{-1}$. In terms of the 2nd series of emissions measurements, the idle speed was identical in all three measurements (870 $min^{-1}$), which is comparable with the 1st series. The regulator speed ranged from 2,720 to 2,860 $min^{-1}$. Engine temperature (83 °C) was higher by 5 °C than engine temperature in the 1st series of measurements. Light absorption coefficient was identical in all three measurements (0.28 $m^{-1}$). The smoke opacity was 0.28 $m^{-1}$ with a variance of 0.00 $m^{-1}$. Considering the 3rd series of emissions measurements, the idle speed was identical in all three measurements (880 $min^{-1}$) and was higher than idle speed shown in the 1st and 2nd series. The regulator speed ranged from 2,730 to 2,850 $min^{-1}$ with engine temperature of 83 °C, which is identical to the temperature observed in the 2nd series. Light absorption coefficient was identical in all three measurements (0.28 $m^{-1}$). The smoke opacity was 0.28 $m^{-1}$ with a variance of 0.00 $m^{-1}$. Based on the results of the three series of measurements, Diesel fuel complies with the EURO 3 limits.

Ultimately, measurement results of smoke emissions and smoke opacity proved that test engine fuelled by Alternative fuel I, Alternative fuel II and Diesel fuel is in compliance with the EURO 3 limits.

### Statistical evaluation of smoke emissions and smoke opacity results of different fuels

Statistical evaluation of smoke emissions and smoke opacity results is shown in Table 3.

Statistical analysis of smoke emissions shows an existence of differences in smoke opacity between investigated engine fuels. Average values of the smoke opacity of Diesel fuel and Alternative fuel II were 0.28 $m^{-1}$, which are lower in contrast to the smoke opacity (0.29 $m^{-1}$) detected for Alternative fuel I. According to the coefficient of variation, smoke opacity values ranged from 10.71% (Alternative fuel I) to 17.86%

**Table 3** Statistical evaluation of smoke emissions and smoke opacity of different fuels

| Fuel | *n* | $\acute{x}$ | SD | $c_v$ (%) |
|---|---|---|---|---|
| **Diesel fuel** | 9 | 0.28a | 0.05 | 17.86 |
| **Alternative fuel I** | 9 | 0.29b | 0.03 | 10.71 |
| **Alternative fuel II** | 9 | 0.28a | 0.05 | 17.86 |

*n* – number of measurements; – arithmetic mean; SD – standard deviation; $c_v$ – coefficients of variation; a, b – values in the column with different upper index letter have statistically significant ($P$ <0.05) differences

(Alternative fuel II and Diesel fuel). Difference in the smoke opacity was statistically significant ($P$ <0.05) between Diesel fuel and Alternative fuel I and between Alternative fuel I and Alternative fuel II. The results obtained show that there are minimal differences in the light absorption coefficient. In terms of the aforementioned, attention should be paid to the chemical composition of the fuels and their detailed analysis. Furthermore, more focus should also be paid to other options for investigation of the emissions produced by compression ignition combustion engines. Similarly to the light absorption coefficient, the emissions value might not be an adequate and objective assessment indicator of the emissions status in engine, especially when using alternative fuels, since there are devices installed in the exhaust systems that serve to reduce the exhaust emissions values. Therefore, attention should be also paid to other emissions components that would allow to objectively assess both the emissions status of the combustion engine and the production of emissions in the combustion of alternative fuels.

Minimum differences in the values of the light absorption coefficient between the compared fuels may indicate that the chemical composition of the tested alternative fuels is very similar to the reference fuel. The measurements were performed in accordance with the valid measurement methodology and the measuring device was regularly calibrated. Few authors (Qi et al., 2010) presented no differences, or minimal increase (Armas et al., 2010; Aydin and Bayindir, 2010) in particulate matter emissions of biodiesel, which could be caused by higher viscosity of biodiesel (Aydin and Bayindir, 2010). Higher viscosity decreases fuel atomization and combustion quality. Armas et al. (2010) found out that increase in particulate matter emissions is caused by unburnt or partially burnt hydrocarbon emissions. Hydrocarbon emissions condensated and were absorbed on the surface of particulate matter, which could cause an increase in soluble organic fraction – main element of particulate matter emissions. Results of the emissions measurement study presented are in compliance with mentioned conclusions. The study presented did not confirm a reduction of particulate matter emissions in biodiesel, which is a scientific conclusion of multiple authors (Pal et al., 2014; Yadav et al., 2016). Biodiesel quality can be improved by metal-based additives, cetane improver additives, fuel antioxidants, and oxygenating fuel additives. Furthermore, engine performance can be improved, and emissions can be reduced by fuel additives (Vijay Kumar et al., 2018). Angelovič et al. (2015) also reported that the mechanisms of oxidative degradation can be result of autoxidation in presence of atmospheric oxygen. The issue addressed by us is current from the environmental aspect, as evidenced by other publications. Beloev et al. (2017) focused on reducing the $CO_2$ emissions in the transport sector based on emission compensation and Čedík et al. (2018) solved the effect of biobutanol-sunflower oil-diesel fuel blends on operational parameters of combustion engines.

## Conclusion

Scientific study is based on contemporary scientific knowledge, experimental results and calculations pertaining to two types of alternative fuels. This study investigates the impacts of fuel type on exhaust gas emissions and smoke emissions in dependence on engine load. The first sample was biodiesel produced by Meroco, Inc. Company (Alternative fuel I), the second sample was biodiesel produced in factory situated in Sereď (Alternative fuel II). Conventional Diesel fuel produced by Slovnaft, Inc. Company service station was used in this experiment for the reference purposes. Results were achieved by means of experimental measurements, calculations, statistical analysis, evaluation and comparison. Based on the particulate matter emissions measurements, all three investigated fuels comply with EURO 3 emission limit. Statistical analysis of smoke emissions shows an existence of differences in the smoke opacity between investigated engine fuels, which was statistically significant (P<0.05) between Diesel fuel and Alternative fuel I and between Alternative fuel I and Alternative fuel II.

## Acknowledgements

This work was supported by AgroBioTech Research Centre built in accordance with the project "Building the Research Centre AgroBioTech" ITMS 26220220180.

This work was supported by the project VEGA 1/0464/17 "Monitoring the Impact of Ecological Fuels Obtained from Agricultural Production and Additives in Hydrocarbon Fuels on Technical and Environmental Performance of Internal Combustion Engines Used in Agricultural and Transport Machines".

## References

ANGELOVIČ, M. – JABLONICKÝ, J. – TKÁČ, Z. – ANGELOVIČ, M. 2015. Oxidative stability of fatty acid alkyl esters: a review. In Slovak Journal of Food Sciences (Potravinárstvo), vol. 9, no. 1, pp. 417–426.

ARMAS, O. – YEHLIU, K. – BOEHMAN, A. L. 2010. Effect of alternative fuels on exhaust emissions during diesel engine operation with matched combustion phasing. In Fuel, vol. 89, no. 19, pp. 438–456.

AYDIN, H. – BAYINDIR, H. 2010. Performance and emission analysis of cotton seed oil methyl ester in a diesel engine. In Renewable Energy, vol. 35, no. 3, pp. 588–592.

BASKAR, P. – SENTHILKUMAR, A. 2016. Effects of oxygen enriched combustion on pollution and performance characteristics of a diesel engine. In Engineering Science and Technology, vol. 19, no. 1, pp. 438–443.

BELOEV, I. – GABROVSKA-EVSTATIEVA, K. – EVSTATIEV, B. 2017. Compensation of $CO_2$ emissions from petrol stations with photovoltaic parks: Cost-benefit and risk analysis. In Acta Technologica Agriculturae, vol. 20, no. 4, pp. 85–90.

ČEDÍK, J. – PEXA, M. – PETERKA, B. – HOLUBEK, M. – MADER, D. – PRAŽAN, R. 2018. Effect of biobutanol-sunflower oil-diesel fuel blends on combustion characteristics of compression ignition engine. In Acta Technologica Agriculturae, vol. 21, no. 4, pp. 130–135.

Decree of the Ministry of Transport and Construction of the Slovak Republic no. 138/2018 of 27 April 2018 laying down details in the field of emission control.

Directive 2014/45/EU of the European Parliament and of the Council of 3 April 2014 on periodic roadworthiness tests for motor vehicles and their trailers and repealing the Directive 2009/40/EC (Text with EEA relevance).

KAHRAMAN, A. – CINIVIZ, M. – ÖRS, İ – OĞUZ, H. 2016. The effect on performance and exhaust emissions of adding cotton oil methyl ester to diesel fuel. In International Journal of Automotive Engineering and Technologies, vol. 5, no. 4, pp. 148–154.

LAURIN, J. 2007. Research of the impact of motor fuels containing biocomponent on action and emission of compression ignition and ignition engines in the vehicle fleet of the Czech Republic: Report of project co-investigators FT-TA4 / 066 for 2007. Liberec: Technical University of Liberec. (In Czech: Výzkum vlivu motorových paliv obsahujících biosložky na chod a emise vznětových a zážehových motorů ve vozidlovém parku ČR: zpráva spoluřešitele projektu FT-TA4/066 za rok 2007. Liberec: Technická univerzita v Liberci).

Methodological Guideline of the Ministry of Transport and Construction of the Slovak Republic no. 32/2018 for the performance of emission control of regular positive-ignition motor vehicles with an improved emission system, with petrol engine with improved emission system and with a diesel engine.

PAL, A. – MOHAN, S. – DHANANJAY, T. 2014. Production and performance testing of waste frying oil biodiesel. In International Journal of Current Engineering and Technology, vol. 4, no. 3, pp. 1366–1369.

QI, D. H. – CHEN, H. – GENG, L. M. – BIAN, Y. Z. H. 2010. Experimental studies on the combustion characteristics and performance of a direct injection engine fuelled with biodiesel/ diesel blends. In Energy Conversion and Management, vol. 51, no. 12, pp. 2985–2992.

SAS. USER'S GUIDE. 2005. Version 9.1 (TS1M3). SAS Institute Inc., Carry, NC, USA.

VIJAY KUMAR, M. – VEERESH BABU, A. – RAVI KUMAR, P. 2018. The impacts on combustion, performance and emissions of biodiesel by using additives in direct injection diesel engine. In Alexandria Engineering Journal, vol. 57, pp. 509–516.

YADAV, K. A. – KHAN, E. M. – DUBEY, M. A. – PAL, A. 2016. Performance and emission characteristics of a transportation diesel engine operated with non-edible vegetable oils biodiesel. In Case Studies in Thermal Engineering, vol. 8, pp. 236–244.